SPACE, TELECOMMUNICATIONS AND RADIOSCIENCE LABORATORY

STARLAB
DEPARTMENT OF ELECTRICAL ENGINEERING
STANFORD UNIVERSITY • STANFORD, CA 94305

Statistical Analysis and Modeling of Low-Frequency Radio Noise and Improvement of Low-Frequency Communications

by

Douglas A. Chrissan

Final Technical Report D179–1
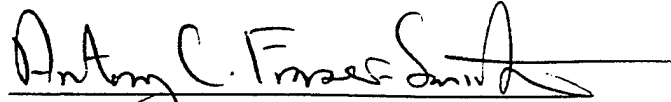
August 1998

19990226063

STATISTICAL ANALYSIS AND MODELING OF LOW-FREQUENCY RADIO NOISE AND IMPROVEMENT OF LOW-FREQUENCY COMMUNICATIONS

A DISSERTATION
SUBMITTED TO THE DEPARTMENT OF ELECTRICAL ENGINEERING
AND THE COMMITTEE ON GRADUATE STUDIES
OF STANFORD UNIVERSITY
IN PARTIAL FULFILLMENT OF THE REQUIREMENTS
FOR THE DEGREE OF
DOCTOR OF PHILOSOPHY

By
Douglas A. Chrissan
August 1998

I certify that I have read this dissertation and that in my opinion it is fully adequate, in scope and quality, as a dissertation for the degree of Doctor of Philosophy.

Antony C. Fraser-Smith
(Principal Adviser)

I certify that I have read this dissertation and that in my opinion it is fully adequate, in scope and quality, as a dissertation for the degree of Doctor of Philosophy.

Robert A. Helliwell

I certify that I have read this dissertation and that in my opinion it is fully adequate, in scope and quality, as a dissertation for the degree of Doctor of Philosophy.

Abbas El Gamal

Approved for the University Committee on Graduate Studies:

Abstract

Naturally occurring radio noise above approximately 100 MHz is well modeled for most applications as a Gaussian random process; however, atmospheric radio noise below 100 MHz is often impulsive in nature and is not well modeled as Gaussian. Atmospheric events (mainly lightning strokes, which create electromagnetic emissions known as *sferics*) produce large, clustered impulses in the noise waveform seen at a receiving antenna, causing the waveform to vary greatly from typical Gaussian background noise. Due to large variations in sferic activity on a seasonal and diurnal basis and with the passing of individual storms, atmospheric noise is also non-stationary.

The objective of this work is the statistical characterization and modeling of atmospheric radio noise in the range 10 Hz – 60 kHz (denoted *low-frequency* noise), with the specific goal of improving communication systems operating in this range. The analyses are based on many thousands of hours of measurements made by the Stanford Radio Noise Survey System.

The statistics analyzed include seasonal and diurnal variations, amplitude probability distributions (APDs), impulse interarrival time distributions, background noise statistics, and power spectral densities. Noise characteristics derived from these analyses are presented, and several noise models that accurately represent low-frequency noise APDs are compared. The most accurate model for representing low-frequency noise APDs is found to depend on geographic location, time of year and day, bandwidth, and center frequency, but two of the simplest models (*i.e.*, each with only two parameters) are found to give extremely good performance in general. These are the Hall and alpha-stable (or α-stable) models, both of which

approximate the Rayleigh distribution for low amplitude values but decay with an inverse power law for high amplitude values. It is concluded that the Hall model is the optimal choice in terms of accuracy and simplicity for locations exposed to heavy sferic activity (*e.g.*, low-latitude regions), and the α-stable model is best for locations relatively distant from heavy sferic activity (*e.g.*, high-latitude regions).

Based on the statistical characteristics of the noise data, a new clustering Poisson atmospheric noise model is developed. This model is based on several previously known statistical-physical models, but in addition takes into account the clustering of sferic impulses. It is shown that the clustering model accurately predicts the statistical features found in low-frequency radio noise data.

Finally, since many low-frequency digital communication systems operate in high-latitude regions, which are relatively distant from heavy sferic activity, it is of value to compare the bit error rate (BER) performance of receivers specifically designed for α-stable noise with the BER performance of conventional low-frequency receivers. The communication signal formats examined are quadrature phase-shift keying (QPSK) and 16 point quadrature amplitude modulation (16 QAM). Hundreds of simulations using time-series data from various times and locations and at various center frequencies and bandwidths are performed, and the following results are found uniformly: for QPSK signals, virtually no performance improvement is gained when using an α-stable receiver instead of the best conventional receiver, but for 16 QAM signals, an improvement of several dB is gained by using an α-stable receiver.

Acknowledgments

In this section, I wish to acknowledge those responsible for the success of my research project at Stanford.

First and foremost, I wish to thank Professor Antony C. Fraser-Smith, my principal research adviser, for his technical guidance and financial support throughout the duration of my work. I also thank him for his wisdom regarding numerous aspects of life and his example as a great person, for these have left impressions that will last well beyond my stay at Stanford.

In addition, I would like to thank the following individuals: Professor Robert A. Helliwell, my associate adviser, for his infusion of ideas and energy into this research project from beginning to end; Professor Abbas El Gamal, for suggestions that greatly improved the results of Chapter 4 and for a variety of worthwhile interactions during my time at Stanford; and Professor Howard Zebker, for serving as the fourth member of my defense panel.

Acknowledgments also go to Professor Dwight Nishimura, Marianne Marx and Hadar Avi-Itzhak for helping me become established at Stanford; to Thomas Liu for his useful suggestions throughout this research; to my parents for their tireless efforts to enhance my education and quality of life; and to all my family and friends (especially Kim) who were supportive along the way.

Contents

List of Tables

List of Figures

Chapter 1

Introduction

Naturally occurring radio noise above approximately 100 MHz is well modeled for most applications as a Gaussian random process; however, atmospheric radio noise below 100 MHz is often impulsive in nature and is not well modeled as Gaussian. Atmospheric events (mainly lightning strokes, which create electromagnetic emissions known as *sferics*) produce large, clustered impulses in the noise waveform seen at a receiving antenna, causing the waveform to vary greatly from typical Gaussian background noise. Due to large variations in sferic activity on a seasonal and diurnal basis and with the passing of individual storms, atmospheric noise is also non-stationary.

The objective of this work is the statistical analysis, characterization and modeling of atmospheric radio noise in the frequency range 10 Hz – 60 kHz, with the specific goal of improving communication systems operating in this range. The analyses are based on many thousands of hours of measurements made by the Stanford Radio Noise Survey System.

This chapter begins with an overview of 10 Hz – 60 kHz radio noise, which includes most or all of the extremely-low frequency (ELF; 3 Hz – 3 kHz), very-low frequency (VLF; 3 kHz – 30 kHz) and low frequency (LF; 30 kHz – 300 kHz) bands. Following this overview is a description of the measurement systems used to collect the noise data. The contents of each chapter are then summarized, and finally, the main contributions of the dissertation are presented. From this point on, the

terms ELF, VLF and LF refer to the individual frequency bands, while the term *low-frequency* refers specifically to the 10 Hz – 60 kHz range measured by the Noise Survey System.

1.1 ELF/VLF/LF Noise

ELF/VLF/LF radio noise is comprised of both man-made and natural signals. Examples of man-made signals are power line harmonics, communication signals and interference from electrically powered machinery; naturally occurring noise includes sferics, whistlers, polar chorus and auroral hiss. Naturally occurring noise is discussed below, but for a more thorough treatment see Helliwell [24].

Sferics are typically the dominant source of naturally occurring low-frequency radio noise. Even though lightning activity mainly occurs in tropical regions (and thus at lower latitudes), sferics can propagate for thousands of miles with little attenuation, so they are seen in noise data worldwide. The amount of sferic activity in a given noise sample depends on the worldwide source distribution of lightning relative to the receiver location, with nearby storms contributing a great deal and distant storms contributing less.

Whistlers are bursts of electromagnetic energy that travel into the ionosphere, follow the lines of force of the earth's magnetic field, and come back into the atmosphere at roughly the same latitude and longitude in the opposite hemisphere. The dispersion of the medium in which they travel causes them to have a time-frequency characteristic that sounds like a "chirp" or "whistle" when converted to an audible signal.

Polar chorus and auroral hiss are VLF emissions that are generated in the ionosphere and/or magnetosphere and have distinct spectral signatures. Both are found primarily in the polar regions. Polar chorus refers to sequences of discrete signals that often come in bursts and have a chirping frequency characteristic; auroral hiss is thermal-like noise within a given bandpass frequency range. At high-latitude sites, it is possible for auroral hiss to dominate the noise completely and drown out even the strongest sferics.
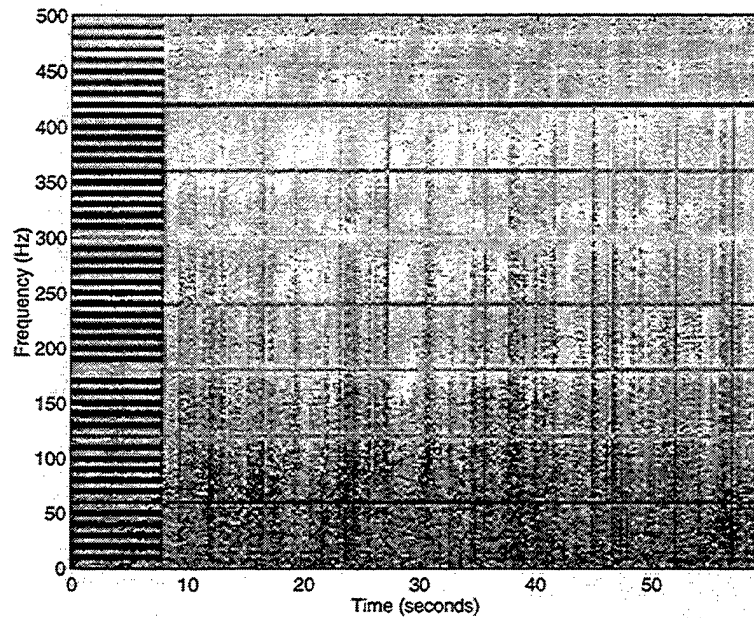
Figure 1.1: Stanford ELF Spectrogram, 25 August 1987, at 00:04 UT.

It must be noted that none of the radio noise analyzed in this dissertation is comprised of whistlers, chorus or hiss to a noticeable degree, so the results contained within are only known to apply to atmospheric noise.

1.1.1   Spectral Content

A sample ELF spectrogram from Stanford, California, is shown in Figure 1.1. The first eight seconds include a calibration tone: harmonics spaced 10 Hz apart with 10 pico-Tesla (pT) magnitudes. It is easily seen from the calibration tone that notch filters are installed at 60, 120, 180 and 300 Hz, in order to help remove power line harmonics that otherwise would use up most of the dynamic range. The rolloff above 400 Hz is due to an anti-aliasing filter. The vertical lines are sferics, each representing a lightning stroke that could be many thousands of kilometers away.

A sample VLF spectrogram for eight seconds of Arrival Heights data is shown in Figure 1.2. The first one second includes a calibration tone: harmonics spaced 250 Hz apart with 0.1 pT magnitudes. There is a single pole highpass filter with a cutoff frequency of 5 kHz to remove power line harmonics. Once again a number of sferics
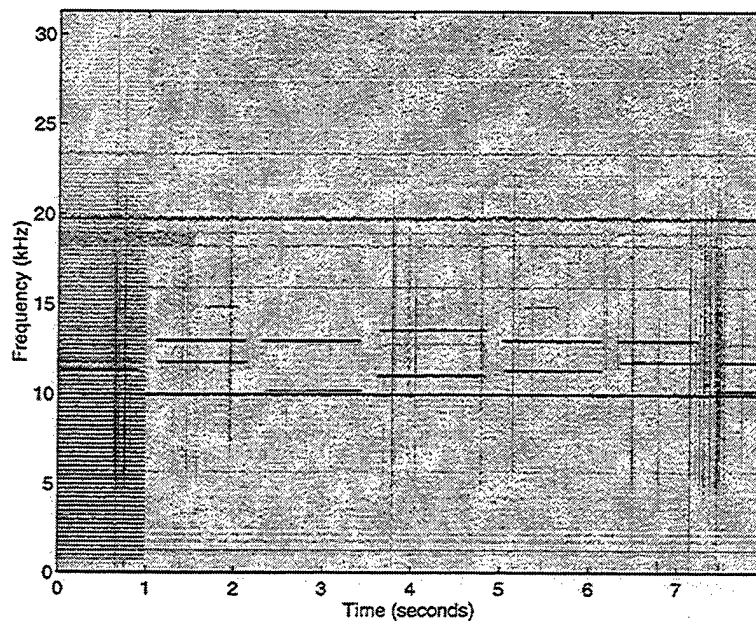
Figure 1.2: Arrival Heights VLF Spectrogram, 08 May 1995, at 16:05 UT.

can be seen, the strongest of which occur at 0.7, 6.5 and 7.4 seconds. The line at 10 kHz is an instrumentation signal, and the dashed horizontal lines between 10 kHz and 14 kHz on the order of one second in length are from the Omega navigation system [27]. The horizontal lines above 15 kHz are from communication systems, primarily phase shift keyed digital systems transmitting on the order of 100 – 200 baud. When these lines are crossed by the dark vertical lines, sferics are likely to be causing bit errors.

A sample VLF spectrogram for eight seconds of Grafton, New Hampshire data is shown in Figure 1.3. A great deal of sferic activity is seen, and the sferics are strong enough to clearly dominate the calibration tone. This is because Grafton is much closer to thunderstorm activity than Arrival Heights, and in addition July is the peak of the North American storm season and 00 UT is the peak of the North American diurnal cycle [3, 5]. The term *heavy sferic activity* is used throughout this dissertation to refer to the condition of numerous (and often overlapping) sferics as seen in Figure 1.3, while the term *light sferic activity* is used to describe the condition of sporadic (but possibly large) impulses as in Figure 1.2.
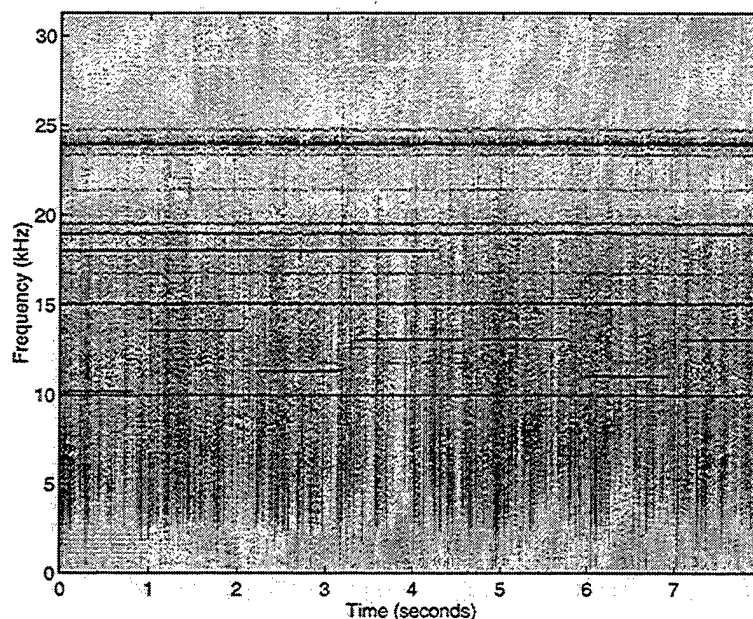
Figure 1.3: Grafton, New Hampshire VLF Spectrogram, 20 July 1988, at 00:05 UT.

It is seen in Figures 1.1 to 1.3 that power decreases with increasing frequency above a given range; this is due to the physical mechanism of lightning and to propagation effects. The power spectral density of low-frequency radio noise falls off in general as f^{-2} up to 2 – 3 kHz, rises up to 10 kHz, then drops off steeply (greater than f^{-4}) throughout the VLF and LF ranges [25, 28]. Propagation mode changes due to the earth-ionosphere waveguide cutoff account for the 2 – 10 kHz amplitude change.

1.2 The Stanford ELF/VLF Radio Noise Survey

During the years 1985-1986, eight ELF/VLF (10 Hz – 32 kHz) radio noise measurement systems, or radiometers, were installed at a variety of high-latitude and mid-latitude sites in an effort to fill large gaps in the information available on radio noise in this frequency range [13, 14]. Other ELF/VLF measurement systems have been implemented in the past, but this is the only system of its kind in terms of its geographic coverage and continuity of simultaneous data collection. The project was

a follow-on to a number of previous atmospheric, ionospheric and magnetospheric studies conducted by the Space, Telecommunications and Radioscience (STAR) laboratory at Stanford (*e.g.,* Bell and Helliwell [1, 24]).

The radiometers are located at Arrival Heights, Antarctica (AH; $78°S$, $167°E$); Dunedin, New Zealand (DU; $46°S$, $170°E$); Grafton, New Hampshire (GN; $44°N$, $72°W$); Kochi, Japan (KO; $33°N$, $133°E$); L'Aquila, Italy (AQ; $42°N$, $13°E$); Søndrestromfjørd, Greenland (SS; $67°N$, $51°W$); Stanford, California (SU; $37°N$, $122°W$); and Thule, Greenland (TH; $77°N$, $69°W$). Most of the stations operated much longer than program expectations, and the systems at Stanford and Arrival Heights are still operating. They should be able to collect data beyond one solar cycle. A complete technical description of the radiometers is provided in Fraser-Smith and Helliwell [13], so only an overview is presented here.

Each radiometer contains two receivers, one for the 10 – 400 Hz frequency range (designated ELF) and the other for the 400 Hz – 32 kHz frequency range (designated VLF). Each receiver has its own pair of crossed loop antennas, one oriented in the N–S geomagnetic direction and the other in the E–W geomagnetic direction. The ELF antennas are 1164 turn coils that are either buried or enclosed in order to prevent noise due to wind induced motion of the coils in the earth's magnetic field. The VLF antennas are single-turn triangular above-ground loops 18 meters wide and 9 meters high. The Thule, Greenland station has an additional receiver containing a downconverter with a 30 kHz translation frequency, thus allowing data in the lower part of the LF range (30 kHz – 60 kHz) to be collected and analyzed.

1.2.1 Noise Amplitude Data

Continuous data collection is obtained from the radiometers by monitoring the outputs of a bank of sixteen narrowband channel filters with center frequencies distributed roughly logarithmically across the 10 Hz – 32 kHz band. Each of the 32 filters (the N-S and E-W loops must be filtered separately) is a six pole Chebychev bandpass filter with a two-sided bandwidth equal to five percent of the center frequency. The sixteen center frequencies and bandwidths are listed in Table 1.1: the

Channel	Frequency	Bandwidth
1	10 Hz	0.5 Hz
2	30	1.5
3	80	4
4	135	6.75
5	275	13.75
6	380	19
7	500	25
8	750 Hz	37.5
9	1 kHz	50
10	1.5	75
11	2	100
12	3	150
13	4	200
14	8	400
15	10.2	510
16	32 kHz	1600 Hz

Table 1.1: Center frequencies and bandwidths for the 16 narrowband channels of the ELF/VLF radiometer.

first six are within the ELF receiver's frequency range and the last ten are within the VLF receiver's. The 10.2 kHz center frequency of channel 15 was chosen specifically to record signals from the Omega Navigation System (for propagation studies), but the other center frequencies were chosen to be free of man-made interference.

Each filter's output is passed through an analog root-mean-square (RMS) detector that squares the input, performs a time average, and outputs the square root of the average. The RMS detector output is then sampled at a rate of ten times per second by an analog to digital converter and sent to a digital computer, which then computes the root-sum-square of the N–S and E–W detector outputs to determine the RMS amplitude of the horizontal component of magnetic field for each channel. The analog to digital converters have a useful dynamic range of 70 dB, but switchable gain amplifiers in the analog receiver circuitry increase the total system dynamic range to 100 dB. The measurements taken are of absolute noise levels.

In order to save digital tape space, the computer writes out only every tenth sample. However, it also stores the average and RMS values for each minute (600

samples), along with the minimum and maximum of the 600 values for that minute. The seasonal and diurnal variations reported in Chapter 2 are derived from these one minute average amplitudes.

1.2.2 Time-Series Data

ELF broadband time-series data are collected for one minute every half hour, and are sampled at a 1 kHz sampling rate by a 14 bit digital to analog converter. A 400 Hz lowpass filter is inserted before the D/A to prevent aliasing. The VLF and LF broadband time-series data are collected for one minute every hour; the sampling rate for these data is 62.5 kHz and the D/A converter is 16 bits. The anti-aliasing filter is set at either 20 kHz or 30 kHz depending on which part of the frequency spectrum is to be analyzed. (The 30 kHz filter allows some aliasing at lower frequencies but does not distort the 20 kHz – 30 kHz range). The LF data at Thule, once downconverted, are processed the same as the VLF data.

The ELF time-series data, like the noise amplitude data, are calibrated to absolute levels and digitally recorded. The VLF time-series data, however, are recorded to analog tape and digitized later. Due to concerns about the flatness of frequency response in the measurement process, the VLF time-series data are restricted to narrowband analyses and their amplitudes within a given frequency band of analysis are normalized to an expected value of one.

Only one axis (the N–S loop) is recorded for the time series data, so the data are collected with a direction dependent gain pattern. Fortunately, this is shown not to affect the theoretical results of the dissertation or the comparison of these results to the noise, but it does preclude the use of direction finding information in the statistical analysis of the noise.

1.3 Outline of the Dissertation

This dissertation is concerned with the statistical analysis and modeling of low-frequency radio noise and the improvement of low-frequency communications. Chapter 2 discusses statistical analysis results, Chapters 3 and 4 are concerned with noise modeling, and Chapter 5 addresses low-frequency communications.

The statistics analyzed in Chapter 2 include seasonal and diurnal variations, amplitude probability distributions (APDs), impulse interarrival time distributions, correlations between noise impulses, and background noise statistics. Noise characteristics derived from the analyses are presented, and are used in the following chapters to aid in the modeling problem.

In Chapter 3, APDs derived from thousands of hours of ELF/VLF/LF noise survey data are compared to the APDs of various low-frequency noise models. The most accurate model for representing low-frequency noise APDs is found to depend on geographic location, time of year and day, bandwidth, and center frequency, but two of the simplest models (*i.e.*, each with only two parameters) are found to give extremely good performance in general. These are the Hall and alpha-stable (or α-stable) models, both of which approximate the Rayleigh distribution for low amplitude values but decay with an inverse power law for high amplitude values. It is concluded that the Hall model is the optimal choice in terms of accuracy and simplicity for locations exposed to heavy sferic activity (*e.g.*, low-latitude regions), and the α-stable model is best for locations relatively distant from heavy sferic activity (*e.g.*, high-latitude regions).

Chapter 4 develops a new clustering Poisson atmospheric noise model based on the statistical characteristics of the noise data found in Chapters 2 and 3. This model is similar to several previously known statistical-physical models, but in addition accounts for the clustering of sferics. It is verified that the clustering model accurately predicts the statistical features found in low-frequency noise data.

Chapter 5 compares the bit error rate (BER) performance of receivers specifically designed for α-stable noise with that of conventional nonlinear analog receivers used

with impulsive noise, such as clippers, limiters and log-correlators. The communication signal formats examined are quadrature phase-shift keying (QPSK) and 16 point quadrature amplitude modulation (16 QAM). Hundreds of simulations using time-series data from various times and locations and at various center frequencies and bandwidths are performed, and the following results are found uniformly: for QPSK signals, virtually no performance improvement is gained when using an α-stable receiver instead of the best conventional receiver, but for 16 QAM signals, an improvement of several dB is gained by using an α-stable receiver.

Finally, Chapter 6 summarizes the main results of this dissertation and suggests topics of future research.

1.4 Contributions

Here is a brief summary of the contributions made in this dissertation.

- Statistical analysis of thousands of hours of globally collected low-frequency radio noise (Chapter 2).

- Comparison of APD models used for modeling low-frequency noise (Chapter 3).

- Development of a clustering Poisson model for atmospheric noise and proof that the model accurately predicts low-frequency noise statistics (Chapter 4).

- Comparison of receivers designed for α-stable noise to conventional receivers (Chapter 5).

Chapter 2

Measured Statistics

2.1 Introduction

This chapter presents an overview of some of the statistical characteristics of naturally occurring low-frequency radio noise. The statistical properties discussed include long-term noise averages, amplitude probability distributions, impulse interarrival time distributions, correlations between impulses, and background noise statistics.

2.2 Long-Term Noise Averages

The noise amplitude data described in Section 1.2.1 are collected continuously at the radiometer sites over long periods of time, and their absolute noise levels are well calibrated. It is thus possible to derive statistically significant seasonal and diurnal variations of ELF/VLF noise from them. Since the noise is primarily caused by lightning occurring throughout the world, these variations are related to seasonal weather patterns and global climate change [15]. This section provides an overview of the seasonal and diurnal variation calculations performed with the data; more extensive results are contained in [3, 4, 5].

To provide a basic context for the ELF/VLF noise amplitude measurements, Figure 2.1 shows the one hour average noise amplitudes over the course of one
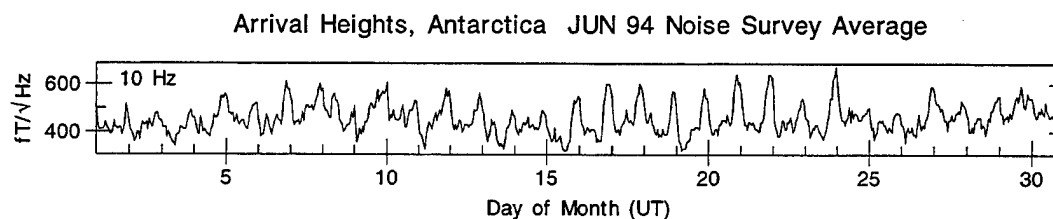
Figure 2.1: Noise averages in the 10 Hz frequency band recorded June 1994, at Arrival Heights, Antarctica. Each of the 720 points on this plot is an average of one hour of data.

month for one channel, the 10 Hz band measured at Arrival Heights during the month of June 1994. Each of the 720 points on this graph, representing one hour, is an average of roughly 32,000 noise filter output samples (not 36,000 because of calibration periods). The data consist of both random and diurnal variations; they sometimes show occasional short duration impulses due to both man-made and natural interference as well. The entire database contains thousands of these plots, one for each station, month and channel.

The unit $fT/\sqrt{Hz}$ is essentially the square root of power spectral density, obtained in this case by dividing the RMS filter amplitude output (in fT) by 0.707, the square root of the 0.5 Hz bandwidth for the 10 Hz channel filter. The data are presented in fT because the system detects magnetic field. The vertical electric field component and/or the power of the incoming signal may be obtained using 377 Ω as the impedance of free space, but this is an approximation (albeit usually a good one) that assumes the impinging electromagnetic waves are planar. To convert to electric field under this assumption, the relation $B = \sqrt{\mu_0 \epsilon_0} E = E/c$ may be used to determine that 1 fT is equivalent to $0.300 \, \mu V/m$. If it is desired to relate magnetic field (or magnetic flux density) B to magnetic intensity H, the relation $B = \mu_0 H$ can be used to find that 1 fT is equivalent to $7.958 \times 10^{-4} \, \mu A/m$.

2.2.1 Seasonal Variations

Determining the seasonal variations of natural radio noise over the course of many years requires two steps: (i) monthly averages are computed for each station, month,

year, and frequency band (*i.e.*, all the data in Figure 2.1 are averaged to come up with one number for June 1994 at Arrival Heights in the 10 Hz frequency band), and (ii) all the years are then averaged together, resulting in an overall variation by month at each station and in each band.

Figures 2.2 and 2.3 show the monthly variations of the noise level for all channels at Stanford, California, and the error bars show the standard deviations from year to year, *i.e.*, a small error bar indicates little variation from one year to the next for that month. Note that the error bars are largely unrelated to the standard deviation of individual noise samples, which can be quite large; they are also unrelated to the standard deviation of the total average, which is minute since each point on these plots is an average of millions of sample values. Note that each individual graph has its own scale. All 24 hours of each day are included; for seasonal variations using only specific diurnal time periods, refer to [3].

A strong annual variation with a peak in the northern hemisphere summer can be seen in most of the frequency channels at Stanford. Although not shown, it exists at Søndrestrøm as well. Arrival Heights and Dunedin, however, have some variations with a peak in the northern hemisphere winter. The differences between annual variations among stations and from channel to channel can be attributed to different patterns in local and distant lightning, with the higher frequency variations being influenced more strongly by closer sources. The seasonal variation of global lightning is such that southern hemisphere locations are generally more active in the northern hemisphere winter and northern hemisphere locations are more active in the northern hemisphere summer [4, 19].

In Figure 2.3, for frequencies in the range 1 – 1.5 kHz, the error bars are too large relative to the data to extract a statistically significant seasonal variation. This band is within the range of the earth-ionosphere waveguide cutoff frequencies, where noise does not propagate far and the receiver predominantly picks up the fields from local sources. In addition, the 32 kHz band at Stanford is known to be contaminated by man-made noise, resulting in a weak variation with large error bars.

At the other frequencies, however, a monthly variation strongly dominates the uncertainty of the error bars. Given the number of data points and years involved,
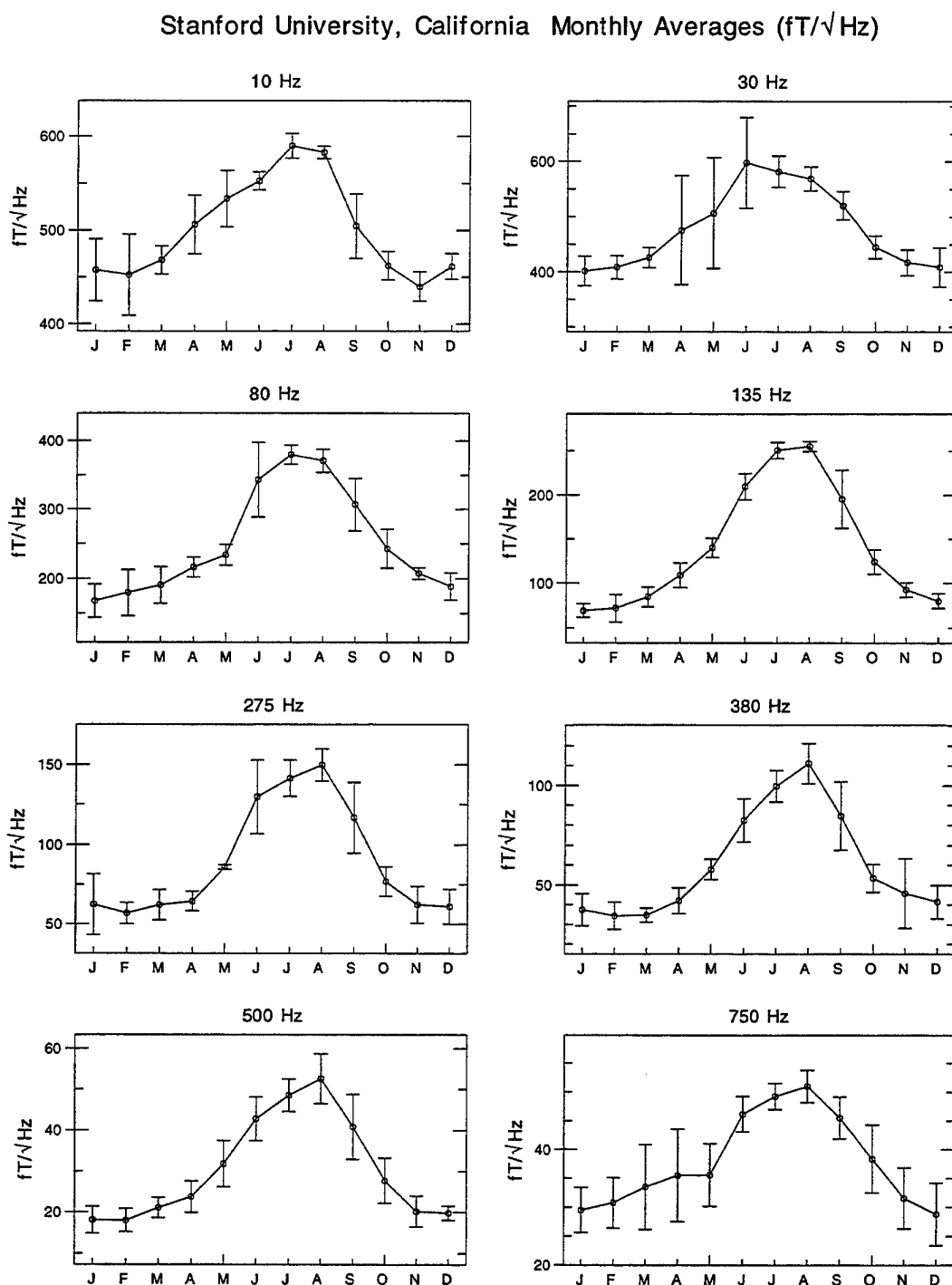
Figure 2.2: Monthly variation of ELF/VLF radio noise at Stanford, California, for the eight lowest-frequency channels. The years 1986 to 1993 are included.
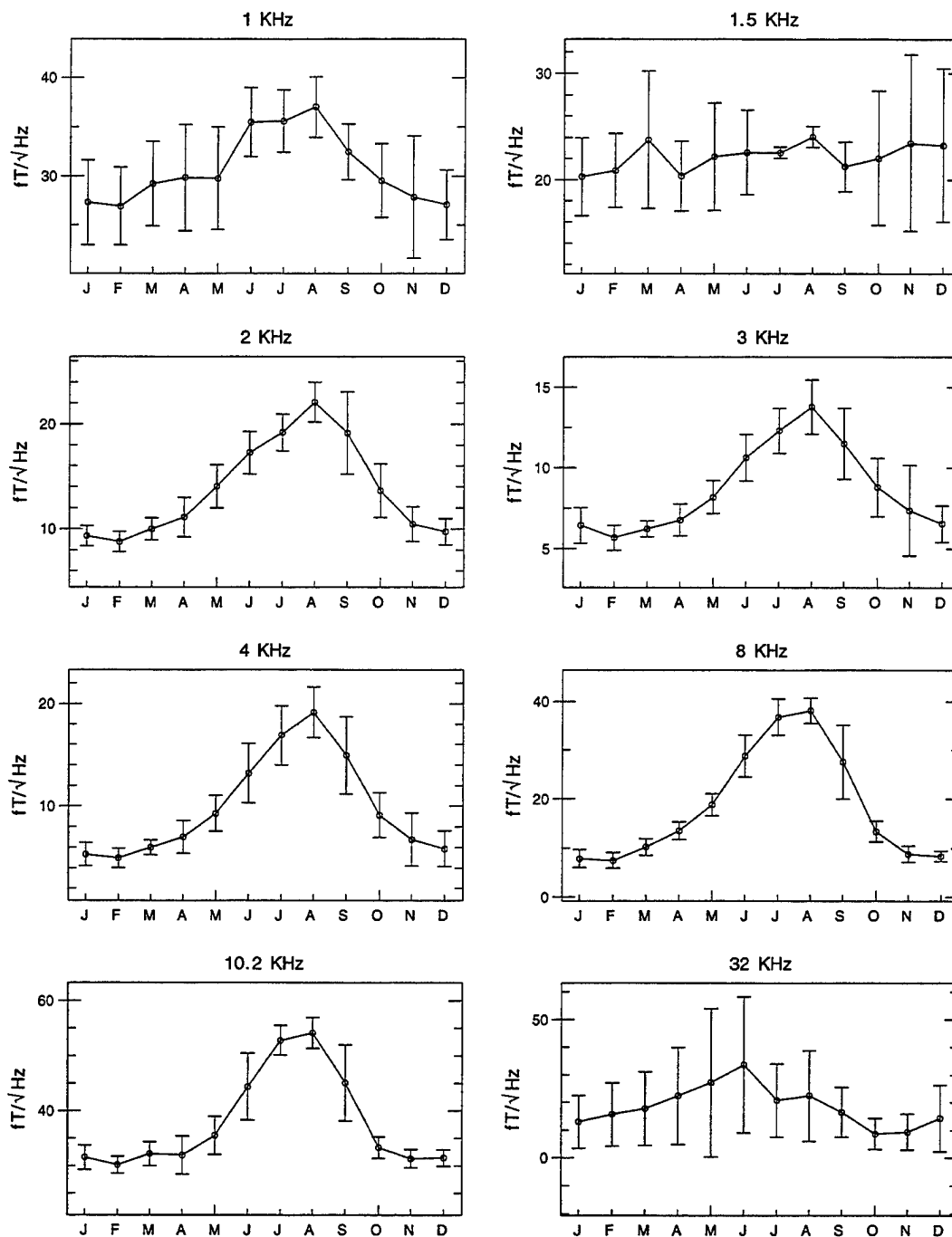
Figure 2.3: Monthly variation of ELF/VLF radio noise at Stanford, California, for the eight highest-frequency channels. The years 1986 to 1993 are included.

this reflects a definite seasonal trend in source quantity (*i.e.* lightning flash rate) and/or location. It is shown in [4] that the seasonal variations seen in the data correlate strongly with estimates of global lightning flash rates.

2.2.2 Diurnal Variations

Figures 2.4 and 2.5 show diurnal variations of the noise level for January and July at Arrival Heights, Antarctica, for the eight lowest frequency channels. The error bars indicate the standard deviations from year to year, *i.e.*, small error bars indicate little variation from one year to the next in the diurnal cycle of a particular month. Once again, the error bars are largely unrelated to the standard deviation of individual noise samples or to the standard deviation of the total average.

Changes in average noise levels from year to year for each month are removed from the error bar calculations, since otherwise they would artificially enlarge the diurnal variation error bars. The normalization is performed in three parts: (i) for each month and year, a noise average for the entire month is computed to produce a single value, (ii) for each month, the resulting values from (i) for the different years are averaged together to give one total average reference value per month, and (iii) all the data are normalized (by subtracting the difference between the corresponding values from parts (i) and (ii)) such that differences in total monthly averages from year to year are removed, *i.e.*, each total monthly average now equals that month's reference value. Thus the error bars are truly an indication of the variation of the diurnal cycle. In most cases the error bars are small compared to their respective data, indicating little variation of diurnal cycles from year to year.

Arrival Heights (at 77.8° *S* latitude) sees roughly equal contributions from storms at all longitudes, especially at the lowest frequencies. The 10 Hz band thus exhibits a diurnal pattern in phase with the overall worldwide distribution, a broad peak from 14-22 UT, as clearly seen in Figure 2.4. From June to September, however, the peak shifts to roughly 22-00 UT, as seen in Figure 2.5. This indicates a strong contribution from North American storms during their peak season [15].

Although not shown, large diurnal variations are seen in most of the frequency
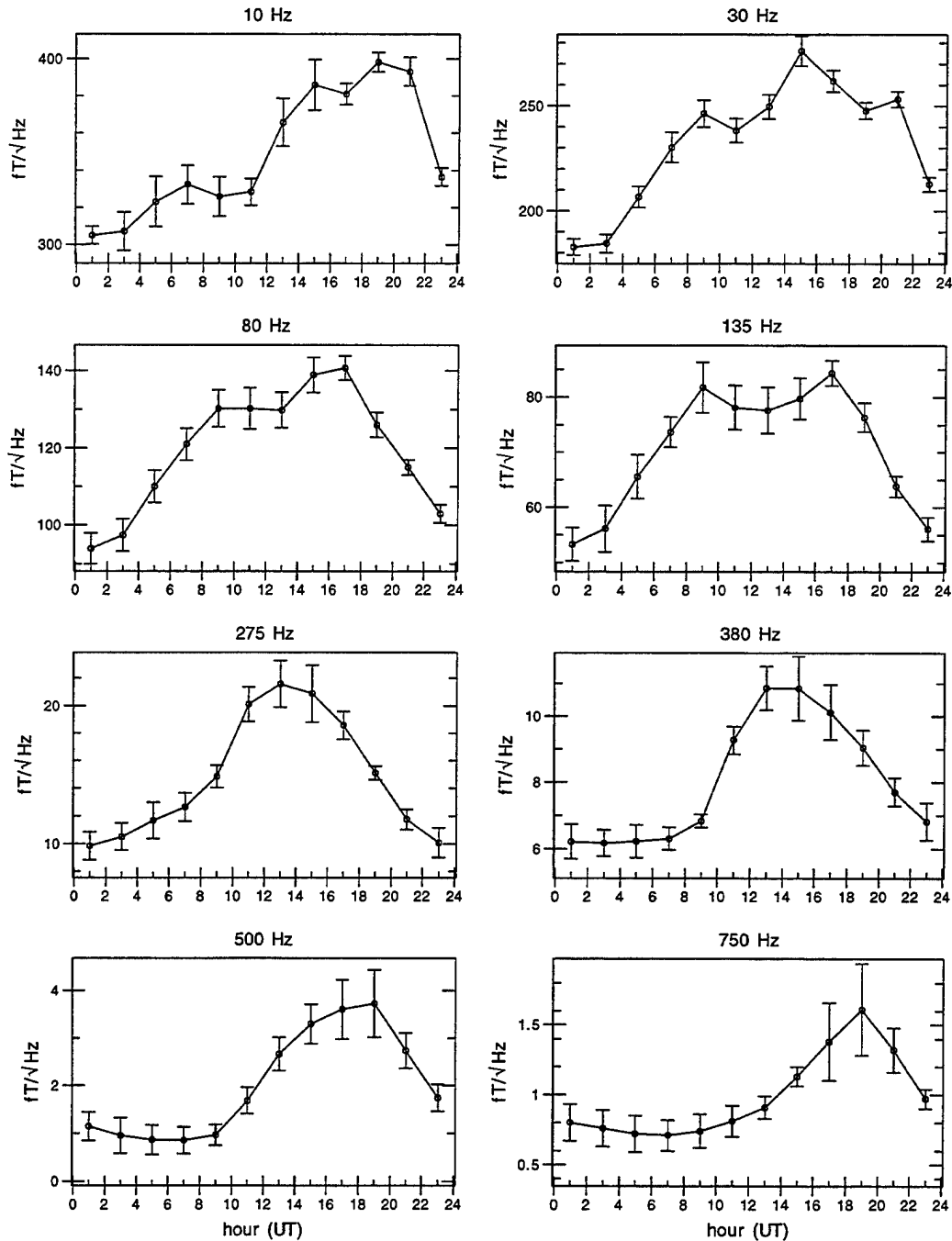
Figure 2.4: Diurnal variation of ELF/VLF radio noise at Arrival Heights, Antarctica, during the month of January for the eight lowest-frequency channels. The years 1985 to 1994 are included.
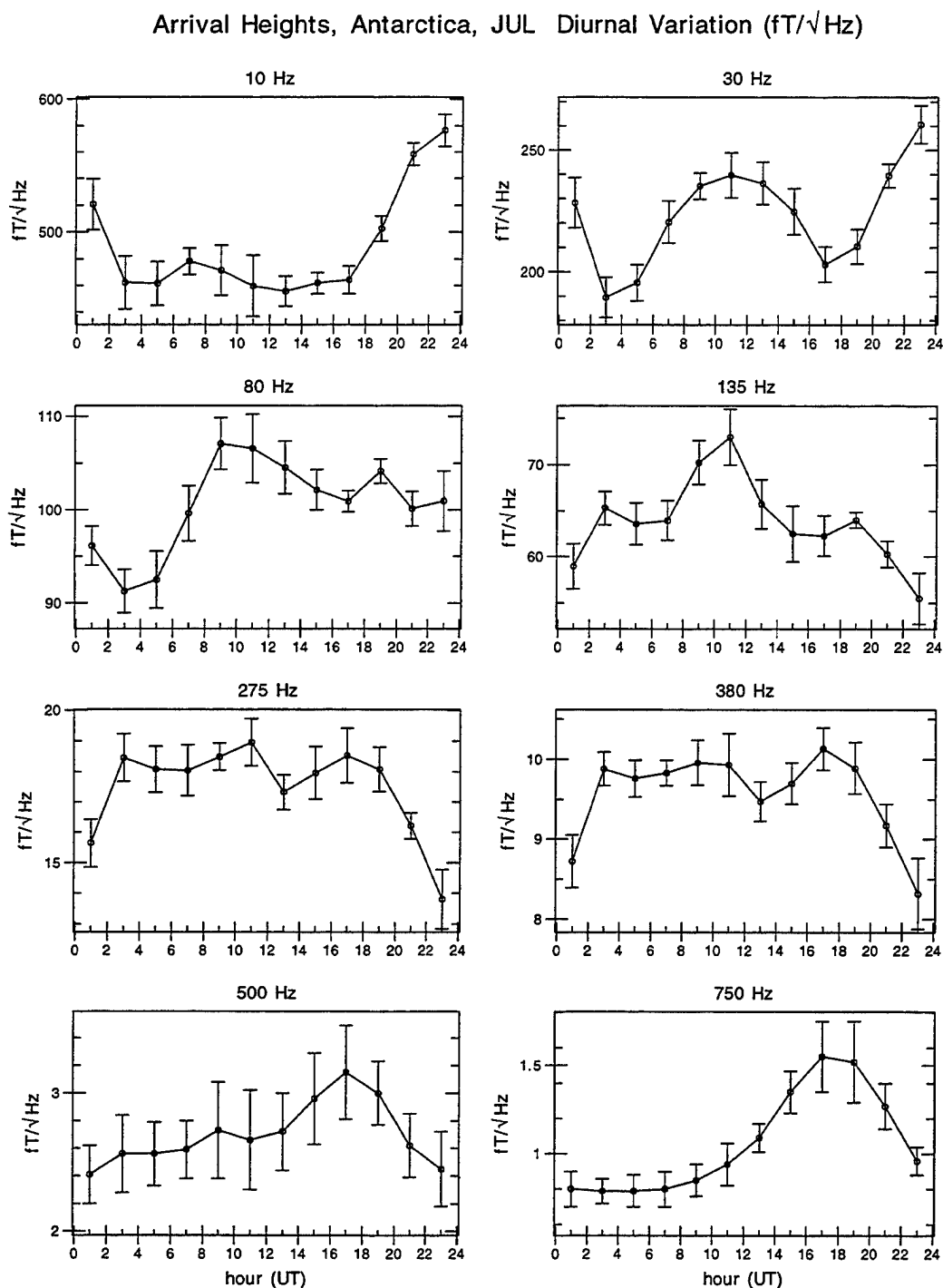
Figure 2.5: Diurnal variation of ELF/VLF radio noise at Arrival Heights, Antarctica, during the month of July for the eight lowest-frequency channels. The years 1985 to 1994 are included.

channels at most of the stations [5]. However, the phases of these diurnal variations can depend strongly on month, frequency, and especially station. Variation by station is primarily due to the diurnal signature of global lightning, for which it is known that lightning over North America peaks at roughly 00 UT, lightning over South America peaks at roughly 20 UT, lightning over Europe and Africa peaks at roughly 16 UT, and lightning over Southeast Asia peaks at roughly 08 UT [15, 19]. The differences in diurnal variations with respect to frequency can be attributed to different patterns in local and distant lightning, with the higher frequency variations being influenced more strongly by closer sources.

2.3 Amplitude Probability Distributions

The most measured and modeled statistic of low-frequency radio noise, next to absolute power level, is the first-order APD. This section gives an overview of APD characteristics; APD modeling is covered in Chapters 3 and 4.

Since wideband time-series data generally contain significant man-made interference, the noise APD is usually analyzed within a relatively narrow frequency range. In such narrowband analysis, the broadband time-series data are digitally downconverted (*i.e.,* frequency translated) using various center frequencies, and low-pass filtered using various cutoff frequencies. Statistics are then derived from the resulting lowpass equivalent signals.

A narrowband signal $n(t)$ can be written

$$n(t) = n_I(t) \cos(2\pi f t) - n_Q(t) \sin(2\pi f t), \qquad (2.1)$$

where $n_I(t)$ is the inphase component, $n_Q(t)$ is the quadrature component, and f is the center frequency. The signals $n_I(t)$ and $n_Q(t)$ are then lowpass signals with bandwidth much smaller than f. The complex-analytic representation is written

$$n(t) = A(t)e^{j(2\pi f t + \Theta(t))}, \qquad (2.2)$$

where the magnitude (or envelope) $A(t)$ is

$$A(t) = \sqrt{n_I^2(t) + n_Q^2(t)}, \tag{2.3}$$

and the phase $\Theta(t)$ is

$$\Theta(t) = \arctan \frac{n_Q(t)}{n_I(t)}. \tag{2.4}$$

Using this latter notation the signal $n(t)$ can also be written

$$n(t) = \Re[A(t)e^{j(2\pi ft + \Theta(t))}], \tag{2.5}$$

where $\Re()$ indicates the real part of the argument.

The noise envelope $A(t)$ is a random process, and its first-order statistics at a given time are specified by its APD. The APD is defined as the probability that the noise envelope A takes on a value larger than some given value a: $P(A > a)$. Other commonly used statistical definitions that characterize $A(t)$ are (i) the cumulative distribution function (CDF), $F_A(a)$, which is one minus the APD, (ii) the probability density function (pdf), $f_A(a)$, which is the derivative of the CDF, and (iii) the voltage deviation V_d, defined as $10 \log(E[A^2]/E^2[A])$, which serves as an indicator of the impulsiveness of the noise. The phase $\Theta(t)$ of atmospheric noise has long been known to have a distribution that is uniform over the angles $-\pi$ to π [33]; several checks on the noise survey data provide additional evidence that this is true.

Since low-frequency noise is thought of as Gaussian noise plus an impulsive noise component, its pdf looks like a bell curve but with heavier tails. Likewise, since the envelope distribution of Gaussian noise is Rayleigh, the envelope distribution of low-frequency noise appears Rayleigh but with a heavier tail. The difference between a typical low-frequency noise envelope pdf and the Rayleigh pdf is shown in Figure 2.6, for July 1986 data from Thule, Greenland, in the 35.6 – 37.6 kHz range. Noise envelope pdf's are found to decay with an inverse power law for large values (out to some limit set by the dynamic range of the system), so the Rayleigh pdf has a tail that rolls off too quickly to accurately represent the noise data pdf.
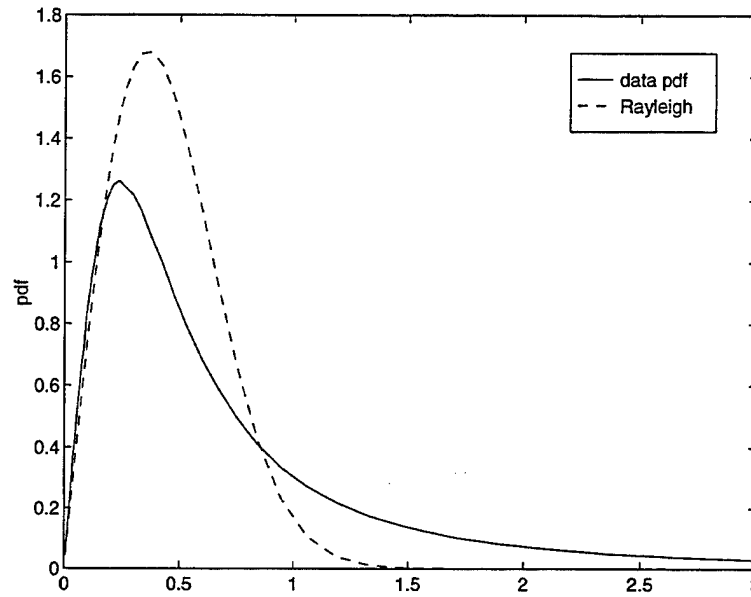
Figure 2.6: Thule envelope pdf compared to a Rayleigh distribution with the same initial slope. The data are normalized such that $E[A] = 1$.

2.4   Impulse Interarrival Distributions

Thousands of hours of ELF/VLF/LF data were analyzed to determine impulse interarrival distributions. In each case, a set of threshold values (and their negatives) were chosen such as in Figure 2.7, a plot of 52 seconds of ELF broadband time-series data. For each occurrence of an upward crossing of a given positive threshold value or a downward crossing of the respective negative threshold value, the following are noted: (i) time of occurrence of the threshold crossing, linearly extrapolated from the two samples between which the level is crossed, (ii) the maximum (or minimum) extent of the sferic, and (iii) the amount of time the noise remains above (or below) the threshold crossing (i.e., the duration, also linearly extrapolated from the two closest sample values). Crossings less than one millisecond apart are assumed to be from the same impulsive waveform and are ignored. For a given +/− threshold value, all positive and negative sferics are treated together, and the time differences are determined from one sferic to the next. The result is a set of impulse spacings, or interarrival times.
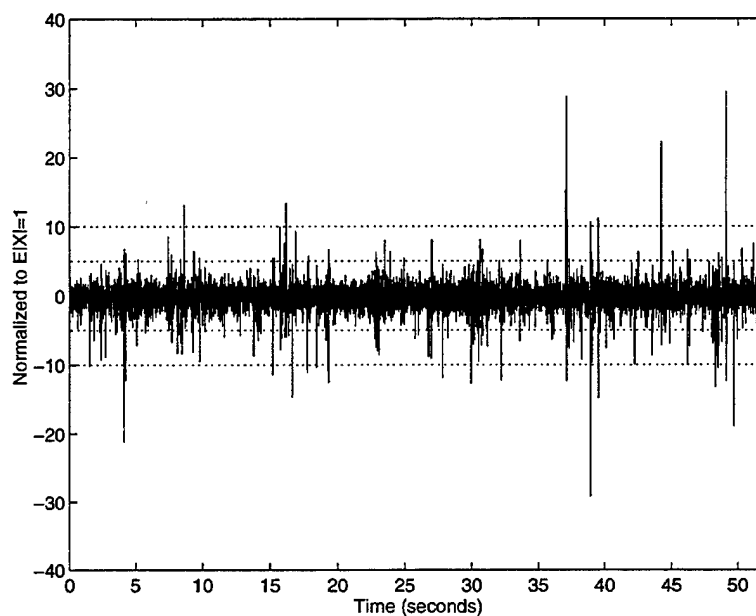
Figure 2.7: Stanford ELF broadband data, 01 April 1990, at 01:04 UT. Dotted lines are shown at ±5 and ±10 times the norm of the noise.
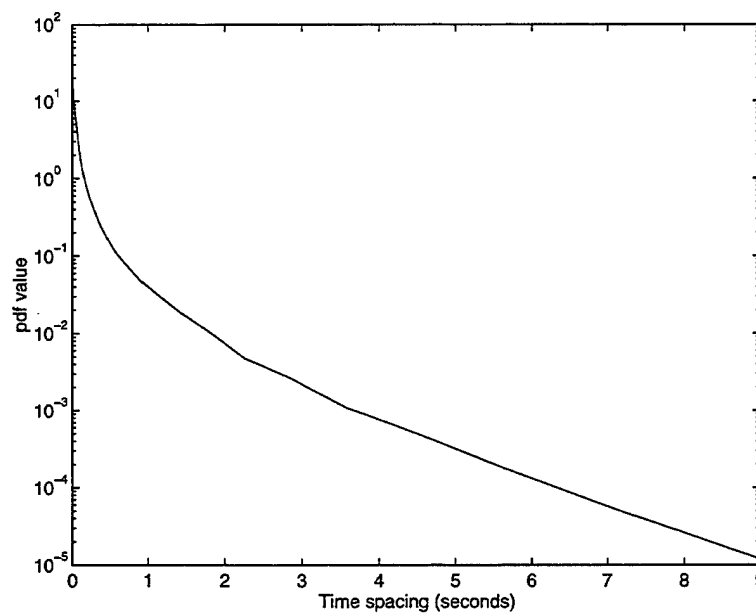
Figure 2.8: Impulse interarrival pdf for Arrival Heights, December 1995, for the 25.5 – 27.5 kHz noise band, with the impulse detection threshold set at 20 times the norm of the noise.

The set of successive interarrival times $T_I(k)$ form a discrete random process. The marginal pdf of $T_I(k)$ is assumed not to depend on the index k, and so can be found from a histogram of the interarrival times of the data. For every data sample analyzed, the resulting interarrival time pdf $f_{T_I}(t)$ was found to be of the form of Figure 2.8; this figure shows $f_{T_I}(t)$ for Arrival Heights December 1995 data in the 25.5 – 27.5 kHz noise band, with the impulse threshold set at 20 times the norm of the noise.

Since Figure 2.8 has a logarithmic ordinate axis, functions of the form $ce^{-\lambda t}$ appear as straight lines with slope $-\lambda$ and intercept $\log c$. Thus an exponential pdf, indicative of a simple Poisson process, would appear as a straight line. In all the data and for all threshold values, an approximately straight line is found for times greater than roughly one second. For values of T_I between zero and one, however, the slope is more steeply downward curving. This implies clustering, since it indicates that many of the impulses are bunched together with short times between them. Section 4.4 shows that a clustering Poisson assumption predicts the behavior of the pdf $f_{T_I}(t)$ very well.

2.5 Correlations Between Impulses

Since the magnitude and direction of each sferic's threshold crossing is noted, it is possible to check for correlations between maximum amplitude levels of adjacent impulses and also between maximum amplitudes and interarrival times. In all the data samples examined and at a variety of threshold levels, however, no significant correlations were found in adjacent amplitude levels or between amplitudes and interarrival times, validating certain independence assumptions of the model to be proposed in Section 4.2.2. The correlation coefficient between adjacent interarrival times is roughly .15 – .20.

2.6   Background Noise Statistics

As mentioned previously, it has long been held that atmospheric noise can be viewed as a superposition of Gaussian noise and distinct impulses [12, 17]. The Gaussian component is the *background* noise, which results from the superposition of numerous low-level sources, including distant sferics. The impulses are caused by lighting from relatively nearby thunderstorms.

For narrowband noise with bandwidth B, the background noise samples are commonly modeled as independent if they are spaced at the Nyquist rate 1/2B. This assumption about the noise survey data is tested by removing all the noise impulses that stand out above the background noise level and performing correlation statistics on the samples that are left (usually more than 95% of them). It is found that the resulting background noise is indeed well modeled as white Gaussian noise (WGN), albeit with the tails chopped off. This characteristic is used in the receiver design problem of Chapter 5.

2.7   Conclusions

This chapter sets the framework for the rest of the dissertation by introducing some of the statistical properties of low-frequency radio noise. These properties are used in the following chapters to derive both models of the noise and receiver structures for communicating in it. The primary results of this chapter are:

- Seasonal and Diurnal variations correlate well with global lightning patterns and can be used to track global climate change.

- The narrowband noise envelope pdf of low-frequency noise has the functional form of a Rayleigh pdf at low values of dynamic range but decays with an inverse power law for high values.

- Impulse interarrival time distributions indicate clustering of sferics with bursts on the order of one second in length.

- No appreciable correlations are found between the maximum amplitudes of adjacent sferics or between these maximum amplitudes and interarrival times.

- Low-frequency noise can be viewed as the superposition of white Gaussian noise and clustered noise impulses from sferics.

Chapter 3

Comparison of APD Models

3.1   Introduction

It is stated in Chapter 2 that one of the most commonly modeled statistics in atmospheric noise studies is the noise envelope APD, or equivalently the pdf. In this chapter, the first-order amplitude probability distributions of ELF/VLF/LF noise data are determined and compared to several noise models used in recent literature: the Hall model [23], the Field-Lewinstein (or F-L) model [12] and the α-stable model [40]. These were chosen over a number of other noise models because of their popularity, accuracy and relative simplicity.

For a given data histogram, each model's parameters are adjusted to minimize the expected value of the log error squared between the histogram and the model's estimate of it. This log error metric, called the mean-square log error (MSLE), is defined as

$$\text{MSLE} = \int f(x) \left(\log_{10} \frac{f(x)}{\hat{f}(x)} \right)^2 dx, \qquad (3.1)$$

where $f(x)$ is the data pdf and $\hat{f}(x)$ is the model's estimate of it. Note that the expression (3.1) is similar to the *relative entropy* definition in information theory [6], except for squaring the term in parentheses.

After optimizing the parameters of each model, the minimum errors achieved for the individual models are compared and the best model is determined. The

26

best model depends on geographic location, time of year and day, frequency, and bandwidth, but the Hall and α-stable models are found to give extremely good performance in general. Both models have Rayleigh characteristics for low amplitude values but decay with an inverse power law for high amplitude values. The results show that the Hall model is the optimal choice in terms of accuracy and simplicity for locations exposed to heavy sferic activity (*e.g.,* low-latitude regions), and the α-stable model is best for locations relatively distant from heavy sferic activity (*e.g.,* high-latitude regions). In addition, the commonly used *voltage deviation* (V_d) parameter is found to be only weakly related to the amount of sferic activity in the noise waveform.

3.2   Amplitude pdf Models

Extensive research has been conducted for over forty years in order to characterize and model the first-order APDs of atmospheric radio noise (*e.g.,* [7, 33, 36, 47]). Some APD models are based entirely on intuitive reasoning and/or fitting the data to mathematical functions (these are called empirical models); others start with assumptions on noise source distributions and the propagation of noise impulses to the receiver (statistical-physical models). Empirical models in general have been based on crude curve fittings to limited data, but nonetheless a number of good models have been developed, including the Hall and Field-Lewinstein models. They are typically simpler and more mathematically tractable than other models, but their parameters are often unrelated to the physical processes that create the noise.

Statistical-physical models take into account the underlying physical processes of impulsive noise, but usually are difficult to work with mathematically. Making them tractable often requires approximations that are known not to be true for atmospheric noise, such as assuming the impulsive sources are distributed independently and uniformly in space and time. Nonetheless, statistical-physical models prove useful in many applications.

The most widely known statistical-physical models are the class A and B noise models developed by Middleton [33]. These are not considered explicitly in this

dissertation due to their complexity, but the class B model proves to be very accurate since it is a generalization of both the Hall and α-stable models. It should be noted that class A noise is defined for cases in which the bandwidth of the input noise is comparable to or less than the detection bandwidth, and class B noise is defined for cases where the noise bandwidth is greater than the bandwidth of the detector (*i.e.* impulsive noise inputs produce transients in the receiver). It is the latter case that applies in this study, especially at lower latitudes, since the sferics in the noise data have much wider bandwidths than those used to analyze the noise.

The complete set of noise model distributions from which the Hall, α-stable and F-L were selected includes power-Rayleigh (or Weibull), Laplace, lognormal, hyperbolic, and any promising mixture processes or piecewise combinations of these, both with and without the Gaussian or Rayleigh distribution included as well. This encompasses most, if not all, of the commonly known APD models (*e.g.*, [16, 18, 34]).

3.2.1   Hall Model

The Hall Model is presented and explained extensively in [23], but only the first order pdf of the narrowband envelope A is needed here. The Hall model specifies this envelope pdf $f_A(a)$ as the two parameter distribution

$$f_A(a) = (m - 1)\gamma^{m-1} \frac{a}{[a^2 + \gamma^2]^{\frac{m+1}{2}}}, \ a \geq 0, \tag{3.2}$$

called the Hall pdf from this point on. The term γ is a scaling factor and the term m determines the impulsiveness of the noise. Note that A has infinite variance for $m \leq 3$.

3.2.2   Field-Lewinstein Model

The Field-Lewinstein model is an empirical model developed from the assumption that atmospheric noise is composed of impulsive noise superimposed on a background of low-level Gaussian noise. The envelope A is approximated as the sum of

a Rayleigh distributed random variable (for the Gaussian component) and a power-Rayleigh distributed random variable (for the impulsive component), so the envelope pdf is the convolution of the two densities:

$$f_A(a) = \frac{2a}{R_0^2} e^{-\frac{a^2}{R_0^2}} * \frac{\alpha a^{\alpha-1}}{R^\alpha} e^{-\left(\frac{a}{R}\right)^\alpha}, \ a \geq 0. \qquad (3.3)$$

Equation (3.3) is referred to as the F-L distribution from this point on. Note that it is a three parameter distribution with no closed form, so it is somewhat difficult to work with mathematically.

3.2.3 Alpha-Stable Model

The α-stable pdf is directly specified in the characteristic function domain. The characteristic function $\Phi_X(\omega)$ of a random variable X is essentially a Fourier transform of the pdf:

$$\Phi_X(\omega) = E[e^{j\omega X}] = \int_{-\infty}^{\infty} f_X(x) e^{j\omega x} \, dx,$$

and the α-stable characteristic function is defined as

$$\Phi_X(\omega) = e^{-\gamma|\omega|^\alpha},$$

a two parameter distribution. The general form of the distribution includes two more parameters, defining an absolute shift and a skew, but these may be eliminated by assuming the noise is distributed symmetrically about zero. (This the case for atmospheric noise time-series data).

For $\alpha = 2$ the characteristic function defines a Gaussian distribution with mean zero and variance 2γ; for $\alpha = 1$ it defines a Cauchy distribution with parameter γ. Thus the Cauchy and Gaussian distributions are forms of the α-stable distribution. For α close to two the distribution is essentially Gaussian but with heavier tails. The α-stable distribution for $\gamma = 1$ and various values of α is shown for positive values in Figure 3.1. A significant difference in tail rolloff is seen even for $\alpha = 1.95$ as compared to the Gaussian case, $\alpha = 2.0$.
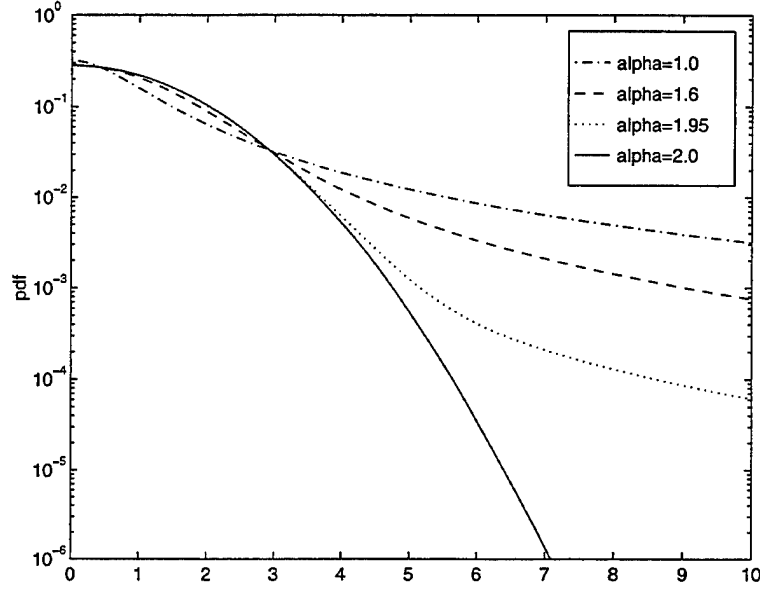
Figure 3.1: The α-stable pdf for $\alpha = 1.0$ (Cauchy), 1.6, 1.95 and 2.0 (Gaussian), and $\gamma = 1.0$; only positive abscissa values are shown.

If narrowband atmospheric noise is α-stable distributed, the inphase and quadrature components are jointly α-stable with characteristic function

$$\Phi_{X_I, X_Q}(\underline{\omega}) = E[e^{j(\omega_1 X_I + \omega_2 X_Q)}] = e^{-\gamma |\underline{\omega}|^\alpha}, \tag{3.4}$$

where $\underline{\omega} = (\omega_1, \omega_2)$. The corresponding envelope distribution is the Fourier-Bessel transform of $e^{-\gamma \rho^\alpha}$:

$$f_A(a) = a \int_0^\infty \rho e^{-\gamma \rho^\alpha} J_0(a\rho) d\rho, a \ge 0. \tag{3.5}$$

Note for $\alpha = 2$ that this is the Rayleigh distribution. For α close to two it is essentially a Rayleigh distribution but with a heavier tail. From this point on, the $f_A(a)$ of (3.5) will be referred to as the α-stable envelope pdf.

The α-stable pdf does not exist in closed form except for $\alpha = 1$ or $\alpha = 2$, but it can be approximated numerically without a great deal of computational complexity.

In addition, the parameter γ is a simple scaling factor such that

$$f_X(x; \alpha, \gamma) = \frac{1}{\gamma^{\frac{1}{\alpha}}} f_X(\frac{x}{\gamma^{\frac{1}{\alpha}}}; \alpha, 1),$$

and likewise for the envelope pdf

$$f_A(a; \alpha, \gamma) = \frac{1}{\gamma^{\frac{1}{\alpha}}} f_A(\frac{a}{\gamma^{\frac{1}{\alpha}}}; \alpha, 1),$$

so a lookup table must vary only over the one parameter α. Such a lookup table method is used in these analyses.

The α-stable model is an empirical model, but like the Hall model it does have some physical justification. Nikias and Shao [37] show that under certain assumptions on the underlying noise sources and the propagation characteristics between them and the receiver, atmospheric noise is expected to exhibit an α-stable pdf. These assumptions, such as defining sources to be independently distributed in space and time, are not true in practice; however, they are approached closely enough in some cases to explain the accuracy of the α-stable model.

3.3 Determining APDs of the data

For data analysis, the underlying probability distribution $f_A(a)$ of the noise envelope must be derived from the data, so it is assumed that the desired ensemble statistics can be determined using corresponding time averages (for time intervals of interest). The data consist of one minute segments spaced one hour apart, however, and it is known that the noise is not stationary because the mean and RMS values have a diurnal and seasonal variation. To compensate for the shift in absolute amplitude levels between one minute segments, a normalization is performed on each segment such that the norm of A equals one, *i.e.*, $E[|A|] = E[A] = 1$.

A normalization in amplitude is used rather than the more common normalization in power, $E[A^2] = 1$, because of the large effect a few outliers (large impulsive values) can have on the second moment. When normalizing to the second moment,

just a few large sferics in one sample compared to another can shift the distributions with respect to each other even though their statistics are otherwise similar. When using normalization in amplitude, however, data taken over the course of hours and/or days have histograms that match closely.

Once all the one minute samples are normalized, they are combined into a histogram with 81 bins spaced logarithmically from 0.01 to 100, or -40 dB to 40 dB in power relative to $A = 1$. This dynamic range is found to include virtually every data point and is consistent with the range used for previously published data.

3.4 Data Analysis

This section presents the general results found when fitting all three models to all of the data, followed by specific results for each measurement location. This is followed by a discussion of each of the models, noting the range of parameters each model uses in fitting the data and how these parameters vary with season, time of day, and station. Finally, the results are compared with the voltage deviation parameter V_d.

Because of the difficulty of finding noise samples that are completely free of man-made interference and the extensive processing time required to manipulate even the uncontaminated data, only a small subset of the noise survey database is analyzed. Nonetheless, the resulting data set consists of 35 gigabytes and spans various times of the year and all times of the day at seven of the stations. Space limitations preclude the presentation of the thousands of graphs and model parameter values resulting from the analysis; instead the qualitative features of the data are discussed and some numerical results are provided as proof.

The data clearly reveal a pattern defining which model works best under which conditions, and the findings are as follows: the Hall model is found to be very accurate in modeling the amplitude pdf of VLF radio noise under the condition of heavy sferic activity in the noise, otherwise the α-stable model is optimal. In addition, there is a fairly large transition region (as a function of time, location, frequency, etc.) where both models are equally accurate. The F-L model exhibits an error metric roughly 10 to 100 times higher than the other two for most of the

data samples examined, but it is still reasonably accurate.

As mentioned in Chapter 1, heavy sferic activity means that the noise contains numerous sferic impulses, as in Figure 1.3. This condition is met in general at the low-latitude sites compared to the high-latitude sites, as seen in the differences between the time-series data from Grafton, Dunedin, Stanford, Kochi and L'Aquila and the data from Arrival Heights, Søndrestrøm and Thule. The higher latitude sites are far from the main sources of sferics (the tropical regions) so only larger sferics reach these locations. As viewed from a high-latitude receiver, then, sferics appear to be more sporadic.

It is stated in Section 2.2 that sferic activity at a given location has both a seasonal and a diurnal cycle. Seasonal variations peak during the local summer, and diurnal variations peak in the local afternoon. Since the optimal model depends on sferic activity, it is thus related to season and time of day.

The sferics themselves have a frequency response (as seen at the receiver) that peaks in the 8 – 14 kHz range and decreases with increasing frequency; therefore, only the stronger sferics create large impulses at the higher VLF frequencies (as seen in spectrograms similar to Figures 1.2 and 1.3). Because of this frequency response, narrowband time-series data appear to contain lower sferic activity as the center frequency is increased.

The bandwidth of the receiver is known to affect the impulsiveness of the noise because a narrow bandwidth spreads the sferics in time, causing them to overlap more and appear less impulsive (this typically lowers the V_d as well). Thus the α-stable model exhibits a larger error than the Hall at low bandwidths since the impulses are less distinctive against the background noise, but this is true only for very small bandwidths.

The following section presents specific results related to the above discussion, but it must be noted again that the analysis is known only to apply to atmospheric noise. Since auroral hiss has the characteristics of thermal noise, it is likely that the α-stable distribution with $\alpha \approx 2$ would model it accurately, but this hypothesis is not confirmed.

3.4.1 Results by Station

The Arrival Heights VLF data are taken from the time period May 1995 through June 1996; the center frequencies analyzed span the range 17 – 27.5 kHz and the noise bandwidth is chosen to be 600 Hz (in order to reject adjacent man-made signals). A fairly wide uncontaminated band from 25.5 – 27.5 kHz is analyzed as well. It is found that the α-stable model performs optimally over the whole data set, with an average MSLE of 0.0008, compared to 0.006 for the Hall and 0.0153 for the F-L. This means that on average the α-stable model is roughly within 7% ($10^{\sqrt{0.0008}}$) of the true pdf, compared to 19% for the Hall and 33% for the F-L. The α-stable model's accuracy is especially good above 20 kHz, where the respective average errors are 5%, 22% and 29%.

The Dunedin VLF data cover the year 1989; the center frequencies analyzed span the range 15 – 27 kHz and the noise bandwidth is 400 Hz. The band 25 – 27 kHz is analyzed as well. It is found that the Hall model performs best below approximately 23 kHz; above this range the α-stable model is slightly better. The respective percentage errors for the α-stable, Hall and F-L pdf's are 14%, 10% and 33% for frequencies below 23 kHz, and 8%, 10% and 31% for those above.

The Thule data include June 1986 to February 1987, with center frequencies ranging from 15 – 43 kHz (LF data were collected at Thule). The bandwidth for 23 kHz and below is 400 Hz; at the higher frequencies tested it is 2 kHz. It is found that the Hall and α-stable models are comparable below 23 kHz except during the peak of the seasonal and diurnal cycles, when the Hall model exhibits 1/2 to 1/3 the MSLE of the α-stable model. The respective average percentage errors for the α-stable, Hall and F-L models below 22 kHz are 12%, 10% and 34%; at higher frequencies those errors are 6%, 15% and 35%. Even at higher frequencies the seasonal and diurnal variations have an effect: at 36 kHz the α-stable error varies roughly from 5% to 11% seasonally and from 9% to 15% diurnally (during the seasonal peak).

The Søndrestrøm data include September 1993 to June 1994, with frequencies from 17 – 26 kHz and bandwidths of 600 Hz. The accuracy of the models follows the same diurnal, seasonal and frequency patterns as at the stations discussed above; sample results for Søndrestrøm are shown in Figure 3.2. The three rows of this
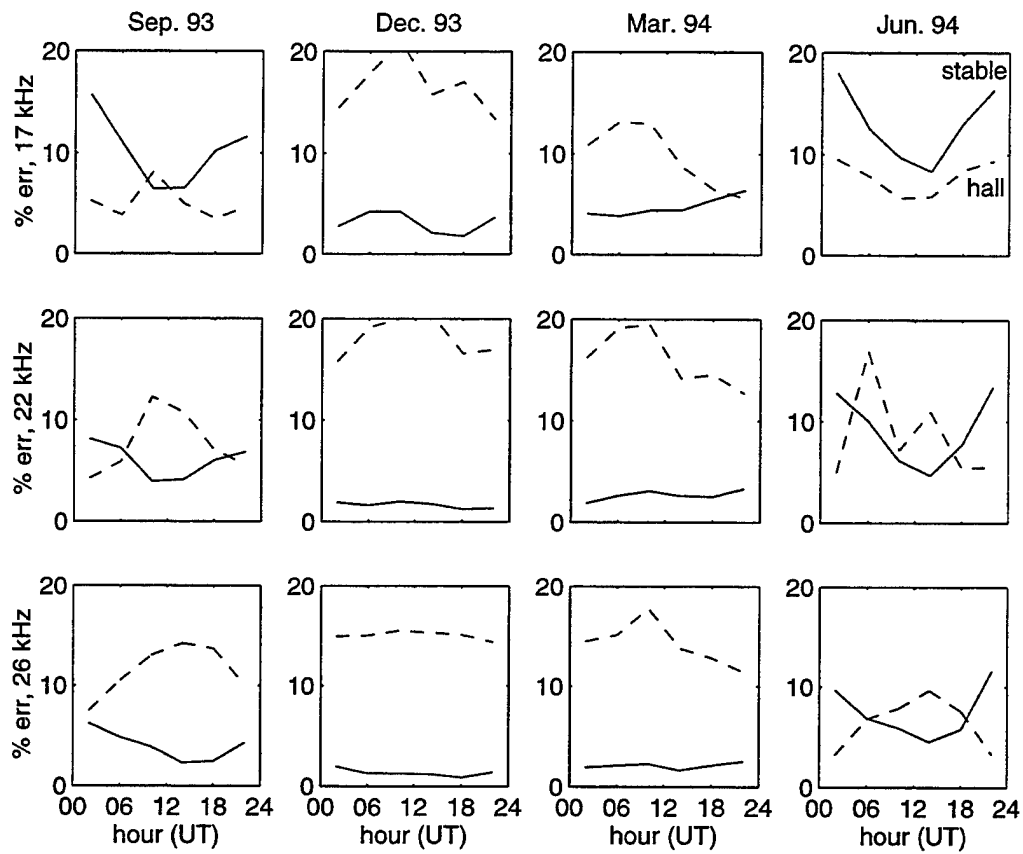
Figure 3.2: Errors of the Hall (dashed line) and α-stable (solid line) models as a function of frequency and season at Søndrestrøm.

figure correspond to center frequencies of 17.350, 22.550 and 26.500 kHz, and the four columns cover four consecutive seasons from September 1993 to June 1994. The plots are of the average percentage error as calculated using $10^{\sqrt{MSLE}}$; the Hall error is depicted by the dashed line and the α-stable error by the solid one.

Note that the α-stable model has considerably less error than the Hall for the months of December and March, when the northern hemisphere seasonal variation is at a minimum. However, in June and September (near the peak of storm season) and at 17 kHz, the Hall model gives better performance. In addition, there is a diurnal variation of the α-stable error in September and June, when it increases with the passing of North American storms at approximately 00 UT.

The Grafton, Stanford and L'Aquila data cover the same general frequency and time ranges as the data presented above, with the same results. Grafton is especially close to heavy storm activity in North America, which typically occurs in the northern hemisphere summer, so the accuracy of the α-stable model is noticeably worse during these months. This is depicted in Figure 3.3, which shows the average percentage errors (averaged over all frequencies) of the three models as a function of time of day for the months of January 1988 and July 1988. The α-stable model is clearly the best in January, but in July its performance degrades to a greater error than the Hall model.

Bandwidth Effects   Thule data at center frequencies of 36.6 kHz and 43.4 kHz and with bandwidths of 25, 50, 100, 200, 400, 800 and 1600 Hz were processed in order to test the effect of increasing bandwidth. The Hall model exhibits a larger MSLE and the α-stable model a smaller one as bandwidth increases, but the effect is only seen during increased storm activity, and the maximum error of either model is only approximately 13%.

An additional sample of Arrival Heights May 1995 data was processed with a center frequency of 8 kHz and bandwidth varying from 25 Hz to 1600 Hz. In this case the α-stable model is only 7.5 percent in error across the whole range of bandwidths, while the Hall error increases from 9.5 to 21 percent with increasing bandwidth. The F-L error varies between 40 and 60 percent.
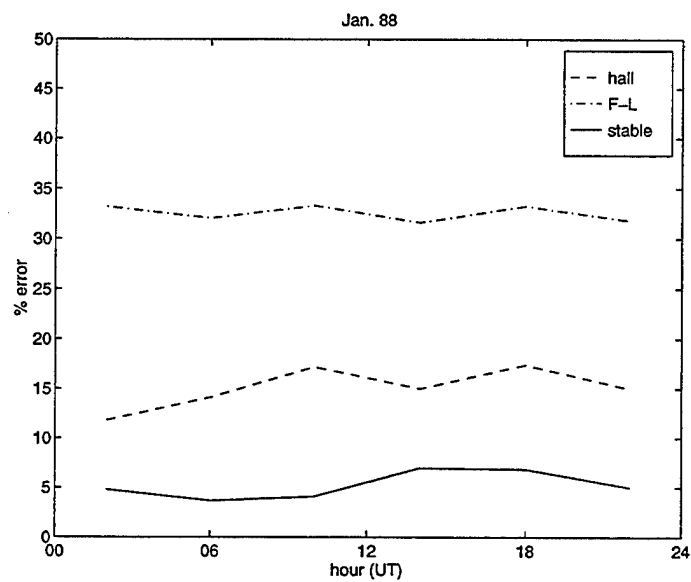
(a) January 1988
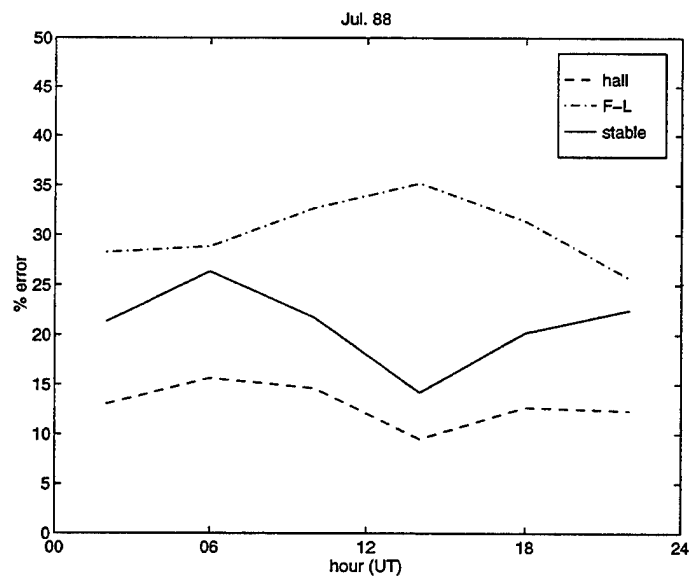
(b) July 1988

Figure 3.3: Errors of the Hall, Field-Lewinstein and α-stable models as a function of frequency and season at Grafton, New Hampshire.

Model	Parameters	MSdBE	% error
Hall	$m = 5.23$ $\gamma = 1.348$	0.0075	22%
F-L	$\alpha = 0.58$ $r_0 = 0.77$ $r = 0.18$	0.0132	30%
α-stable	$\alpha = 1.844$ $\gamma = 0.293$	0.000038	1.4%

Table 3.1: Parameter values for the Hall, Field-Lewinstein and α-stable models in Figure 3.4.

Model	Parameters	MSdBE	% error
Hall	$m = 3.05$ $\gamma = 0.665$	0.000088	2.2%
F-L	$\alpha = 0.59$ $r_0 = 0.40$ $r = 0.40$	0.0219	41%
α-stable	$\alpha = 1.38$ $\gamma = 0.276$	0.0011	8%

Table 3.2: Parameter values for the Hall, Field-Lewinstein and α-stable models in Figure 3.5.

3.4.2 Parameters of the Models

This section discusses how well each model fits various portions of the dynamic range of the noise envelope. This information is not contained in the MSLE since it is an average over the entire dynamic range; therefore, this section provides additional insight as to why a model may perform well or poorly. In addition, it is stated for each model the range of parameters exhibited in fitting the data histograms, and whether or not these parameters are correlated with location, center frequency, bandwidth, time of day or season of the year.

Figure 3.4 shows the fit of the three models (both APD and pdf) using a typical data sample for which the α-stable model is optimal; the data and α-stable plots virtually coincide. The data are from Arrival Heights during the 04 – 08 UT diurnal time period in May, a time and month of relatively low sferic activity. The center
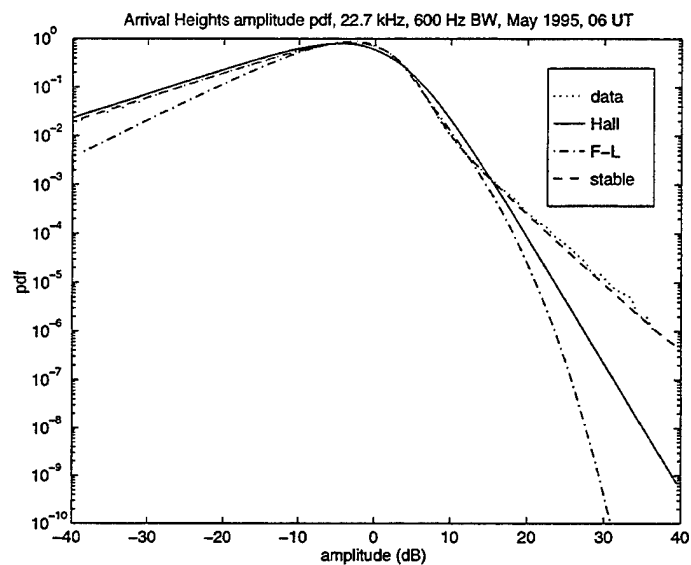
(a) fit of pdf
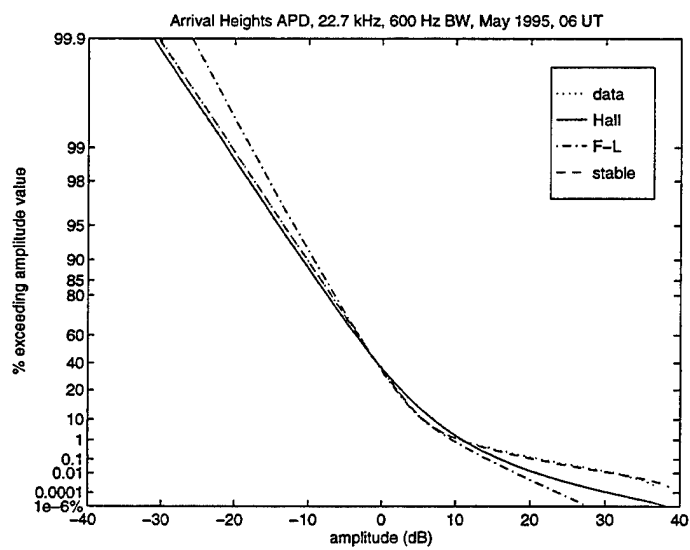
(b) fit of APD

Figure 3.4: Fit of the Hall, Field-Lewinstein and α-stable pdf models to a sample of Arrival Heights data.
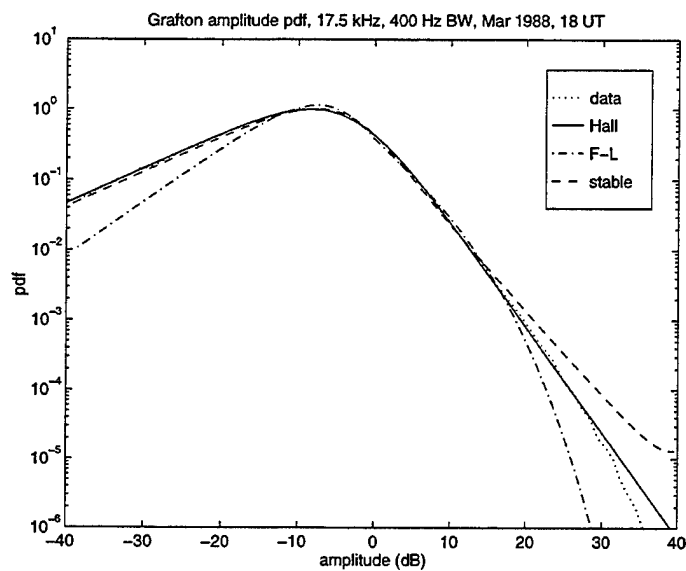
(a) fit of pdf
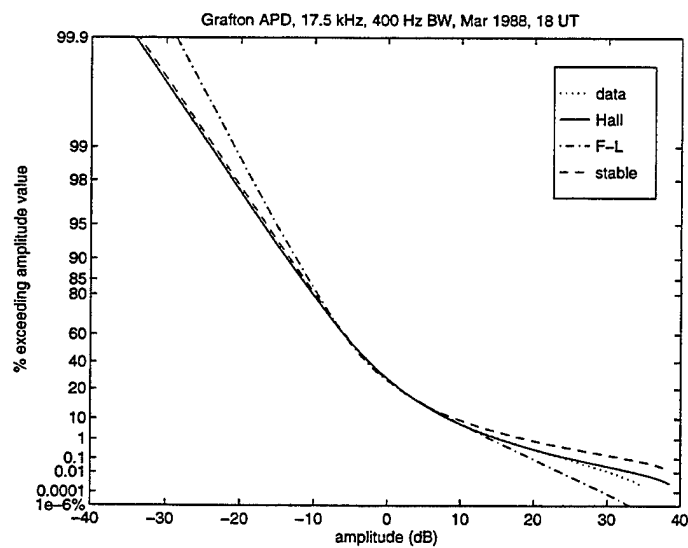
(b) fit of APD

Figure 3.5: Fit of the Hall, Field-Lewinstein and α-stable pdf models to a sample of Grafton data.

frequency is 22.7 kHz and the bandwidth is 600 Hz. Parameters and errors for the three models are given in Table 3.1.

The envelope pdf of Figure 3.4 is essentially Rayleigh except for a heavy tail due to occasional sferics, starting at 10 dB in the dynamic range. The Hall and F-L models fit the curve accurately in the high probability -10 to 10 dB range, but are unable to accurately model the higher range. In fact, they are often off by orders of magnitude.

Figure 3.5 shows the fit (both APD and pdf) for data typical of when the Hall model is optimal. The data are from Grafton, in March, and contain heavy sferic activity. The center frequency is 17.5 kHz and the bandwidth is 400 Hz. Parameters and errors for the three models are given in Table 3.2.

The value of m for the Hall model and the value of α for the α-stable model are significantly less in Table 3.2 than in Table 3.1. The average amplitude is higher relative to the background noise, and so more of the probability occurs at dB values less than zero. In addition, the data curve has no convex bend at 10 dB as in Figure 3.4, making the Hall pdf an almost perfect fit. The upward curve of the α-stable pdf near 40 dB in Figure 3.5 is due to limits of numerical accuracy for the algorithm used to determine the pdf.

3.4.3   Error Across Dynamic Range

The errors across dynamic range in Figures 3.4 and 3.5 are shown in Figure 3.6. A value of one on the y-axis corresponds to an order of magnitude in error, so it is seen that the Hall and F-L models give an estimate that is several orders of magnitude too low for the high end of the dynamic range in the Arrival Heights data. The F-L model gives too low an estimate at low levels as well.

For very small a, the F-L model has functional form $a^{\alpha+1}$, since it is the convolution of a with $a^{\alpha-1}$ (ignoring constants). This is clearly seen in Figures 3.4(a) and 3.5(a), where the slope of the F-L curves at low values is roughly 0.8 dB/dB. Since the abscissa is in dB power, this is equivalent to 1.6 dB/dB in amplitude, which is almost exactly the value of $1 + \alpha$. The other curves (including the data) have a slope
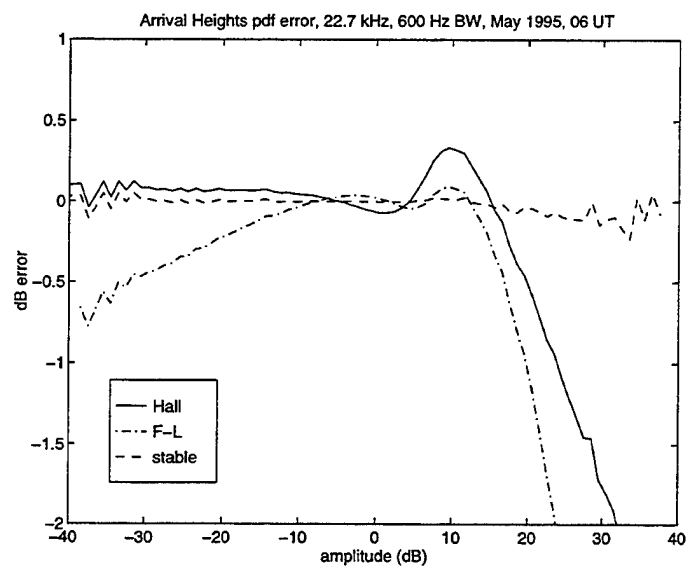
(a) error in Arrival Heights pdf fit
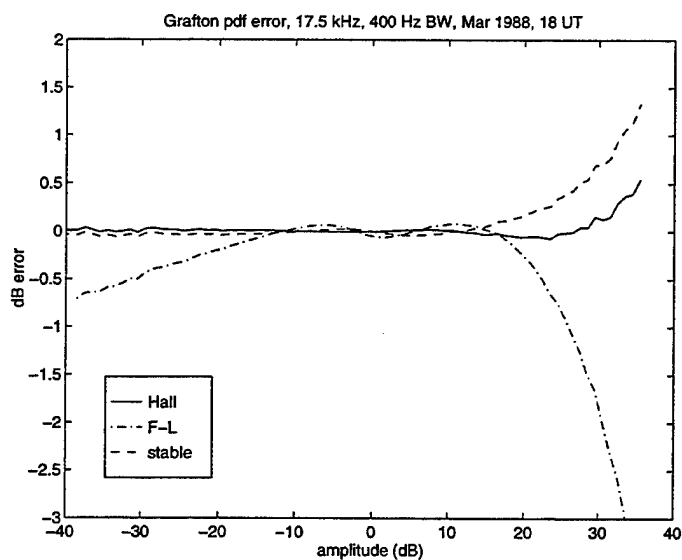
(b) error in Grafton pdf fit

Figure 3.6: Errors of the Hall, Field-Lewinstein and α-stable pdf models in fitting the data of Figures 3.4 and 3.5.

of 0.5 dB/dB power, or 1.0 dB/dB amplitude, indicating a Rayleigh pdf for small a. At the high end of the dynamic range, the F-L model decreases power-exponentially as $a \rightarrow \infty$, which is too rapid of a decay. The polynomial decay exhibited by the other two models is more accurate.

3.4.4 Typical Parameter Values

Typical values of the F-L parameters are as follows: α is usually in the range 0.5 to 0.6, although values as low as 0.34 and as high as 1.15 are found. The values of r_0 and r both range from 0.1 to 1.0, but typically take values of 0.7 and 0.25, respectively. There is only a mild dependence of the three parameters on season and time of day at the high-latitude sites, but at lower latitudes there is a large dependence. At Grafton, for example, the value of α jumps from 0.5 in January to 0.9 in June, and there is an additional 0.2 diurnal variation about these values as well. The term r_0 correspondingly drops from 0.8 to 0.2, and r increases from 0.2 to 0.8, from January to June.

The Hall model has values of m that range from 2.2 to 11, with typical values between 3 and 4. Values of γ range from 0.6 to 2.4 and are typically 1 to 1.5. There is no strong relationship between the Hall parameters and time, location, etc., but the values of m and γ do tend to rise as the center frequency is increased throughout the 15 – 27 kHz range.

The α-stable model has values of γ that are mostly near 0.3. The value of α is usually between 1.6 and 2.0, but can be as low as 1.1. A seasonal and diurnal dependence is seen in α, but it is strong only at the low-latitude sites.

3.4.5 ELF Results

The ELF data are severely contaminated by power line harmonics spaced either 50 Hz or 60 Hz apart, and the need for total rejection of these signals allows only for very narrow analysis bandwidths. (The need for total rejection of power line harmonics is demonstrated by the fact that even small leakage causes a significant drop in V_d). Fortunately, several data samples were found for which the 240 Hz

harmonic did not exist at all for an entire month, so the usable bandwidth spanned the range 180 – 300 Hz. These data samples are Arrival Heights for September 1994, and Thule and Søndrestrøm for April 1990. They are analyzed using a center frequency of 240 Hz and bandwidths ranging over the values 5, 10, 15, 20, 25 and 30 Hz.

The ELF results do not differ significantly from the VLF results either qualitatively or quantitatively. The average percentage errors of the α-stable, Hall and F-L models at Arrival Heights are 4%, 12% and 36%, respectively; at Søndrestrøm they are 9%, 6% and 42% respectively; at Thule they are 8%, 7% and 37%. These numbers are averaged across bandwidth; at the larger bandwidths the α-stable model always outperforms the Hall. The parameter ranges of the models are the same as described above for VLF.

3.5 Voltage Deviation

The V_d statistic is reintroduced at this point because it is a fundamental concept in previous work on modeling atmospheric noise [26, 42]. It is computed as $V_d = 10\log(E[A^2]/E^2[A])$, and as such it is the RMS value of the noise envelope divided by the average value, in dB. V_d is a measure of the *spikiness* of the noise (since sharper impulses result in a higher RMS value relative to the mean value) and is greatly dependent on the noise bandwidth; however, it is not necessarily an indicator of heavy sferic activity. For the data of Figure 3.4, the V_d is 3.48 dB, and for the data of Figure 3.5, it is 4.91 dB, but there are many cases where the α-stable model is optimal for higher V_d's as well. (It should be noted that the ability to compute $10\log(E[A^2]/E^2[A])$ from the data is based on system dynamic range limitations, since V_d is undefined for many parameter values of the Hall and α-stable models).

Seasonal and diurnal variations of V_d are seen in the data, but they cannot be systematically correlated with known storm distributions. For instance, V_d does not necessarily rise and fall with storm season: at Grafton (for one sample frequency band) it reaches a low of 2.5 dB in both January and July, from approximately 4.5 dB in spring and fall. Other data show that Grafton's V_d varies out of phase with its

diurnal variation, while Dunedin's V_d variation is in phase with its diurnal variation. The typical range of V_d values is 1.5 dB to 6.0 dB, although values as high as 10 dB can be seen at high-latitude sites.

V_d is also found to relate somewhat to the parameters of the three pdf models. For one set of Arrival Heights data samples, the Hall parameters m and γ decrease from 10 to 2.8 and 2.0 to 0.4, respectively, as V_d increases from 1.5 to 9.0. The F-L parameters α, r_0 and r change from 0.7 to 0.4, 1.0 to 0.4, and 0.1 to 0.2, respectively, as V_d increases, and the α-stable parameters α and γ decrease from ≈ 2.0 to 1.2 and 0.3 to 0.2, respectively. The errors of the three models have fairly little relation to V_d, except that the Hall model tends to be more accurate than the α-stable model for lower values of m, which corresponds to higher values of V_d. This is not universally true, though, since as mentioned previously it is possible to have a high V_d for noise of relatively low sferic activity.

3.6 Conclusions

This chapter presents many APD results derived from a statistical analysis of low-frequency radio noise. Three models for the noise envelope APD are described, and the parameters and accuracy of each model are determined as a function of location, time and frequency. The parameters and errors of each model are found to vary with thunderstorm activity, and the noise frequency and bandwidth.

The main conclusion of this chapter is that the Hall model is the optimal model in terms of accuracy and simplicity for locations exposed to heavy sferic activity, and the α-stable model is best for locations relatively distant from heavy sferic activity. A general rule based on the results would be to use the α-stable pdf in high-latitude regions except at the peak of the diurnal and seasonal storm cycle, and to use the Hall model at low- and mid-latitudes except at the null of the seasonal and diurnal cycle. The crossover point is not critical; there are a broad range of conditions where both models have roughly the same accuracy.

Chapter 4

Clustering Poisson Model

4.1 Introduction

This chapter presents a statistical-physical radio noise model, denoted the "clustering Poisson" model, and shows that this model predicts several important statistical features of atmospheric radio noise very accurately. The model is derived in conjunction with the statistical results of Chapters 2 and 3, and so it is supported by a multitude of real data. The term "clustering Poisson" is used to describe the model because noise source events occur as Poisson processes that are triggered by another, independent Poisson process, and thus the noise impulses are seen to occur in bursts, or clusters.

A number of statistical-physical noise models (*i.e.*, based on the underlying physical process that creates the noise) have been developed over the past four decades; each can be roughly categorized into one of two types: (i) simple enough to provide concise, closed form answers but only somewhat representative of the true physical situation, and (ii) representative of the true physical situation but very complicated to use. The second type often uses specific storm distribution and propagation information and calculates the noise characteristics at a given point numerically (*e.g.*, Warber and Field [46]), whereas the first type usually assumes independence in space and time of the source distribution (a condition known not to be true in practice). The new model partially bridges the gap between the two

types by replacing independence in time with a clustering Poisson assumption.

The model is verified by comparing it to four statistical features of atmospheric radio noise: impulse interarrival distributions, correlations between impulses, APDs, and power spectral densities. The impulse interarrival time distributions predicted by the model are shown to match those seen in the data, thus verifying the accuracy of the clustering Poisson assumption. Furthermore, the noise amplitude probability density function predicted by the clustering Poisson model, the α-stable envelope pdf, is shown in Chapter 3 to accurately fit histograms of real data for locations relatively distant from storm activity. Finally, clustering of pulses is shown to have little effect on the power spectral density of the noise, a fact also seen in the data. Given the accuracy to which the predicted statistical features fit the actual data, it is concluded that the clustering Poisson model is a good candidate as a model for atmospheric noise.

Section 4.2 discusses several existing models for atmospheric noise and presents the new clustering Poisson model, then Section 4.3 shows that this model predicts the noise envelope pdf to be an α-stable distribution. Section 4.4 derives the predicted impulse interarrival distributions, and Section 4.5 discusses power spectral densities. Finally, the results are summarized in Section 4.6.

4.2   Review of Existing Models

Most impulsive noise models do not take impulse interarrival time dependencies into account, but two statistical-physical models that do address impulse clustering are those of Furutsu and Ishida [16] and Giordano and Haber [18]. Furutsu and Ishida address only the clustering of pilots and leaders (on the order of milliseconds) in an individual lightning stroke, however, and the analysis does not provide concise results. Giordano and Haber model impulse clustering by assuming that with each *independent* impulse there is a finite probability of a similar *dependent* impulse a time τ_i later, where τ_i is an appropriately specified random variable. The analysis is not extended to multiple dependent impulses due to the added mathematical complexity. Both models provide several key features upon which the new model is based, such

as specification of the source distribution and propagation characteristics.

Nikias and Shao [37] use an adapted form of Giordano's model (without impulse clustering), in addition to a method in Zolotarev [48] for the model of point sources of influence, to prove that atmospheric noise has an α-stable distribution. Since some of the results in the following sections use this proof, the notation in describing both the non-clustering model and the new clustering model largely follows that in [37].

4.2.1 A Non-Clustering Statistical-Physical Poisson Model

This section defines a non-clustering statistical-physical Poisson model that is common in principle to several described in the literature [18]. Begin by assuming that the received noise is the superposition of many impulses produced by many sources in a region encompassing the receiver location. Given this assumption, if the exact source distribution were known, as well as the exact time that each source emits an impulse and the exact waveform of each impulse at the receiver (including knowledge of time delay), the characteristics of the received noise waveform could be completely determined. The problem, of course, is that it could only be determined numerically and would not in general yield simple, closed form results. In order to proceed to such results, exact knowledge of the source characteristics must be replaced with simplified statistical approximations and expectations.

The region Ω encompassing the receiver location is defined on $\mathbf{R^n}$, where $n \in \{1, 2, 3\}$ is the dimension of the space (*i.e.*, a line ($\mathbf{R^1}$), a plane ($\mathbf{R^2}$), or a volume ($\mathbf{R^3}$)). The receiver is at the origin and each source i is at a position $\mathbf{x}_i$ a distance $|\mathbf{x}_i|$ from the receiver. It is assumed that all sources have similar enough waveform generation mechanisms that their emitted waveforms may be modeled as $a_i D(t; \theta_i)$, where the random amplitudes a_i are independent and identically distributed (i.i.d.) with pdf $f_a(a)$ (denoted i.i.d. $\sim f_a(a)$) and the random parameters θ_i are i.i.d. $\sim f_\Theta(\theta)$. The θ_i represent arbitrary mappings from a probability space to an ensemble of possible waveforms; they are chosen to be scalars for simplicity.

The effect of the transmission medium is modeled as the combination of a power law attenuation factor ν and a linear, time-invariant (LTI) filtering factor $h(\theta)$ such

that the impulse $a_i D(t; \theta_i)$ appears as $a_i \frac{c_1}{|\mathbf{x}_i|^\nu} D(t; \theta_i) * h(\theta_i)$ at the receiver, where c_1 is a positive constant and $\nu > 0$. Since θ_i is arbitrary, the convolution $D(t; \theta_i) * h(\theta_i)$ may be defined as $E(t; \theta_i)$ without loss of generality. Further defining the quantity

$$U(t; \mathbf{x}_i, \theta_i) = \frac{c_1}{|\mathbf{x}_i|^\nu} E(t; \theta_i) \tag{4.1}$$

and letting the random variable N be the number of contributing impulses at the time of observation, the received waveform Y is then

$$Y = \sum_{i=1}^{N} a_i U(t_i; \mathbf{x}_i, \theta_i). \tag{4.2}$$

The time $t_i > 0$ is defined as the difference between the observation time $t = 0$ and the source emission time, so it is larger for *older* impulses (*i.e.*, t is a measure of negative time).

It now remains to specify N. In order to attain the most tractable results while maintaining a reasonably accurate physical representation, N is assumed to be the number of events generated by a Poisson process in space and time with source density function $\rho(\mathbf{x}, t)$. The value $\rho(\mathbf{x}, t) \, d\mathbf{x} \, dt$ is then the probability that a noise impulse will be emitted from the (infinitely small) region defined by the line, square or cube (for $n = 1, 2, 3$) with far corners $\mathbf{x}$ and $\mathbf{x} + d\mathbf{x}$, and during the (infinitely small) interval $[t, t + dt]$ prior to observation. The term $\rho(\mathbf{x}, t)$ may take a general form over $\mathbf{x} \in \Omega$ and $t \in [0, \infty)$, but for simplicity it is approximated as

$$\rho(\mathbf{x}, t) \approx \frac{\rho_0}{|\mathbf{x}|^\mu} \tag{4.3}$$

where $\rho_0, \mu > 0$ are constants. Thus the sources are defined to be independent both in time and direction from the receiver. The exponent μ defines a variation in source density with distance, providing an added degree of freedom with minimal added complexity.

The definition of $\rho(\mathbf{x}, t)$ in Eq. (4.3) is the key approximation for making further analyses reasonably simple and tractable, but it is not the true physical source

distribution of atmospheric radio noise. Various storm centers are active at various times of day and year [4, 5, 19], so for a given receiver location there are certain directions from which heavier sferic activity arrives than others. This directional dependence contradicts the source distribution of Eq. (4.3), but nonetheless Eq. (4.3) is often reasonably accurate.

The temporal independence approximation, however, is not reasonably accurate. Bursts of sferics on the order of one second in length are clearly seen in spectrograms of ELF/VLF/LF time-series data at all locations and times (see Figure 1.2), and they have considerable effect on the time-series data. The model presented below adds impulse clustering properties to the model just described in a way that accurately represents this clustering of sferics.

4.2.2 Definition of the Clustering Poisson Model

Instead of specifying the received waveform Y to be the superposition of impulses distributed throughout the region, specify it to be the superposition of clusters distributed throughout the region, where a cluster is defined as a burst of impulses from a given location over a short time period. (Clusters will be specified in detail in the next two sections). The resulting waveform at the receiver is then

$$Y = \sum_{k=1}^{N_c} X_k = \sum_{k=1}^{N_c} \sum_{i=0}^{N_k} a_{k,i} U(\tau_{k,i}; \mathbf{x}_k, \theta_{k,i}), \qquad (4.4)$$

where N_c is the number of clusters, N_k is the number of impulses in cluster k, and the indices k, i on a, τ and θ refer to the ith impulse of the kth cluster ($i = 0$ refers to the impulse that starts the cluster). All the impulses in cluster k are modeled as occurring at the same location $\mathbf{x}_k$. The $a_{k,i}$ and $\theta_{k,i}$ are all independent, an assumption verified by the lack of correlations between impulses discussed in Section 2.5. Every cluster is assumed to be independent of every other in both space and time. The X_k's are the waveforms of the individual clusters.

4.2.3 Specification of Clusters

The number of clusters N_c is analogous to N in Eq. (4.2) and the clusters have the source density of Eq. (4.3), but the statistical properties of the clusters themselves still need to be specified. The specification chosen must accurately model the physical mechanism of lightning and should also lead to tractable results.

In order to develop a physically accurate model, several features of lightning must be considered. From Uman's classic text *Lightning* [44], it is known that a complete cloud to ground discharge, called a *flash*, is made up of one or more intermittent, partial discharges, called *strokes*. Each stroke involves a complex process whereby either a *stepped leader* or a *dart leader* initiates a strong *return stroke*, transferring large amounts of charge between the earth and its atmosphere. A significant percentage of flashes contain many strokes; one data sample in [44] indicates that 40 percent of all flashes contain at least five strokes and some contain as many as 19. In addition, 50 percent of those flashes with five or more strokes have a duration of more than 400 milliseconds. Data histograms in [44] and [46] showing typical flash per stroke distributions indicate that the number of flashes per stroke can be reasonably modeled as a geometric random variable; thus the number of impulses per cluster in the clustering Poisson model is defined to be a geometric random variable as well.

Now the timing of impulses within a cluster must be specified. Every cluster has at least one impulse, which is the start of the cluster. The interarrival times T_i between any additional impulses in a given cluster are specified as i.i.d. random variables with pdf

$$f_T(t) = \lambda_1 e^{-\lambda_1 t}, \; t \geq 0, \tag{4.5}$$

i.e., an exponential distribution (denoted $EXP(\lambda_1)$). Each cluster then is essentially a variable length Poisson process with rate λ_1 impulses per second, and as stated above, all the clusters are independent of the main process and of each other. Similar cluster specifications have found use in modeling computer failures [29], earthquakes [45], and neural impulses [21].

4.2.4   Length of Clusters

This section specifies the probability mass function (pmf) of the N_k's and determines the pdf of the cluster lengths T_{Lk}. The N_k's are modeled as i.i.d. geometric random variables with pmf

$$P(N = n) = \frac{\lambda_L}{\lambda_1 + \lambda_L} \left(\frac{\lambda_1}{\lambda_1 + \lambda_L} \right)^n , \quad n = 0, 1, 2, 3 \ldots, \tag{4.6}$$

where the index k is omitted since this pdf applies for all k. The parameter λ_L is now shown to be the reciprocal of the expected cluster length.

If $N = 0$, there are no impulses after the first impulse and the cluster length is zero. For a given $N > 0$, the length T_L of the cluster is the sum of N independent $\mathrm{EXP}(\lambda_1)$ random variables, and therefore it is known to have the Erlang density

$$f_{T_L|N}(t, n) = \frac{\lambda_1 (\lambda_1 t)^{n-1} e^{-\lambda_1 t}}{(n-1)!}. \tag{4.7}$$

Thus the pdf $f_{T_L}(t)$ for $t > 0$ can be determined by conditioning on N:

$$
\begin{aligned}
f_{T_L}(t) &= \sum_{n=1}^{\infty} \frac{\lambda_L}{\lambda_1 + \lambda_L} \left(\frac{\lambda_1}{\lambda_1 + \lambda_L} \right)^n \frac{\lambda_1 (\lambda_1 t)^{n-1} e^{-\lambda_1 t}}{(n-1)!} \tag{4.8} \\[2mm]
&= \left(\frac{\lambda_L}{\lambda_1 + \lambda_L} \right) \left(\frac{\lambda_1}{\lambda_1 + \lambda_L} \right) \lambda_1 e^{-\lambda_1 t} \sum_{n=0}^{\infty} \frac{\left(\frac{\lambda_1^2 t}{\lambda_1 + \lambda_L} \right)^n}{n!} \tag{4.9} \\[2mm]
&= \left(\frac{\lambda_1}{\lambda_1 + \lambda_L} \right) \left(\frac{\lambda_1 \lambda_L}{\lambda_1 + \lambda_L} \right) e^{-\left(\frac{\lambda_1 \lambda_L}{\lambda_1 + \lambda_L} \right) t}, \quad t > 0, \tag{4.10}
\end{aligned}
$$

where (4.10) is obtained using the exponential summation formula. Note that the rest of the probability on T_L is at the point $P(T_L = 0) = \lambda_L / (\lambda_1 + \lambda_L)$.

Since $\lambda_1 / (\lambda_1 + \lambda_L)$ is the probability that $N > 0$, it is apparent from Eq. (4.10) that $f_{T_L|N>0}$ is $\mathrm{EXP}(\lambda_1 \lambda_L / (\lambda_1 + \lambda_L))$ distributed. In addition, since the expected value of an $\mathrm{EXP}(\lambda)$ random variable is $1/\lambda$, it follows from (4.10) that

$$E[T_L] = \frac{\left(\frac{\lambda_1}{\lambda_1 + \lambda_L} \right)}{\left(\frac{\lambda_1 \lambda_L}{\lambda_1 + \lambda_L} \right)} = \frac{1}{\lambda_L}. \tag{4.11}$$

An equivalent cluster specification results by defining clusters to be Poisson processes of random length $T_{\hat{L}}$, where $T_{\hat{L}}$ is EXP(λ_L). In other words, it is equivalent to define (i) the N_k's as geometric random variables, so that the cluster length T_L given N_k is Erlang distributed as in (4.7), or (ii) the length $T_{\hat{L}}$ of a rate λ_1 Poisson process such that $N_k|T_{\hat{L}}$ is a Poisson($\lambda_1 T_{\hat{L}}$) random variable. With definition (ii), the pmf of N_k is

$$
\begin{aligned}
P(N_k = n) &= \int_0^\infty \lambda_L e^{-\lambda_L t} \frac{(\lambda_1 t)^n e^{-\lambda_1 t}}{n!} \, dt & (4.12) \\
&= \frac{\lambda_L}{n!} \int_0^\infty (\lambda_1 t)^n e^{-(\lambda_1 + \lambda_L) t} \, dt & (4.13) \\
&= \frac{\lambda_L}{\lambda_1 + \lambda_L} \left(\frac{\lambda_1}{\lambda_1 + \lambda_L} \right)^n, \; n = 0, 1, 2, 3 \ldots, & (4.14)
\end{aligned}
$$

where the integral in (4.13) is solved using item (860.07) in Dwight [9]. Since (4.14) and (4.6) are identical and the interarrival specifications are the same as well, definitions (i) and (ii) are equivalent. The variable $T_{\hat{L}}$, however, is not the length of the cluster; it is simply the length of an underlying Poisson process. The variable T_L (which is less than or equal to $T_{\hat{L}}$) is the true length of the cluster, for it indicates the location of the last impulse. Definition (ii) is introduced because it simplifies the proof in the next section.

4.3 Probability Density Function of Clustered Poisson Noise

Now that the clustering Poisson model is specified, it remains to demonstrate its validity in the modeling of real data. This section presents a proof that the first order pdf of the received noise Y defined by the clustering model of Eq. (4.4) is an α-stable distribution.

Let the receiver's response due to a single cluster X_k starting at time t_k before

zero (zero is the observation time) and at location $\mathbf{x}_k$ be

$$X_k = a_{k,0}U(t_k; \mathbf{x}_k, \theta_{k,0}) + \sum_{i=1}^{N_k} a_{k,i}U(\tau_{k,i}; \mathbf{x}_k, \theta_{k,i}), \qquad (4.15)$$

where the first term of (4.15) is the impulse at t_k, the cluster starting time. Since the clusters are i.i.d., the index k is redundant when specifying any one cluster; thus the notation

$$X = a_0U(t; \mathbf{x}, \theta_0) + \sum_{i=1}^{N} a_iU(\tau_i; \mathbf{x}, \theta_i) \qquad (4.16)$$

is used from this point on, where $i = 0, \ldots, N$ remains the index for impulses within a cluster. (In Eqs. (4.15) and (4.16), the $i = 0$ term is separated out from the summation).

Now use the second cluster specification of Section 4.2.4, noting that the length $t_{\hat{L}}$ is an $\text{EXP}(\lambda_L)$ random variable. The impulse rate within clusters over this length is λ_1 impulses per second, so it follows that for a given $t_{\hat{L}}$, $N \sim \text{Poisson}(\lambda_1 t_{\hat{L}})$ and the τ_i's (for $i > 0$ and without respect to ordering) are i.i.d. uniformly distributed over $[t - t_{\hat{L}}, t]$. (Once again, time is in the negative direction). Defining $a_iU_i = a_iU(\tau_i; \mathbf{x}, \theta_i)$ as the contribution to the received waveform of any one of the impulses other than the first in a cluster X, it also follows that the characteristic function of the conditional pdf of a_iU_i given $\mathbf{x}$, t and $t_{\hat{L}}$, denoted $\Phi_i(\omega)|\mathbf{x}, t, t_{\hat{L}}$, is

$$\Phi_i(\omega)|\mathbf{x}, t, t_{\hat{L}} = E[e^{j\omega a_iU(\tau_i; \mathbf{x}, \theta_i)}] \qquad (4.17)$$

$$= \int_{-\infty}^{\infty} f_a(a)da \int_{\Theta} f_\theta(\theta)d\theta \int_{t-t_{\hat{L}}}^{t} \frac{1}{t_{\hat{L}}}d\tau \ e^{j\omega aU(\tau; \mathbf{x}, \theta)}, \qquad (4.18)$$

where the integrand in (4.18) is brought to the far right for reading clarity. (This format is used in several of the following equations as well). The impulsive waveform $U(\tau; \mathbf{x}, \theta)$ is specified without loss of generality to be zero for $\tau < 0$ in order that the system remains causal.

The characteristic function of X given $\mathbf{x}$ and t, including the $i = 0$ (first) impulse,

is then

$$
\begin{aligned}
\Phi_X(\omega)|\mathbf{x},t &= E[e^{j\omega a_0 U(t;\mathbf{x},\theta_0)}]E[(\Phi_i(\omega)|\mathbf{x},t,t_i)^n] \tag{4.19}\\
&= \left[\int_{-\infty}^{\infty} f_a(a)da \int_{\Theta} f_{\Theta}(\theta)d\theta \, e^{j\omega a U(t;\mathbf{x},\theta)}\right]\\
&\quad \cdot \int_0^{\infty} \lambda_L e^{-\lambda_L \tau} \sum_{n=0}^{\infty} \frac{(\lambda_1 \tau)^n e^{-\lambda_1 \tau}}{n!} (\Phi_i(\omega)|\mathbf{x},t,\tau)^n \, d\tau \tag{4.20}\\
&= \left[\int\!\!\int_a \int_{\Theta} e^{j\omega a U(t;\mathbf{x},\theta)}\right]\int_0^{\infty} \lambda_L e^{-\lambda_L \tau} e^{\lambda_1 \tau((\Phi_i(\omega)|\mathbf{x},t,\tau)-1)} \, d\tau \tag{4.21}\\
&= \left[\int\!\!\int_a \int_{\Theta} e^{j\omega a U(t;\mathbf{x},\theta)}\right]\\
&\quad \cdot \int_0^{\infty} \lambda_L e^{-\lambda_L \tau} e^{\lambda_1 \int_{-\infty}^{\infty} f_a(a)da \int_{\Theta} f_{\Theta}(\theta)d\theta \int_{t-\tau}^{t} d\tau' \left(e^{j\omega a U(\tau';\mathbf{x},\theta)}-1\right)} \, d\tau. \tag{4.22}
\end{aligned}
$$

Note that the -1 in the last exponent of (4.21) is brought inside the integrals over a, θ and τ' in (4.22) (the joint pdf will still integrate to the same result), and the notation of the bracketed term in (4.20) is simply abbreviated in (4.21) and (4.22).

In order to get the characteristic function of any cluster that is randomly distributed over a region $\mathbf{x} \in \Omega(R_1, R_2)$ (*i.e.*, the region for which $R_1 \le \mathbf{x} \le R_2$) and a starting time $t \in [0, T]$, expectations must be taken over $\mathbf{x}$ and t:

$$
\begin{aligned}
\Phi_X(\omega) &= \int_0^T \int_{\Omega} f_{T,R_1,R_2}(\mathbf{x},t)\left\{\left[\int\!\!\int_a \int_{\Theta} e^{j\omega a U(t;\mathbf{x},\theta)}\right]\right.\\
&\quad \left. \cdot \int_0^{\infty} \lambda_L e^{-\lambda_L \tau} \, e^{\left[\lambda_1 \int_a \int_{\Theta} \int_{t-\tau}^{t} d\tau' \left(e^{j\omega a U(\tau';\mathbf{x},\theta)}-1\right)\right]}\right] d\tau\right\} d\mathbf{x}\,dt, \tag{4.23}
\end{aligned}
$$

where again the integral expressions on a and Θ have been abbreviated.

Now define the superposition of all clusters within the region $\Omega(R_1, R_2)$ and starting in the time interval $[0, T]$ as

$$
Y_{T,R_1,R_2} = \sum_{k=1}^{N_c} X_k = \sum_{k=1}^{N_c} \sum_{i=0}^{N_k} a_{k,i} U(\tau_{k,i}; \mathbf{x}_k, \theta_{k,i}) \tag{4.24}
$$

as in Eq. (4.4). The number of clusters N_c is a Poisson random variable with

parameter

$$\lambda_{T,R_1,R_2} = \int_{\Omega(R_1,R_2)} \int_0^T \rho(\mathbf{x},t)\, dt\, d\mathbf{x} \qquad (4.25)$$

and the $(\mathbf{x}_k, t_k)$ terms (the locations and starting times of the clusters) are i.i.d. with distribution

$$f_{T,R_1,R_2} = \frac{\rho(\mathbf{x},t)}{\lambda_{T,R_1,R_2}}, \ \mathbf{x} \in \Omega(R_1,R_2), \ t \in [0,T]. \qquad (4.26)$$

Since cluster formation is a Poisson process, the characteristic function of Y_{T,R_1,R_2} can be calculated in the same manner as the second term on the right in (4.19) to get

$$\Phi_Y(\omega) = e^{\lambda_{T,R_1,R_2}(\Phi_X(\omega)-1)}. \qquad (4.27)$$

Inserting (4.26) into (4.23) and the result into (4.27), then taking logarithms, results in

$$\log \Phi_Y(\omega) = \int_0^T \int_\Omega \rho(\mathbf{x},t) \left\{ \left[\int_a \int_\Theta e^{j\omega a U(t;\mathbf{x},\theta)} \right] \left[\int_0^\infty \lambda_L e^{-\lambda_L \tau} \right. \right.$$
$$\left. \left. \cdot\, e^{\left[\lambda_1 \int_a \int_\Theta \int_{t-\tau}^t d\tau' \left(e^{j\omega a U(\tau';\mathbf{x},\theta)}-1 \right) \right]} d\tau \right] - 1 \right\} d\mathbf{x}\, dt, \qquad (4.28)$$

where the last -1 is brought inside the integrals over $\mathbf{x}$ and t without changing the result. Inserting (4.1) and (4.3), noting that $f_a(a)$ is a symmetric distribution, and using the identity $\cos 2x = 1 - 2\sin^2(x)$ results in

$$\log \Phi_Y(\omega) = \int_0^T \int_\Omega \frac{\rho_0}{|\mathbf{x}|^\mu} \left\{ \left[2 \int_{a=0}^\infty \int_\Theta \cos(\omega a c_1 |\mathbf{x}|^{-\nu} E(t;\theta)) \right] \left[\int_0^\infty \lambda_L e^{-\lambda_L \tau} \right. \right.$$
$$\left. \left. \cdot\, e^{\left[-4\lambda_1 \int_{a=0}^\infty \int_\Theta \int_{t-\tau}^t d\tau' \left(\sin^2(\frac{1}{2}\omega a c_1 |\mathbf{x}|^{-\nu} E(\tau';\theta)) \right) \right]} d\tau \right] - 1 \right\} d\mathbf{x}\, dt. $$
$$(4.29)$$

At this point the last exponential in (4.29) must be converted to a Taylor series,

resulting in

$$\log \Phi_Y(\omega) = \int_0^T \int_\Omega \frac{\rho_0}{|\mathbf{x}|^\mu} \left\{ \left[2 \int_{a=0}^\infty \int_\Theta \cos(\omega a c_1 |\mathbf{x}|^{-\nu} E(t;\theta)) \right] \left[\int_0^\infty \lambda_L e^{-\lambda_L \tau} \right. \right.$$
$$\left. \cdot \left(\sum_{j=0}^\infty \frac{(-4\lambda_1)^j}{j!} \left[\int_{a=0}^\infty \int_\Theta \int_{t-\tau}^t d\tau' \left(\sin^2(\frac{1}{2}\omega a c_1 |\mathbf{x}|^{-\nu} E(\tau';\theta)) \right) \right]^j \right) d\tau \right]$$
$$\left. -1 \right\} d\mathbf{x}\, dt. \tag{4.30}$$

In order to proceed further, solve for only the $j = 0$ term and group the last -1 with this term as well. Since the integral over τ is one in this case, the $j = 0$ term of Φ_Y is

$$\Phi_{Y,j=0}(\omega) = e^{\int_0^T \int_\Omega \frac{\rho_0}{|\mathbf{x}|^\mu} \left[-4 \int_{a=0}^\infty \int_\Theta \sin^2(\frac{1}{2}\omega a c_1 |\mathbf{x}|^{-\nu} E(t;\theta)) \right] d\mathbf{x}\, dt}. \tag{4.31}$$

Now integrate over $\mathbf{x}$ first, and consider the substitution $r = |\mathbf{x}|$. If $n = 1$, the integral is over dr; if $n = 2$, switching to polar coordinates results in an integral over $2\pi r\, dr$; if $n = 3$, spherical coordinates give an integration over $4\pi r^2\, dr$. For general dimension n, the integral is over $c_n r^{n-1}\, dr$. Using this conversion and an additional substitution $r' = r^{-\nu}$, $dr' = -\nu r^{-\nu-1} dr$ (and then dropping the primes) results in

$$\Phi_{Y,j=0} = e^{-\frac{4c_n \rho_0}{\nu} \left[\int_0^T \int_{a=0}^\infty \int_\Theta \int_{r=R_1}^{R_2} \sin^2(\frac{1}{2}\omega a c_1 r E(t;\theta))(r^{-\frac{n-\mu}{\nu}-1})\, dr\, d\theta\, da\, dt \right]}. \tag{4.32}$$

Now set $R_1 \to 0$, $R_2 \to \infty$ and $T \to \infty$, define $\alpha = \frac{n-\mu}{\nu}$, where $0 < \alpha \le 2$, and use the definite integral (3.823) from Gradshteyn and Rhyzik [20],

$$\int_0^\infty x^{\mu-1} \sin^2 ax\, dx = -\frac{\Gamma(\mu) \cos \frac{\mu\pi}{2}}{2^{\mu+1} a^\mu}, \quad a > 0, \ -2 < \mu < 0, \tag{4.33}$$

to get the result

$$\Phi_{Y,j=0} = e^{-\gamma_0 |\omega|^\alpha}, \tag{4.34}$$

where

$$\gamma_0 = \frac{2c_1^{\alpha}c_n\rho_0\Gamma(1-\alpha)\cos\frac{\pi\alpha}{2}}{\nu\alpha}$$
$$\cdot \int_0^{\infty}\int_{\Theta}\int_0^{\infty} a^{\alpha}|E(t;\theta)|^{\alpha}f_a(a)f_{\theta}(\theta)\,dt\,d\theta\,da. \qquad (4.35)$$

(Note that the relation $\Gamma(1-\alpha) = -\alpha\Gamma(-\alpha)$ is used in (4.35)).

In order to solve for the $j = 1$ term of Eq. (4.30), rewrite it using this identity:

$$\sin^2(a)\cos(2b) = \frac{1}{2}\sin^2(a+b) + \frac{1}{2}\sin^2(a-b) - \sin^2(b) \qquad (4.36)$$

to get

$$\log\Phi_{Y,j=1}(\omega) = \int_0^{\infty}\int_{\Omega}\frac{\rho_0}{|\mathbf{x}|^{\mu}}\int_0^{\infty}\lambda_L e^{-\lambda_L\tau}\left\{ -8\lambda_1\int_{a_1=0}^{\infty}\int_{\Theta_1}\int_{a_2=0}^{\infty}\int_{\Theta_2}\int_{\tau'=t-\tau}^{t}\right.$$
$$\left[\frac{1}{2}\sin^2\left(\frac{1}{2}\omega c_1|\mathbf{x}|^{-\nu}(a_1 E(t;\theta_1) + a_2 E(\tau';\theta_2))\right)\right.$$
$$\left.+\frac{1}{2}\sin^2\left(\frac{1}{2}\omega c_1|\mathbf{x}|^{-\nu}(a_1 E(t;\theta_1) - a_2 E(\tau';\theta_2))\right)\right.$$
$$\left.\left. - \sin^2\left(\frac{1}{2}\omega c_1|\mathbf{x}|^{-\nu}a_1 E(t;\theta_1)\right)\right]\right\}d\tau'\ldots d\tau d\mathbf{x}\,dt. \qquad (4.37)$$

The three $\sin^2()$ terms in (4.37) may be integrated separately, each in a manner analogous to Eqs. (4.31) – (4.35), to determine the result

$$\Phi_{Y,j=1} = e^{-\gamma_1|\omega|^{\alpha}}, \qquad (4.38)$$

where

$$\gamma_1 = \frac{4c_1^{\alpha}c_n\rho_0\lambda_1\Gamma(1-\alpha)\cos\frac{\pi\alpha}{2}}{\nu\alpha}\int_0^{\infty}\int_0^{\infty}\lambda_L e^{-\lambda_L\tau}\int_{a_1=0}^{\infty}\int_{\Theta_1}\int_{a_2=0}^{\infty}\int_{\Theta_2}\int_{t-\tau}^{t}$$
$$\cdot\left[\frac{1}{2}|a_1 E(t;\theta_1) + a_2 E(\tau';\theta_2)|^{\alpha} + \frac{1}{2}|a_1 E(t;\theta_1) - a_2 E(\tau';\theta_2)|^{\alpha}\right.$$
$$\left. -|a_1 E(t;\theta_1)|^{\alpha}\right]d\tau'\,d\theta_2\,da_2\,d\theta_1\,da_1\,d\tau\,dt. \qquad (4.39)$$

Moving on to $j = 2$, the bracketed term

$$\int_{a=0}^{\infty} \int_{\Theta} \int_{t-\tau}^{t} d\tau' \left(\sin^2(\frac{1}{2}\omega a c_1 |\mathbf{x}|^{-\nu} E(\tau'; \theta)) \right) \qquad (4.40)$$

from Eq. (4.30) is now squared, resulting in

$$\int_{a_2=0}^{\infty} \int_{\Theta_2} \int_{t-\tau}^{t} d\tau_2' \int_{a_3=0}^{\infty} \int_{\Theta_3} \int_{t-\tau}^{t} d\tau_3'$$
$$\left(\sin^2(\frac{1}{2}\omega a_2 c_1 |\mathbf{x}|^{-\nu} E(\tau_2'; \theta_2)) \right) \left(\sin^2(\frac{1}{2}\omega a_3 c_1 |\mathbf{x}|^{-\nu} E(\tau_3'; \theta_3)) \right). \qquad (4.41)$$

Using the formula

$$\sin^2 a \sin^2 b = \frac{1}{2} \sin^2 a + \frac{1}{2} \sin^2 b - \frac{1}{4} \sin^2(a+b) - \frac{1}{4} \sin^2(a-b), \qquad (4.42)$$

results in an expression of the form of (4.37) but now there are nine $\sin^2()$ terms instead of three. When each is integrated as in (4.32) – (4.35), the result is

$$\Phi_{Y,j=2} = e^{-\gamma_2 |\omega|^{\alpha}} \qquad (4.43)$$

where

$$\gamma_2 = \frac{8 c_1^{\alpha} c_n \rho_0 \lambda_1^2 \Gamma(1-\alpha) \cos \frac{\pi \alpha}{2}}{\nu \alpha} \int_0^{\infty} \int_0^{\infty} \lambda_L e^{-\lambda_L \tau}$$
$$\int_0^{\infty} f_a da_1 \int_{\theta_1} f_\theta d\theta_1 \int_0^{\infty} f_a da_2 \int_{\theta_2} f_\theta d\theta_2 \int_{t-\tau}^{t} d\tau_2' \int_0^{\infty} f_a da_3 \int_{\theta_3} f_\theta d\theta_3 \int_{t-\tau}^{t} d\tau_3'$$
$$\left\{ \frac{1}{2} |a_1 E(t; \theta_1)|^{\alpha} \right.$$
$$- \frac{1}{4} |a_1 E(t; \theta_1) + a_2 E(\tau_2'; \theta_2)|^{\alpha} - \frac{1}{4} |a_1 E(t; \theta_1) - a_2 E(\tau_2'; \theta_2)|^{\alpha}$$
$$- \frac{1}{4} |a_1 E(t; \theta_1) + a_3 E(\tau_3'; \theta_3)|^{\alpha} - \frac{1}{4} |a_1 E(t; \theta_1) - a_3 E(\tau_3'; \theta_3)|^{\alpha}$$
$$+ \frac{1}{8} |a_1 E(t; \theta_1) + a_2 E(\tau_2'; \theta_2) + a_3 E(\tau_3'; \theta_3)|^{\alpha}$$
$$+ \frac{1}{8} |a_1 E(t; \theta_1) + a_2 E(\tau_2'; \theta_2) - a_3 E(\tau_3'; \theta_3)|^{\alpha}$$

$$+\frac{1}{8}|a_1 E(t;\theta_1) - a_2 E(\tau_2';\theta_2) + a_3 E(\tau_3';\theta_3)|^\alpha$$

$$+\frac{1}{8}|a_1 E(t;\theta_1) - a_2 E(\tau_2';\theta_2) - a_3 E(\tau_3';\theta_3)|^\alpha \Bigg\} \, d\tau \, dt. \qquad (4.44)$$

For the $j = 3, 4, 5 \ldots$ terms, each increment of j adds three additional integrations and multiplies the number of $\sin^2()$ terms (as in (4.37)) by three; however, the relation (4.42) may be applied repeatedly until 3^j individual $\sin^2()$ terms remain, with arguments consisting of the sums and differences of the $a_i E(\tau_i;\theta_i)$ terms. It follows that 3^j integrations of the form (4.32) – (4.35) may then be performed until the result

$$\Phi_{Y,j} = e^{-\gamma_j |\omega|^\alpha} \qquad (4.45)$$

is obtained, but the γ_j become increasingly complicated to express. Convergence is assured since the exponential Taylor series converges for all real arguments and by inspection of (4.29), from which it is apparent due to bounds on the sine and cosine functions that the term in braces is between -1 and 0 for all $\mathbf{x}, t$.

The final desired result $\Phi_X(\omega)$ is found by multiplying

$$\Phi_Y(\omega) = \prod_{j=0}^\infty \Phi_{Y,j} = e^{-\left(\sum_{j=0}^\infty \gamma_j\right)|\omega|^\alpha}, \qquad (4.46)$$

and thus it is proved that the characteristic function of the received noise pdf is that of an α-stable distribution. By the uniqueness of characteristic functions, this proves that the marginal pdf of the noise is an α-stable distribution.

4.3.1 Probability Density Function of the Noise Envelope

The previous sections derive the pdf of the received noise, but it remains to determine the statistics of the narrowband envelope. Since the $E(t,\theta)$'s of Eq. (4.1) may be assumed to include an arbitrary bandpass filter response without loss of generality, it remains only to prove that the equivalent lowpass signals (as in Eq. (2.1)) are jointly α-stable.

Let $E(t; \theta)$ be narrowband, so that it can be represented as

$$
\begin{aligned}
E(t; \theta) &= E_I(t; \theta) \cos(2\pi f_0 t) - E_Q(t; \theta) \sin(2\pi f_0 t) \\
&= A(t; \theta) \cos\phi \cos(2\pi f_0 t) - A(t; \theta) \sin\phi \sin(2\pi f_0 t),
\end{aligned}
$$

(4.47)

(4.48)

where A and ϕ are the complex amplitude and phase as in Section 2.3. Equation (4.4) may then be written

$$
\begin{aligned}
Y &= Y_I \cos(2\pi f_0 t) - Y_Q \sin(2\pi f_0 t) \\
&= \sum_{k=1}^{N_c} \left\{ X_{I_k} \cos(2\pi f_0 t) - X_{Q_k} \sin(2\pi f_0 t) \right\} \\
&= \sum_{k=1}^{N_c} \sum_{i=0}^{N_k} \frac{a_{k,i} c_1}{|\mathbf{x}|^\nu} \left\{ A(t_{k,i}; \theta_{k,i}) \cos\phi_{k,i} \cos(2\pi f_0 t) \right. \\
&\qquad\qquad \left. - A(t_{k,i}; \theta_{k,i}) \sin\phi_{k,i} \sin(2\pi f_0 t) \right\}.
\end{aligned}
$$

(4.49)

(4.50)

(4.51)

Now assume the ϕ's are i.i.d. uniform $[0, 2\pi)$, as in Section 2.3. The joint characteristic functions $\Phi_{X_I, X_Q}(\underline{\omega})$ and $\Phi_{Y_I, Y_Q}(\underline{\omega})$ (where again $\underline{\omega} = (\omega_1, \omega_2)$) may be determined using an analysis similar to that of the previous section, the equivalent of Eq. (4.29) being

$$
\log \Phi_{Y_I, Y_Q}(\underline{\omega}) = \int_0^T \int_\Omega \frac{\rho_0}{|\mathbf{x}|^\mu}
$$

$$
\left\{ \left[2 \int_{a=0}^\infty \int_\Theta \frac{1}{2\pi} \int_0^{2\pi} d\phi \, \cos\left(a c_1 |\mathbf{x}|^{-\nu} A(t; \theta)(\omega_1 \cos\phi + \omega_2 \sin\phi) \right) \right] \left[\int_0^\infty \lambda_L e^{-\lambda_L \tau} \right.\right.
$$

$$
\left.\left. e^{\left[-4\lambda_1 \int_{a=0}^\infty \int_\Theta \int_{t-\tau}^t d\tau' \frac{1}{2\pi} \int_0^{2\pi} d\phi \sin^2\left(\frac{1}{2} a c_1 |\mathbf{x}|^{-\nu} A(\tau'; \theta)(\omega_1 \cos\phi + \omega_2 \sin\phi)\right) \right]} d\tau \right] - 1 \right\} \, d\mathbf{x} \, dt.
$$

(4.52)

Using a Taylor series as before and noting that $\omega_1 \cos\phi + \omega_2 \sin\phi$ may be written $|\underline{\omega}| \cos(\phi - \phi_{\underline{\omega}})$ (where $\phi_{\underline{\omega}} = \arctan(\frac{\omega_2}{\omega_1})$), the equivalent of Eq. (4.30) is

$$
\log \Phi_{Y_I, Y_Q}(\underline{\omega}) = \int_0^T \int_\Omega \frac{\rho_0}{|\mathbf{x}|^\mu}
$$

$$\left\{ \left[2 \int_{a=0}^{\infty} \int_{\Theta} \frac{1}{2\pi} \int_{0}^{2\pi} d\phi \cos\left(|\omega| a c_1 |\mathbf{x}|^{-\nu} A(t;\theta) \cos(\phi - \phi_{\underline{\omega}}) \right) \right] \right.$$

$$\left[\int_{0}^{\infty} \lambda_L e^{-\lambda_L \tau} \left(\sum_{j=0}^{\infty} \frac{(-4\lambda_1)^j}{j!} \left[\int_{a=0}^{\infty} \int_{\Theta} \int_{t-\tau}^{t} d\tau' \frac{1}{2\pi} \int_{0}^{2\pi} d\phi \right. \right. \right.$$

$$\left. \left. \left. \sin^2\left(\frac{1}{2} |\omega| a c_1 |\mathbf{x}|^{-\nu} A(\tau';\theta) \cos(\phi - \phi_{\underline{\omega}}) \right) \right]^j \right) d\tau \right] - 1 \right\} \, d\mathbf{x} \, dt. \qquad (4.53)$$

Comparing (4.53) to (4.30), it is apparent that Φ_{Y_I, Y_Q} may be solved in the manner of Eqs. (4.30) – (4.46) to determine

$$\Phi_{Y_I, Y_Q}(\underline{\omega}) = \prod_{j=1}^{\infty} \Phi_{Y_I, Y_Q, j} = e^{-\left(\sum_{j=1}^{\infty} \gamma_j \right) |\omega|^{\alpha}}, \qquad (4.54)$$

where for example

$$\gamma_0 = \frac{2 c_1^{\alpha} c_n \rho_0 \Gamma(1 - \alpha) \cos \frac{\pi \alpha}{2}}{\nu \alpha} \frac{1}{2\pi} \int_{0}^{2\pi} |\cos \phi|^{\alpha} d\phi$$

$$\cdot \int_{0}^{\infty} \int_{\Theta} \int_{0}^{\infty} a^{\alpha} |A(\tau;\theta)|^{\alpha} f_a(a) f_{\theta}(\theta) \, dt \, d\theta \, da. \qquad (4.55)$$

The characteristic function Eq. (4.54) defines an isotropic α-stable random vector. It is shown in [37] that such a random vector has a complex envelope $A = \sqrt{X_I^2 + X_Q^2}$ with the pdf of Eq. (3.5); therefore, it is finally proved that the clustering Poisson model predicts an α-stable envelope distribution for A.

4.3.2 Validity of Parameters

The parameter ν in Eq. (4.1) is the rate of attenuation of the noise signals with distance; typical values used in previous models range from 0.5 to 1.0 [18]. Given that $n = 2$ is the most realistic choice from a physical standpoint (or perhaps slightly larger than two for an empirical approximation), and μ is fairly small since the source density does not decay significantly with distance, it follows that values of α in the range 1.5 – 2.0 are quite reasonable. Note that for $n > \nu + \mu$, the noise

is infinite when $R_2 \to \infty$, but this is compensated for by fixing R_2 at some large value $R_{\max}$ with the assumption that it does not appreciably affect the integrals of the form of (4.32) – (4.35).

4.3.3 Arbitrary Receiver Gain Pattern

The preceding analyses assume that the receiver's gain pattern is omnidirectional, *i.e.*, the same in all directions. It is now shown that if the receiver has an arbitrary gain pattern, the received noise waveform is still α-stable distributed. This result follows because the key integration that results in the α-stable distribution, Eqs. (4.32) – (4.35), is over distance r from the receiver and not over angle of arrival.

An arbitrary gain pattern may be incorporated without loss of generality as a functional dependence of $f_a(a)$ on direction angle ζ ($n = 2$ is assumed, again without loss of generality), so that $f_a(a)$ is now $f_{a|\zeta}(a, \zeta)$. Using this modification, Eq. (4.32) becomes, for example,

$$\Phi_{Y,j=0} = e^{-\frac{4c_n\rho_0}{\nu}\left[\int_{t=0}^{T}\frac{1}{2\pi}\int_{0}^{2\pi}d\zeta\int_{a=0}^{\infty}f_{a|\zeta}(a,\zeta)\int_{\Theta}\int_{r=R_1}^{R_2}\sin^2(\frac{1}{2}wac_1rE(t;\theta))r^{-\alpha-1}dr\right]}, \quad (4.56)$$

which still results in an expression of the form

$$\Phi_{Y,j=0} = e^{-\gamma_0|\omega|^\alpha}, \quad (4.57)$$

but now γ_0 is

$$\gamma_0 = \frac{2c_1^\alpha c_n\rho_0\Gamma(1-\alpha)\cos\frac{\pi\alpha}{2}}{\nu\alpha}$$
$$\cdot\frac{1}{2\pi}\int_0^{2\pi}\int_0^\infty\int_\Theta\int_0^\infty a^\alpha|E(t;\theta)|^\alpha f_{a|\zeta}(a,\zeta)f_\theta(\theta)\,dt\,d\theta\,da\,d\zeta. \quad (4.58)$$

All the other $\Phi_{Y,j}$ terms will have the same modification to their γ_j terms, and the final result will still have a characteristic function of the form of (4.46) and (4.54). Thus an arbitrary gain pattern may be added to the analysis without changing the result that the noise is α-stable distributed.

4.4 Impulse Interarrival Distribution of Clustered Poisson Noise

This section shows that the clustering Poisson model accurately predicts the impulse interarrival time distributions of low-frequency noise. Predicted interarrival distributions are determined from the model, and these are shown to match the distributions derived from the data.

As defined in Section 4.2.3, the clustering model proposes that the number of follow-on impulses (after the first) within a given cluster is a geometric random variable, and that the interarrival times between adjacent impulses within each cluster are independent and $EXP(\lambda_1)$ distributed. The total process is the superposition of all the impulses in all the clusters, and the clusters themselves are occurrences of a Poisson random process with parameter λ_2 clusters per second.

Since the occurrence of an impulse is defined as the crossing of a threshold level as in Figure 2.7, the individual impulses can be represented for simplicity as Dirac delta functions. The total process can then be expressed as

$$y(t) = \sum_{k=-\infty}^{\infty} \sum_{i=0}^{N_k} \delta(t - t_k - \tau_{k,i}), \tag{4.59}$$

where N_k is the number of impulses in cluster k, t_k is the start time of cluster k, and $\tau_{k,i}$ is the time from the start of the cluster k to the ith impulse of cluster k. (Time is now in the forward direction). Note that $\tau_{k,0} = 0$ for all k, and also that $N_k = 0$ for clusters with no follow-on impulses.

If a stopwatch is started at an arbitrary point in time and stopped at the next occurrence of an impulse, the time shown on the stopwatch is the waiting time for the next impulse, or the *forward recurrence* time. The forward recurrence time is a random variable T_W with marginal pdf $f_{T_W}(t)$.

If the stopwatch is instead started at the occurrence of an arbitrary impulse and stopped at the next impulse, the time on the stopwatch is the impulse interarrival time. This random variable is denoted T_I, with marginal pdf $f_{T_I}(t)$. The following sections derive both $f_{T_W}(t)$ and $f_{T_I}(t)$ for the clustering Poisson model, and then

compare the derived $f_{T_W}(t)$ to the interarrival distributions seen in the data.

4.4.1 Waiting Time pdf

The pdf $f_{T_W}(t)$ of the forward recurrence time of the process $y(t)$ is most easily calculated by setting the time origin ($t = 0$) to be the stopwatch's starting time, then determining the probability that there are no impulses in the time span $[0, t]$. It follows that $1 - P(\text{no impulses in } [0, t])$ is the probability that the waiting time is less than t, so differentiating this quantity results in the pdf $f_{T_W}(t)$.

In order to find $P(\text{no impulses in } [0, t])$, the pmf of N_0, the number of clusters active at time zero, must be calculated. This pmf is calculated in three steps: (i) The number of clusters N created in the range $[-T, 0]$ is a Poisson($\lambda_2 T$) random variable. If ordering is neglected, the starting times of these clusters are uniformly distributed over $[-T, 0]$ and are independent of each other. The probability P_A that any given cluster X_k with starting time $t_k \sim U([-T, 0])$ is active at $t = 0$ can then be calculated by conditioning on t_k:

$$
\begin{aligned}
P_A &\doteq P(\text{cluster starting in } [-T, 0] \text{ is active at } t = 0) \\
&= \frac{1}{T} \int_{-T}^{0} P(T_L > -\tau) \, d\tau \\
&= \frac{1}{\lambda_L T} \left(1 - e^{-\lambda_L T} \right).
\end{aligned}
\tag{4.60}
$$

(ii) Now condition on N: given N clusters with starting times uniformly and independently distributed over $[-T, 0]$, each with a probability of surviving past $t = 0$ given by (4.60), then the number of clusters surviving at $t = 0$ is a binomial random variable:

$$
\begin{aligned}
&P(k \text{ clusters active at } t = 0 | N) \\
&= \frac{N!}{k!(N-k)!} P_A^k (1 - P_A)^{N-k}, \ k = 0, 1, 2 \ldots N.
\end{aligned}
\tag{4.61}
$$

(iii) Since N is Poisson($\lambda_2 T$), the final result is

$$
\begin{aligned}
P(k \text{ clusters active at } t = 0) \\
= \sum_{n=k}^{\infty} \frac{(\lambda_2 T)^n e^{-\lambda_2 T}}{n!} \frac{n!}{k!(n-k)!} P_A^k (1 - P_A)^{n-k}, \; k \geq 0 \quad (4.62)
\end{aligned}
$$

$$
= \frac{e^{-\lambda_2 T}}{k!} \left(\frac{P_A}{1 - P_A} \right)^k \sum_{n=0}^{\infty} \frac{(\lambda_2 T)^{k+n}}{n!} (1 - P_A)^{k+n} \quad (4.63)
$$

$$
= \frac{\left(\lambda_2 T \left(\frac{1}{\lambda_L T} \left(1 - e^{-\lambda_L T} \right) \right) \right)^k e^{-\lambda_2 T \left(\frac{1}{\lambda_L T} \left(1 - e^{-\lambda_L T} \right) \right)}}{k!}, \quad (4.64)
$$

where (4.63) results from a change of variables $n \Rightarrow k+n$. From (4.64) it is clear that N_0 is a Poisson random variable a parameter equal to $\lambda_2 T$ scaled by the probability (4.60), a well-known result for a Poisson process modulated by an indicator function. Setting $T \to \infty$, the final result is that N_0 is a Poisson(λ_2 / λ_L) random variable.

Each of the N_0 clusters active at $t = 0$ has as least one impulse remaining. In addition, from the memoryless property of exponential random variables, the first impulse after time zero in each of these clusters has a time of occurrence that is EXP(λ_1) distributed. Therefore, in order for there to be no impulses in $[0, t]$, all N_0 active clusters must have their next impulse occur after t. Conditioning on N_0 results in

$$
\begin{aligned}
P(\text{no impulses in } [0, t] \text{ due to clusters starting before time } 0) \\
= \sum_{n=0}^{\infty} \frac{\left(\frac{\lambda_2}{\lambda_L} \right)^n e^{-\left(\frac{\lambda_2}{\lambda_L} \right)}}{n!} \left(e^{-\lambda_1 t} \right)^n \quad (4.65)
\end{aligned}
$$

$$
= e^{-\frac{\lambda_2}{\lambda_L} \left(1 - e^{-\lambda_1 t} \right)}. \quad (4.66)
$$

Taking into account that there must be no new clusters in $[0, t]$ as well,

$$
P(\text{no impulses in } [0, t]) = e^{-\lambda_2 t} e^{-\frac{\lambda_2}{\lambda_L} \left(1 - e^{-\lambda_1 t} \right)}, \quad (4.67)
$$

and so the forward recurrence pdf is finally found by negating the derivative of

Eq. (4.67):

$$f_{T_W}(t) = \left[\lambda_2 + \frac{\lambda_2 \lambda_1}{\lambda_L} e^{-\lambda_1 t} \right] e^{-\frac{\lambda_2}{\lambda_L}\left(1 - e^{-\lambda_1 t}\right)} e^{-\lambda_2 t}. \tag{4.68}$$

4.4.2 Interarrival Time pdf

The interarrival pdf $f_{T_I}(t)$ calculation is similar to the forward recurrence calculation except that there is by definition an impulse at time $t = 0$. It is not known whether this impulse is the first impulse of a new cluster or an additional impulse from an established cluster, however, so it is necessary to condition over both possibilities.

First calculate the expected value of the number of impulses in a cluster, which is $1 + E[N_k]$. Using the pmf (4.14), this value is

$$
\begin{aligned}
1 + E[N_k] &= 1 + \sum_{n=0}^{\infty} \frac{n \lambda_L}{\lambda_1 + \lambda_L} \left(\frac{\lambda_1}{\lambda_1 + \lambda_L} \right)^n \\
&= 1 + \frac{\lambda_1}{\lambda_L}. \tag{4.69}
\end{aligned}
$$

Furthermore, if the process is modeled as existing for all time, the probability that any single impulse is the first of its cluster is the reciprocal of (4.69). Using both this information and Eq. (4.67), in addition to the fact that a new cluster at time $t = 0$ must not cause an impulse in $(0, t]$, results in

$$P(\text{no impulses in } (0, t] \text{ given an impulse at } t = 0)$$
$$= \left(\frac{1}{E[N_k + 1]} e^{-\lambda_1 t} + \frac{E[N_k]}{E[N_k + 1]} \right) e^{-\lambda_2 t} e^{-\frac{\lambda_2}{\lambda_L}\left(1 - e^{-\lambda_1 t}\right)}. \tag{4.70}$$

Negating the derivative of (4.70) then gives the marginal interarrival pdf

$$
\begin{aligned}
f_{T_I}(t) &= \frac{e^{-\lambda_2 t - \frac{\lambda_2}{\lambda_L}\left(1 - e^{-\lambda_1 t}\right)}}{\lambda_1 + \lambda_L} \\
&\cdot \left(\lambda_1 \lambda_2 + \left[\lambda_1 \lambda_L + \lambda_2 \lambda_L + \frac{\lambda_1^2 \lambda_2}{\lambda_L} \right] e^{-\lambda_1 t} + \lambda_1 \lambda_2 e^{-2\lambda_1 t} \right), \quad t \geq 0. \tag{4.71}
\end{aligned}
$$

Threshold	λ_1 (s^{-1})	λ_2 (s^{-1})	λ_L (s^{-1})
$5E[\|X\|]$	12.76	4.71	1.29
$10E[\|X\|]$	9.17	2.84	1.06
$15E[\|X\|]$	7.42	2.09	0.95
$20E[\|X\|]$	6.07	1.71	0.89

Table 4.1: Parameter values of the clustering Poisson pdf's in Figure 4.1

4.4.3 Data Analysis

Now that $f_{T_I}(t)$ has been determined, it is compared to the impulse spacings seen in low-frequency noise data. Figure 4.1 shows the fit of Eq. (4.71) to the interarrival time pdf of Arrival Heights noise data in the 25.5 – 27.5 kHz range, for the whole month of December 1995, during the hours 08 – 16 UT of each day. The four lines in the plot are for threshold levels of 5, 10, 15 and 20 times the expected value of the magnitude of the noise. The accurate fit of Eq. (4.71) to the data is quite apparent from the dotted lines in the figure; the parameter values used for each dotted line are listed in Table 4.1.

Many more data samples were examined in addition to those in Figure 4.1, but all of them have the same form for their interarrival pdf's independent of threshold level (as long as the threshold is large enough to distinguish impulses from background noise). The term λ_2 varies with location and seasonal and diurnal variations, but average cluster length is always on the order of one second and λ_1 is on the order of 5 – 10.

4.4.4 Physical Justification of the Model

Since the clustering Poisson equation (4.59) of Section 4.4,

$$y(t) = \sum_{k=-\infty}^{\infty} \sum_{i=0}^{N_k} \delta(t - t_k - \tau_{k,i}), \qquad (4.72)$$
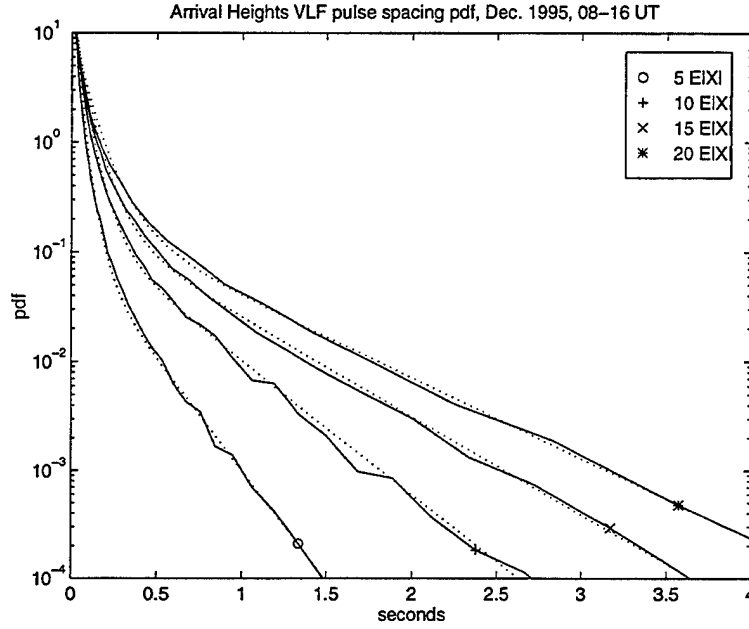
Figure 4.1: Fit of the clustering Poisson impulse interarrival pdf, Eq. (4.71) (dotted lines), to Arrival Heights impulse interarrival data. The threshold levels are 5, 10, 15 and 20 times the first moment of the noise.

differs from equation (4.4) of Section 4.2.2:

$$Y = \sum_{k=1}^{N_c} X_k = \sum_{k=1}^{N_c} \sum_{i=0}^{N_k} \frac{c_1 a_{k,i}}{\mathbf{x}^{\nu}} E(\tau_{k,i}; \theta_{k,i}), \qquad (4.73)$$

it remains to specify the connection between the two. Note that $y(t)$ in (4.72) is a waveform that represents the detection of impulses above a certain threshold, while Y in (4.73) is the received signal at a given point in time.

Begin by defining the range r to be the distance from a given cluster's source to the receiver ($r = |\mathbf{x}|$), and note that it depends only on $|a|$ and r whether or not an impulse crosses a given threshold Y_{th} in the received waveform; i.e., it can be specified with no essential loss of generality that $c_1 = 1$ and $\max |E(\tau_{k,i}; \theta_{k,i})| = 1$, independent of θ. The probability that an impulse from the cluster crosses Y_{th}, as

a function of r and Y_{th}, is then

$$P_{r,Y_{th}} = P\left(\frac{|a|}{r^\nu} > Y_{th}\right) = 2\int_{Y_{th}r^\nu}^\infty f_a(a)\,da. \tag{4.74}$$

However, this poses a problem, since it is not known from the received waveform how many impulses and/or entire clusters have gone undetected because of small values of a. In order to proceed further, it is approximated that for a given Y_{th}, there exists some cutoff distance r_c such that all clusters with $r > r_c$ can be ignored. This cutoff distance is chosen to be

$$r_c = \frac{R_0}{Y_{th}} \tag{4.75}$$

for some constant R_0.

For the region $r < r_c$, the spatial density of clusters is given by Eq. (4.3):

$$\rho(r) = \frac{\rho_0}{r^\mu}, \tag{4.76}$$

but some of the clusters (especially for r near r_c) will still go undetected due to propagation attenuation. To compensate for propagation effects, an effective source density is defined as

$$\hat{\rho}(r) = \frac{\rho_0}{r^{\mu+\nu}}. \tag{4.77}$$

Using this effective source density, it is assumed that all clusters with $r < r_c$ are detected. Thus the effective number of spatial cluster sources for threshold Y_{th}, in units of $1/s$, is

$$\lambda_2 = \int_0^{\frac{R_0}{Y_{th}}} \frac{\rho_0 c_n r^{n-1}}{r^{\mu+\nu}}\,dr, \tag{4.78}$$

and carrying out this integration gives

$$\lambda_2 = \left(\frac{\rho_0 c_n R_0^{n-\mu-\nu}}{n-\mu-\nu}\right) Y_{th}^{-(n-\mu-\nu)}, \tag{4.79}$$

a polynomial in Y_{th}. To confirm the validity of this approximation, the values of relative threshold level and λ_2 listed in Table 4.1 were fit to Eq. (4.79) by taking

the logarithm of both sides of (4.79) and using a linear regression. The exponent $n - \mu - \nu = 0.73$ was found to give a very good fit, and is physically justified by the expected values of $n \approx 2$, $\nu \approx 1.0$, and μ a small positive number. Thus a physical connection between the parameters of (4.72) and (4.73) is shown. (The first term in parentheses in (4.79) is 15.3, but this number is irrelevant since ρ_0 is unknown, R_0 is arbitrary and only relative threshold levels are used).

It is seen from the values of λ_1 and λ_L in Table 4.1 that the expected number of impulses per cluster, $1 + \lambda_1/\lambda_L$, is on the order of 5 – 10.

4.5 Power Spectral Density of Clustered Poisson Noise

This section derives the power spectral density (PSD) of clustered Poisson noise. It is shown that clustering has an effect on the power spectral density only when the impulses within clusters are correlated, so for the clustering Poisson model of Section 4.2.2, the PSD is simply the ensemble average of the PSD's of individual impulses. This is confirmed in the data by calculating PSD's of (i) isolated impulses, and (ii) clustered impulses, and showing that they are the same.

Consider a simple Poisson filtered-impulse random process

$$Y(t) = \sum_{k=-\infty}^{\infty} X_k(t - t_k), \tag{4.80}$$

where X_k is the random waveform of the kth event and t_k is its time of occurrence. Since the occurrence of events is a Poisson process, the random variables $t_k - t_{k-1}$ are i.i.d. $\sim \text{EXP}(\lambda)$. The two-sided power spectral density of $Y(t)$ is given in [22] as

$$S_Y(f) = \lambda E[|\mathcal{X}(f)|^2] + (\lambda E[\mathcal{X}(0)])^2 \delta(f), \ f \in \Re \tag{4.81}$$

where $\mathcal{X}(f)$ is the Fourier transform (FT) of $x(t)$,

$$\mathcal{X}(f) = \int_{-\infty}^{\infty} x(t)e^{-i2\pi ft} \, dt, \tag{4.82}$$

and $x(t)$ is a given realization of $X_k(t)$ (or $X(t)$; the subscript may be dropped since the $X_k(t)$'s are i.i.d. waveforms).

Now define the X_k's of Eq. (4.80) to be cluster waveforms similar to those in Eq. (4.4):

$$X_k(t - t_k) = \sum_{i=0}^{N_k} \frac{c_1 a_{k,i}}{|\mathbf{x}_k|^\nu} E(t - t_k - \tau_{k,i}; \theta_{k,i}), \qquad (4.83)$$

where the $\tau_{k,i}$ now refer to the position of the ith impulse of the kth cluster relative to the start of that cluster. Then let $Y(t)$ be the sum of all the clusters:

$$Y(t) = \sum_{k=1}^{N_c} \sum_{i=0}^{N_k} \frac{c_1 a_{k,i}}{|\mathbf{x}_k|^\nu} E(t - t_k - \tau_{k,i}; \theta_{k,i}). \qquad (4.84)$$

The PSD of Y is still Eq. (4.81), but now (4.83) is inserted into (4.80). Note once again that clusters start with an impulse (the $i = 0$ terms), and the N_k's are i.i.d. geometric random variables for all k.

The clusters come from a variety of locations $\mathbf{x}$ and distances $|\mathbf{x}|$ and they are all independent, so the resulting PSD of Y is the summed contributions from all locations. Integrating over the region using $r = |\mathbf{x}|$ and ignoring the zero frequency (second) term of Eq. (4.81) (it is assumed to be zero) gives

$$S_Y(f) = \left(\int_0^{R_{\max}} \frac{c_n r^{n-1} \rho_0}{r^{\nu + \mu}} dr \right) E\left[|\text{FT of any one cluster}|^2 \right], \qquad (4.85)$$

where the term in parentheses is the effective source density normalized by propagation attenuation, as in Section 4.4.4. ($R_{\max}$ is as in Section 4.3.2). Further defining this term in parentheses as $\bar{\lambda}$ and the waveform of any one cluster relative to its starting point as

$$X(t) = \sum_{i=0}^{N} c_1 a_i E(t - \tau_i; \theta_i), \qquad (4.86)$$

Eq. (4.85) can be written as

$$S_Y(f) = \bar{\lambda} E[|\mathcal{X}(f)|^2] \qquad (4.87)$$

$$= \bar{\lambda}E\left[\left|\int_{-\infty}^{\infty}\left(\sum_{i=0}^{N}c_1 a_i E(t-\tau_i;\theta_i)\right)e^{-j2\pi ft}\,dt\right|^2\right] \qquad (4.88)$$

$$= c_1^2\bar{\lambda}E\left[\left|\sum_{i=0}^{N}a_i\mathcal{E}(f;\theta_i)e^{-j2\pi f\tau_i}\right|^2\right] \qquad (4.89)$$

$$= c_1^2\bar{\lambda}E\left[\sum_{i=0}^{N}\sum_{j=0}^{N}a_i a_j^*\mathcal{E}(f;\theta_i)\mathcal{E}^*(f;\theta_j)e^{-j2\pi f(\tau_i-\tau_j)}\right] \qquad (4.90)$$

where $\mathcal{E}(f;\theta)$ is the Fourier transform of $E(t;\theta)$ and (4.89) results from the Fourier shift property. In order to proceed further, allow the a_i's to be wide sense stationary with autocorrelation function $R(k)$. (They are still mean zero with variance $\sigma_a^2 = R(0)$). Breaking the double sum into terms for which $i = j$ and terms for which $i \neq j$ and including the change of variable $k \Rightarrow |j - i|$ in the latter gives

$$S_Y(f) = \bar{\lambda}c_1^2(1+\frac{\lambda_1}{\lambda_L})\sigma_a^2 E\left[|\mathcal{E}(f;\theta)|^2\right] + c_1^2\bar{\lambda}\,|E\left[\mathcal{E}(f;\theta)\right]|^2$$
$$\cdot\left[\sum_{i=0}^{N-1}\sum_{k=1}^{N-i}R(k)\left(E[e^{j2\pi f(\tau_{i+k}-\tau_i)}]+E[e^{-j2\pi f(\tau_{i+k}-\tau_i)}]\right)\right]. \qquad (4.91)$$

However, the last two expectation terms are the characteristic function of the sum of k interarrival times within a cluster, and that characteristic function's complex conjugate, using $2\pi f$ as the frequency variable instead of ω. Since the interarrival times are i.i.d. $\sim$ EXP(λ_1), the characteristic function expression is simply

$$E[e^{j2\pi f(\tau_{i+k}-\tau_i)}] = \Phi^k(f), \qquad (4.92)$$

where

$$\Phi(f) = \int_0^{\infty}\lambda_1 e^{-\lambda_1 t}e^{j2\pi ft}\,dt = \frac{\lambda_1}{\lambda_1 - j2\pi f}. \qquad (4.93)$$

Now consider two different cases for the autocorrelation $R_a(k)$: For the first case, set $R_a(k) = \sigma_a^2\delta(k)$, so that

$$S_Y(f) = \bar{\lambda}c_1^2(1+\frac{\lambda_1}{\lambda_L})\sigma_a^2 E\left[|\mathcal{E}(f;\theta)|^2\right]. \qquad (4.94)$$

In this case the PSD of the signal Y is simply a scaled version of the PSD of the individual impulse waveforms.

For the second case, let $R_a(k) = \sigma_a^2 \beta^{|k|}$ where $0 < \beta \leq 1$. The double sum in (4.91) can be converted to a single sum such that $S_Y(f)$ can be written

$$
\begin{aligned}
S_Y(f) &= \bar{\lambda} c_1^2 (1 + \frac{\lambda_1}{\lambda_L}) \sigma_a^2 E\left[|\mathcal{E}(f;\theta)|^2\right] + c_1^2 \bar{\lambda} \left|E\left[\mathcal{E}(f;\theta)\right]\right|^2 \sigma_a^2 \\
&\quad \cdot E_N\left[\sum_{k=1}^N (N+1-k)\left(\beta^k \Phi^k(f) + \beta^k \Phi^{k*}(f)\right)\right],
\end{aligned}
\qquad (4.95)
$$

which indicates that Φ is simply scaled by β for this case of $R(k)$.

In order to solve the last expectation in (4.95), algebraic summation formulas are used to find

$$
\sum_{k=1}^N (N+1-k)\Phi^k = \frac{(N+1)(1-\Phi)\Phi - \Phi + \Phi^{N+2}}{(1-\Phi)^2},
\qquad (4.96)
$$

and since N is geometric as in Eq. (4.6), it then follows that

$$
\begin{aligned}
&E_N\left[\sum_{k=1}^N (N+1-k)\beta^k \Phi^k(f)\right] \\
&= \frac{\left(1 + \frac{\lambda_1}{\lambda_L}\right)(1 - \beta\Phi(f))\beta\Phi(f) - \beta\Phi(f) + \frac{\lambda_L(\beta\Phi(f))^2}{\lambda_L + \lambda_1 - \lambda_1 \beta\Phi(f)}}{(1 - \beta\Phi(f))^2}.
\end{aligned}
\qquad (4.97)
$$

This result, when inserted into (4.95), is cumbersome to solve, but it can be simplified somewhat with the approximation $f \gg \lambda_1$, which is true for the VLF frequency range. (Note from Table 4.1 that λ_1 is on the order of 10). Using this approximation,

$$
\begin{aligned}
&E_N\left[\sum_{k=1}^N (N+1-k)\left(\beta^k \Phi^k(f) + \beta^k \Phi^{k*}(f)\right)\right] \\
&\approx \frac{\lambda_1}{\lambda_L}\left[\frac{\beta\lambda_1}{\lambda_1 - j2\pi f} + \frac{\beta\lambda_1}{\lambda_1 + j2\pi f}\right],
\end{aligned}
\qquad (4.98)
$$

and so

$$S_Y(f) \approx \bar{\lambda}c_1^2(1 + \frac{\lambda_1}{\lambda_L})\sigma_a^2 E\left[|\mathcal{E}(f;\theta)|^2\right] + \frac{\beta c_1^2 \bar{\lambda}\lambda_1^3 \sigma_a^2}{2\pi^2 f^2 \lambda_L} |E\left[\mathcal{E}(f;\theta)\right]|^2 . \qquad (4.99)$$

Upon examination of (4.99) it is apparent that the second term, the one due to clustering, is negligible relative to the first for large values of f. Therefore, in the VLF range, clustering has no effect on the power spectral density even if the a_i's are highly correlated. To verify this fact in the data, 1/10 second samples containing one isolated sferic (within a one second interval) were frequency transformed, then compared with the frequency transform of those 1/10 second samples containing many sferics. Averages of all the transforms of the June 1986 data at Thule, Greenland are shown in Figure 4.2; it is clearly seen that there is no difference in the form of the two power spectral density curves. (The y-axis is a relative index only; the plots for the two cases are offset for clarity. The rolloff below 5 kHz is due to a high-pass filter inserted to reduce power line harmonics). Although these results do not provide any additional proof of clustering, they do show that clustering does not affect the PSD of a signal in the VLF frequency range.

4.6   Conclusions

This chapter proposes a statistical-physical clustering Poisson model for atmospheric noise. According to the model, the sources of the noise are clusters of impulses with independent and identically distributed waveforms. Cluster occurrence is a spatial and temporal Poisson process with source distribution independent of direction and time. The impulses within clusters are defined as variable length Poisson processes. The clustering Poisson model is justified by the physical properties of lightning, and in addition, it is derived in conjunction with a statistical analysis of thousands of hours of globally collected ELF/VLF/LF radio noise data.

The model is verified by comparing it to four statistical features of atmospheric radio noise: correlations between impulses (Section 2.5), envelope amplitude probability distributions (Section 4.3), impulse spacings (Section 4.4), and power spectral
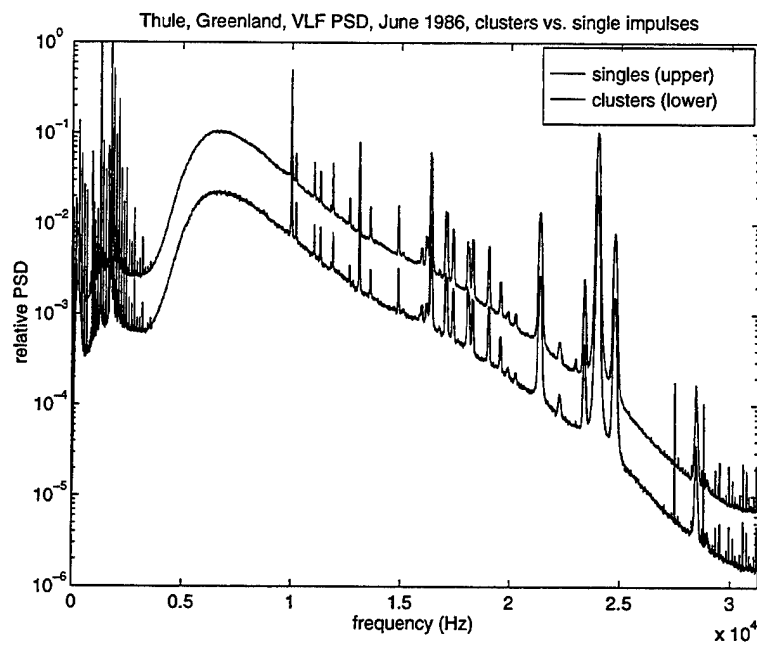
Figure 4.2: Spectral content of individual sferics versus clusters of sferics. The data are from June 1986, at Thule, Greenland. There is a lowpass filter inserted near 7 kHz. The spikes below 5 kHz are power line harmonics, and the spikes above 10 kHz are other man-made signals as in Figures 1.2 and 1.3.

densities (Section 4.5). The correlation properties justify the assumption that the a's of Eq. (4.4) are i.i.d. and that the clusters and impulses within them are independent as well. The envelope pdf and impulse spacing analyses clearly indicate that the theory of the model closely matches the data, and finally, clustering of pulses is shown to have little effect on the power spectral density of the noise.

Given the accuracy to which the predicted statistical features fit the actual data, the clustering Poisson model proves to be a good candidate as a model for atmospheric noise.

Chapter 5

Low-Frequency Communications

5.1 Introduction

As discussed in Chapter 1, there are a number of digital communication systems that operate with carrier frequencies in the VLF and LF frequency bands, and they employ receivers specifically designed for impulsive noise. Since the best receivers are based on knowledge of the statistics of the additive interfering noise, and since the previous chapters present results on the statistical analysis and modeling of VLF/LF noise, it is possible that these results may be used to design better performing receivers than those currently in use.

Specifically, it is shown in Chapter 3 that low-frequency noise has an α-stable envelope distribution at locations relatively distant from heavy sferic activity. Since many VLF/LF communication systems are designed to operate at such locations, it is of practical use to determine whether or not a receiver designed specifically for α-stable noise is worth its complexity in terms of reduced bit error rate (BER).

This chapter presents receivers designed for operation in α-stable noise and compares their BER performance to the conventional nonlinear analog receivers commonly used with impulsive noise, such as clippers, blankers, limiters and log-correlators. The signal formats examined are quadrature phase-shift keying (QPSK) and 16 point quadrature amplitude modulation (16 QAM), *i.e.*, two or four constellation points per signal dimension. Hundreds of simulations using time-series data

78

from various times and locations and at various center frequencies and bandwidths are performed, and the following results are found uniformly: for QPSK signals, virtually no performance improvement is gained when using an α-stable receiver instead of a clipper (the best conventional receiver), but for 16 QAM signals, an improvement of several dB is gained by using an α-stable receiver. In addition, it is found in some cases that, due to the nature of impulsive noise, 16 QAM offers a lower BER than QPSK for the same average transmitted power and data rate.

5.2 Receiver Structures for Impulsive Noise

This section assumes basic knowledge of digital communications, and begins with the problem already cast into a vector form. Reviews of digital communication concepts can be found in [32, 38, 43].

First start with binary phase-shift keying (BPSK). The receiver must choose between two equally probable hypotheses h_0 and h_1 (representing either a zero or a one bit) based on the received vector $\mathbf{X}$:

$$h_1 : \quad \mathbf{X} = \mathbf{S} + \mathbf{N},$$
$$h_0 : \quad \mathbf{X} = -\mathbf{S} + \mathbf{N},$$

where $\mathbf{X}, \mathbf{N}$ and $\mathbf{S}$ are complex n-vectors. This problem may be readily generalized to QPSK in two dimensions, noting that the simulations do not not perform symbol detection (*i.e.*, the inphase and quadrature channels are decoded separately).

For 4PAM (pulse amplitude modulation), the problem is that of choosing between the four choices

$$h_{1,0} : \quad \mathbf{X} = 3\mathbf{S} + \mathbf{N},$$
$$h_{1,1} : \quad \mathbf{X} = \mathbf{S} + \mathbf{N},$$
$$h_{0,1} : \quad \mathbf{X} = -\mathbf{S} + \mathbf{N},$$
$$h_{0,0} : \quad \mathbf{X} = -3\mathbf{S} + \mathbf{N},$$

where the subscripts on h indicate the bit assignments of the symbols. The generalization to two dimensions results in a 16 QAM constellation. The vector $\mathbf{X}$ is determined by sampling the analog input to the receiver and has length n such that

the entire nonzero portion of the original symbol $s(t)$ is included. If this nonzero portion of the symbol covers time T (the symbol length) and the receiver's bandpass front-end input is limited to bandwidth B, n is on the order of $n = 2BT$. Note that B refers to the entire front-end detection bandwidth of the receiver, which can be much larger than the bandwidth occupied by $s(t)$. When the signal is downconverted, the inphase and quadrature components are limited in frequency to $\pm\frac{B}{2}$ and each has BT degrees of freedom, a well-known result from the Nyquist theorem.

In most signal detection analyses, $\mathbf{N}$ is assumed to be an uncorrelated Gaussian random vector (GRV) with each element distributed $N_i \sim \eta(0, \sigma^2)$ for all i (where η refers to the normal distribution). This assumption has lead to a number of elegant results in information theory pertaining to optimal receivers and channel capacity, but it is not applicable for atmospheric noise.

5.2.1 Maximum-Likelihood Detection

Using BPSK for simplicity and given that hypotheses h_1 and h_0 are equally probable, the decision rule that minimizes the probability of error for a received vector X is to compare the *a posteriori* probabilities $P(\mathbf{X}|h_1)$ and $P(\mathbf{X}|h_0)$ and choose the hypothesis corresponding to the larger one, which means choose h_1 if

$$\frac{f_{\mathbf{N}}(\mathbf{X} - \mathbf{S})}{f_{\mathbf{N}}(\mathbf{X} + \mathbf{S})} \geq 1$$

and h_0 otherwise.

For $\mathbf{N}$ an i.i.d. GRV this results in choosing h_1 if

$$\prod_{i=1}^{n} \frac{\frac{1}{2\pi\sigma^2} e^{-\frac{(|x_i - s_i|)^2}{2\sigma^2}}}{\frac{1}{2\pi\sigma^2} e^{-\frac{(|x_i + s_i|)^2}{2\sigma^2}}} \geq 1,$$

which can easily be shown by taking logarithms and rearranging terms to be equivalent to a linear matched filter detector, i.e. choose h_1 iff (if and only if) $\mathbf{X'S} > 0$. The matched filter's impulse response is the time inverted signal, demonstrating the important and well-known result that the optimal receiver for white Gaussian noise

(WGN) filters out all the input noise except for the noise at frequencies occupied by the signal. If the bandpass signal occupies a bandwidth $B_s << B$, then the equivalent baseband signal essentially has only $B_s T$ free dimensions, and only the noise samples in these dimensions affect the decision. Two important results that follow for WGN are that (1) the front-end bandwidth of the receiver need only be large enough to pass the signal, and (2) noise and/or other man-made signals outside the frequency band occupied by the signal of interest do not degrade decision performance because they are rejected by the matched filter.

For impulsive noise, however, the noise samples are not Gaussian and noise outside the signal bandwidth must be considered in the detection process if possible. A large predetection bandwidth relative to the signal bandwidth typically enhances the performance of VLF/LF receivers since the impulses remain sharp relative to the symbol length and can be more cleanly excised or compensated for. Otherwise the impulses are spread out over a large portion of the symbol waveform. On the other hand, the predetection bandwidth must be small enough to avoid adjacent man-made signals, and the signal bandwidth must be large enough to provide a useful information rate.

Once the signal characteristics and noise bandwidth are specified, the terms $f_N(\mathbf{X} - \mathbf{S})$ and $f_N(\mathbf{X} + \mathbf{S})$ must be determined in order to implement the maximum-likelihood (M-L) receiver. These are difficult to solve for impulsive noise distributions, however, and several approximations must be made. Receiver structures based on these approximations are evaluated in Section 5.4, but first a review of conventional impulsive noise receivers is presented.

5.2.2 Conventional Nonlinear Receivers

Conventional digital receivers for VLF noise have an *ad hoc* zero memory nonlinearity followed by a matched filter. The nonlinearity is generally either a clipper, blanker or hard limiter, although simulations show that the clipping amplifier is superior to the other two. The chosen nonlinearity operates on the signal plus noise in an attempt to suppress large, short duration impulses, thereby making an attempt

to "Gaussianize" the noise. Of course, the noise must be of significantly greater bandwidth than the signal for the process to be useful. Since a matched filter follows, the goal is to eliminate as much of the impulse as possible from the band occupied by the signal while minimizing signal distortion, but this is largely a trial and error process since both the receiver's front-end bandwidth and the nonlinear device's threshold level must be chosen as part of the design. Since the noise is nonstationary, one or both of these parameters may have to be adjusted adaptively.

The chosen nonlinearity may operate on a wideband receiver input, but simulations indicate that such receivers do not perform well. Although many sferics stand above all the man-made signals plus background noise, the effect of the nonlinearity on unwanted man-made interference is harmful to detection (after the nonlinearity) in the band of the signal. For this reason, the predetection bandwidth is chosen small enough to eliminate all adjacent man-made interference, and the nonlinearity is applied at baseband after downconversion.

Clippers A clipper operates linearly unless the noise exceeds the range of $+/-$ a given threshold, in which case the output is limited to the $+/-$ threshold level regardless of the input. Not counting signal distortion, using a clipper results in a noise pdf that is truncated to the threshold value, with all the original probability outside of the threshold range now placed at the threshold values. The matched filter unit that follows thus sees noise that is somewhat similar to a Gaussian distribution with its tails cut off.

Blankers Blankers (or hole punchers) simply set values outside some threshold range to zero, and so only those samples uncorrupted by large sferics enter the matched filter. Blankers perform poorly when compared to clippers because they discard data that carry significant information, even if those data are corrupted by impulses.

Hard Limiters Limiters output one value for inputs greater than zero and the negative of that value for inputs less than zero. They are simple but do not perform

as well as clippers.

Simulations Of the three conventional nonlinear receivers just described, the clipping receiver (a clipper followed by a matched filter) consistently performs the best. For the clipping receiver used in the simulations, a number of clipping threshold levels are used but only the one giving the best performance is shown for a given plot.

5.2.3 Previous Receiver Studies

This section briefly reviews previous work in developing various M-L and *ad hoc* receivers, all of which perform much better with impulsive noise than the linear matched filter receiver used for Gaussian noise.

Many receivers have been developed using a small-signal approach, which expands f_{X-S} in a Taylor series and keeps only the zero and first order terms [30, 39, 41]. Using this approximation, the M-L receiver is comprised of a zero-memory nonlinearity followed by a linear detector, and so it is similar to the conventional receivers described above. However, the nonlinearity is an arbitrarily complex function that generally cannot be implemented in analog hardware. A small signal approach is often inaccurate because many low-frequency communication systems have quite large signals at their receivers (see Figure 4.2).

Some studies choose distributions with heavier tails than those of the Gaussian distribution (*e.g.*, Cauchy, Weibull or beta), determine the optimal receiver given the distribution, and derive receiver results either empirically or with computer generated noise [10, 31, 35]. Unfortunately, the distributions used are often inaccurate for atmospheric noise.

The one M-L receiver with possible applications to this work is the log-correlator receiver, the optimal receiver for noise with a Hall distribution [23]. For independent noise samples, the optimal receiver structure is an envelope detector followed by a logarithm operation followed by a summation. Since the Hall envelope pdf is found to very accurately represent impulsive noise under certain conditions, it is expected

that some form of this log-correlator receiver may be optimal in a practical VLF design. For this reason, the log-correlator is included in the simulation analyses.

Studies of actual systems using a clipper/matched filter combination were carried out in the 1970's, when VLF systems were first being installed. Optimal clipping levels and front-end bandwidths are chosen experimentally and are system and location dependent; example results are contained in [8, 11].

5.3 Alpha-Stable Maximum Likelihood Receivers

In order to develop an optimal M-L receiver for α-stable noise, knowledge of the joint distribution of the elements of an α-stable random vector is required. Assuming the elements are distributed symmetrically about zero, this joint pdf $f_{\mathbf{N}}(\mathbf{n})$ is defined by the joint characteristic function

$$\Phi_{\mathbf{N}}(\mathbf{t}) = e^{\int_S |\mathbf{t}'\mathbf{s}|^\alpha \mu(d\mathbf{s})}, \qquad (5.1)$$

where the surface S is the unit sphere and the spectral measure $\mu(d\mathbf{S})$ is a uniquely determined finite symmetric measure on the Borel subsets of S [2]. (The variable $\mathbf{t}$ is equivalent to $\underline{\omega}$ in Section 3.2.3. Thus while a mean zero Gaussian random vector ($\alpha = 2$) of length N is uniquely determined by an $N \times N$ covariance matrix, an α-stable random vector ($\alpha \neq 2$) for even $N = 2$ requires infinite degrees of freedom to be specified. Thus it is impractical to determine the complete description of an α-stable random process from the noise.

Even though several simplified types of α-stable processes exist (*e.g.*, the sub-Gaussian, linear, and harmonizable forms [2]), none are applicable to the noise at hand. In order to proceed, a simplification is made by assuming that the elements of the vector are independent (but not identically distributed), an assumption justified by the statement in Section 2.6 that no appreciable correlations are found in adjacent samples of the background noise. Allowing the distribution (*i.e.*, the parameters α and γ) to vary with time takes into account the rapid statistical variations in the noise caused by bursts of impulses.

Covariation   As an additional measure of the lack of dependence from one noise sample to the next in VLF/LF noise, the concept of covariation is introduced and analyzed. Second order statistics such as covariance functions are not applicable for α-stable noise since the variance of α-stable noise is infinite, so the covariation coefficient is used instead. It is specified for $\alpha > 1$ as λ_{XY}, where

$$\lambda_{XY} = \frac{E(XY^{<p-1>})}{E(|Y|^p)} \tag{5.2}$$

and $1 \le p < \alpha$ [40]. An estimator for λ_{XY} using $p = 1$ is then

$$\lambda_{XY} \approx \frac{\sum_{i=1}^{N} X_i \mathrm{sign}(Y_i)}{\sum_{i=1}^{N} |Y_i|}. \tag{5.3}$$

No appreciable covariations are found for time differences greater than 1/B (where B is the bandwidth) when applying (5.3) to the data, again adding validity to the assumption that adjacent samples can be considered independent.

5.3.1   Parameter Estimations of Alpha-Stable Distributions

Since the noise samples are assumed to be independent but not identically distributed, it remains to specify the two parameters α and γ of the α-stable distribution as a function of time, based on observation of the noise. Thus it is necessary to examine parameter estimation techniques for α-stable distributions.

A number of parameter estimation techniques exist for α-stable distributions [37]; the two that are used in this dissertation are (i) histogram fitting and (ii) estimation of the characteristic function. The former is explained and used in Chapter 3; the latter is used here and is explained as follows: the characteristic function of an α-stable distribution is

$$\Phi_X(\omega) = E[e^{j\omega X}] = e^{-\gamma|\omega|^\alpha}, \tag{5.4}$$

and thus may be estimated from the data (assuming a symmetric distribution about

zero) as

$$\Phi_X(\omega) = \frac{1}{N} \sum_{i=1}^{N} \cos(\omega X_i). \tag{5.5}$$

This is performed in the analyses for $\omega \in \{0.5, 1.0, 1.5, 2.0\}$ and then a linear regression is computed using

$$\log(-\log \Phi_X(\omega)) = \log(\gamma) + \alpha \log(\omega) \tag{5.6}$$

to determine α and γ. This procedure is found to give very accurate estimates of α and γ when compared to the histogram fitting approach (which is assumed to be the most accurate) using as little as 50 data samples, and thus is used throughout the rest of this work.

Since it is desired to estimate α and γ adaptively from the received signal plus noise with as little computation as possible, two other parameter estimation schemes are considered as well. The two methods examined are (iii) to derive an estimation based on the number, size and relative times of localized impulses, and (iv) to derive an estimation based on a filtering process of the noise. Many possible implementations of method (iii) were examined but none accurately predicted the localized values of α and γ determined by the characteristic function estimation method. With method (iv), however, a simple averaging of the l_1 norm is found to correlate very strongly with localized values of α and γ. The correlation coefficient of the l_1 norm with α is roughly 0.7 and with γ it is 0.9.

5.3.2 Realizations of Alpha-Stable Receivers

Four realizations of α-stable M-L receivers are developed and simulated, based on the parameters estimation techniques of the previous section. There are endless receiver specifications possible, but the four used here are typical examples and are chosen to demonstrate in some sense the best and worst cases. Of primary interest is the BER improvement realized by α-stable receivers.

Receiver 1 has *a priori* knowledge of the best estimates of α and γ for each one minute sample of data. Changes on the order of milliseconds due to noise bursts

are not accounted for, so this receiver is typically the poorest performer among the four α-stable receivers.

Receiver 2 has *a priori* knowledge of the best estimates of α and γ on a symbol-by-symbol basis, with a minimum update period of 0.01 seconds and a maximum of 0.2 seconds. Short-term estimates of the noise parameters tend to improve performance by accounting more accurately for bursts in the noise, especially for faster symbol rates.

Receiver 3 estimates the parameters α and γ on a simulation-sample by simulation-sample basis (the simulation sample rate is 2500/sec) by maintaining a 100 sample running average of the l_1 norm of the noise (without signal). This running average is used as the input to two separate linear functions to determine α and γ; the gain and offset of the linear equations are determined *a priori*.

Receiver 4 is identical to receiver 3 except that the running average of the noise envelope magnitude is calculated from the signal plus noise. The noise envelope is estimated by subtracting off the worst-case (most distant) signal point, thus giving an indication of worst-case performance for this type of parameter estimation scheme.

The four receivers described above are somewhat arbitrary, but they are demonstrative of the performance that can be expected from practical α-stable receiver implementations. Receiver 2 typically performs the best of the four, since it has access to quick and accurate estimates of the noise. Receivers 1 and 4 typically perform the worst, 1 being slow to adjust and 4 being inaccurate in its parameter estimation.

5.4 Simulation Results

This section presents the results of hundreds of BER simulations performed using actual VLF/LF noise samples as additive input noise. Signal center frequencies range from 18 kHz to 45 kHz and span a number of times, locations and input bandwidths, and rectangular pulses are used as the symbol basis function. The simulations concentrate on those times and locations for which the noise is most

accurately modeled as α-stable, but other cases are considered as well. The goals of the simulations are as follows: (i) to compare clipping receivers to limiters and linear (matched filter) receivers, (ii) to show the effect of predetection bandwidth and/or symbol rate on BER, (iii) to compare the performance of α-stable receivers to that of clipping receivers, (iv) to determine performance differences between the four types of α-stable receivers listed in Section 5.3.2, and (v) to compute the performance loss when using 16 QAM rather than QPSK with α-stable noise. Note that (i) and (ii) confirm previously known results.

The BER curves are plotted as a function of E_b/N_0, where E_b is the energy per bit and N_0 is twice the variance of the measured noise samples (so that $N_0/2$ is the variance). The use of N_0 maintains consistency with previous literature, but is problematic due to the infinite second moment of α-stable noise. It must be noted then that BER comparisons cannot be made when using different noise samples; however, BER comparisons using the same noise sample (time, station, bandwidth and center frequency) are valid. Both two and four level constellations are examined (QPSK and 16 QAM); larger constellations are not considered due to the increased complexity required in the simulation algorithms.

Figure 5.1 shows typical simulation results for QPSK signals in impulsive noise. The noise has a bandwidth of 2 kHz, centered about 26.5 kHz, and is from Arrival Heights during June of 1996. The symbol rate is 50/sec. The matched filter (the upper solid line) is clearly the worst performer, followed by the limiter, clipper, log correlator and type 2 α-stable receivers. The latter three are very close, however, and for most of the simulation plots they are essentially identical. This result confirms that a simple clipping amplifier followed by a matched filter is nearly optimal for QPSK, as first predicted in 1974 by Evans and Griffiths [11].

Figure 5.2 shows the simulation results for 16 QAM using the exact same noise samples as in Figure 5.1. In this case the two M-L based receivers, the α-stable and log-correlator receivers, are clearly optimal to the conventional nonlinear receivers. Most plots show the α-stable receiver a few tenths of a dB ahead of the log-correlator, and the latter at least 3 dB better than the rest at low BER ($< 10^{-4}$).

Figure 5.3 shows the performance of the four α-stable receiver types described
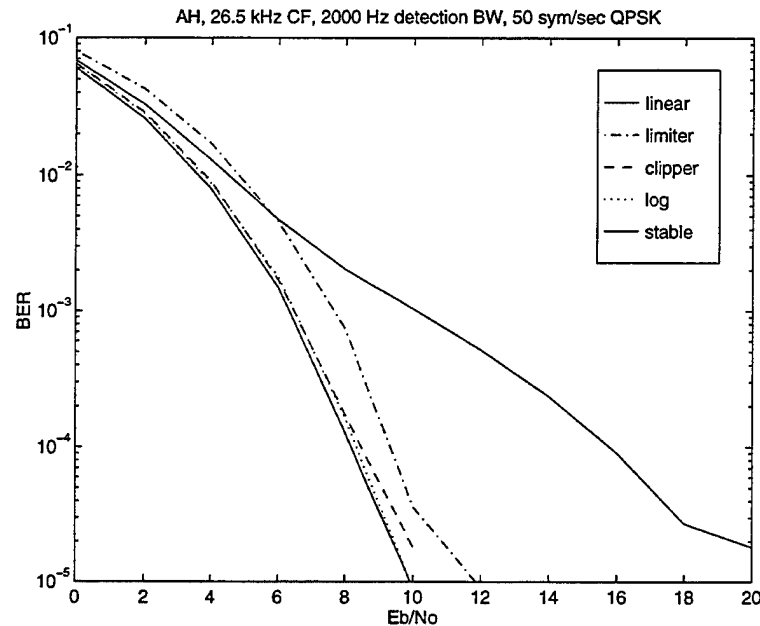
Figure 5.1: Typical BER curve for QPSK noise, comparing linear, limiter, clipper, log correlator and α-stable receivers. The data are from June 1996 at Arrival Heights. The "linear" solid line is to the right of the "stable" solid line.

in Section 5.3 for a 16 QAM constellation. As mentioned above, receiver 2 typically performs the best, although the others are often within 1.0 dB at BER's of 10^{-4}. (The 2 dB difference seen in Figure 5.3 is somewhat of a worst case).

It is mentioned earlier that decreasing the symbol rate or increasing the predetection bandwidth can greatly improve performance, especially for noise characterized by large but infrequent impulses. These effects are shown in Figure 5.4, where the plots show BER curves for symbol times from 1–100 symbols per second and the three subfigures themselves show variation with predetection bandwidth. (Note that the one second per symbol curve on Figure 5.4(a) is off the left side of the plot). Comparison of the three plots demonstrates the large variation in measured N_0 that results when large impulses are smoothed by narrower and narrower predetection filters.

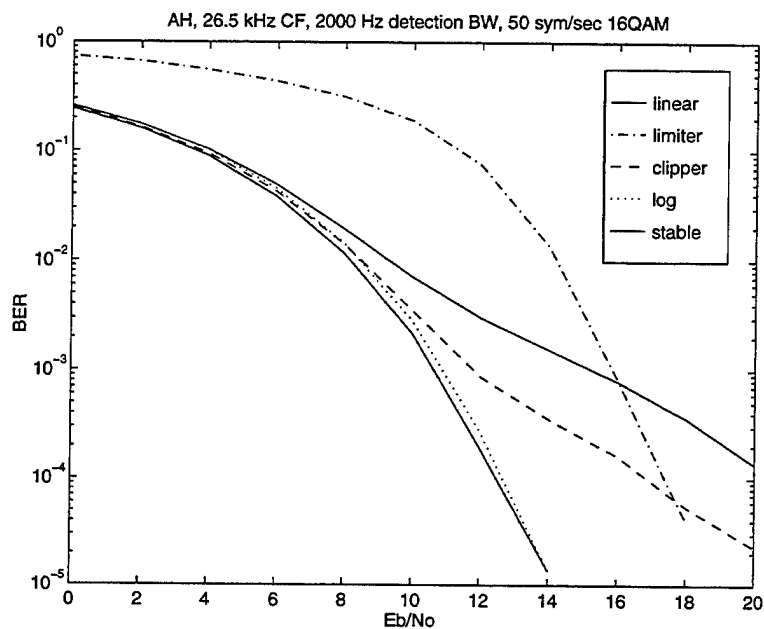The final topic regarding the receiver simulations concerns QPSK versus 16

Figure 5.2: Typical BER curve for 16 QAM noise, comparing linear, limiter, clipper, log correlator and α-stable receivers. The data are from June 1996 at Arrival Heights. The "linear" solid line is to the right of the "stable" solid line.
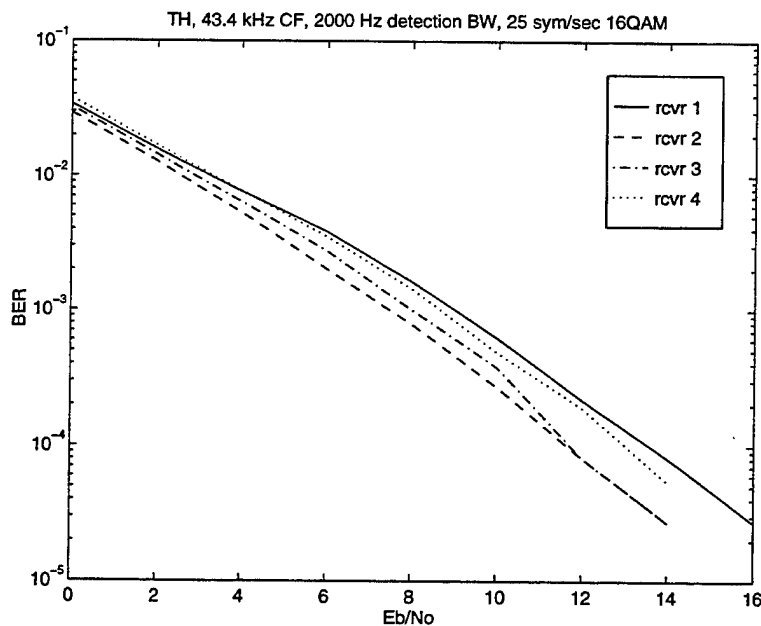

Figure 5.3: BER comparison of four realizations of the α-stable receiver

QAM. The latter requires five times more energy than the former in order to maintain the same minimum distance in the signal constellation, which translates to a 5/2 (4 dB) handicap in energy/bit (as clearly seen when comparing the α-stable receivers in Figures 5.1 and 5.2 at a BER of 10^{-5}). With impulsive noise, however, performance increases with symbol time for the same E_b/N_0, so it is possible that this gap could be compensated for in some cases. The question of interest then is whether it more advantageous to transmit 16 QAM with symbol time 2T or QPSK with symbol time T, using the same average transmitted power.

Simulation results show that 16 QAM with symbol time 2T does in fact give better performance than QPSK with symbol time T for high V_d noise and time-bandwidth products on the order of ten. This is due to the nature of impulsive noise, which when compared to Gaussian noise with the same N_0 will have a much lower level of background noise. Since the idea of signal reception in sporadically impulsive noise is to evaluate the signal "between the impulses", it follows that a multilevel constellation could be transmitted with longer symbols to take advantage of lower level background noise, with no loss of data rate.

Figure 5.5 shows BER's for three cases of QPSK versus 16 QAM. For low and high data rates, the 4 dB performance loss is clearly seen, but at 125 symbols/second 16 QAM, the curves cross. At high data rates (only a few independent noise samples per symbol), a large impulse dominates the symbol regardless of the signal constellation. For low data rates, the greatest percentage of data samples per symbol are background noise and the BER curves roll off in a shape similar to those for Gaussian noise. For BT on the order of ten, however, the low-level background noise in a double length symbol can make up for a short impulse somewhere in the symbol, making 16 QAM a better option than QPSK for the same transmitted power.

5.5   Conclusions

This chapter shows the results of BER receiver simulations performed in order to compare α-stable receivers to common analog receivers. The conclusions drawn from

(a) 2000 Hz bandwidth

(b) 600 Hz bandwidth

(c) 300 Hz bandwidth
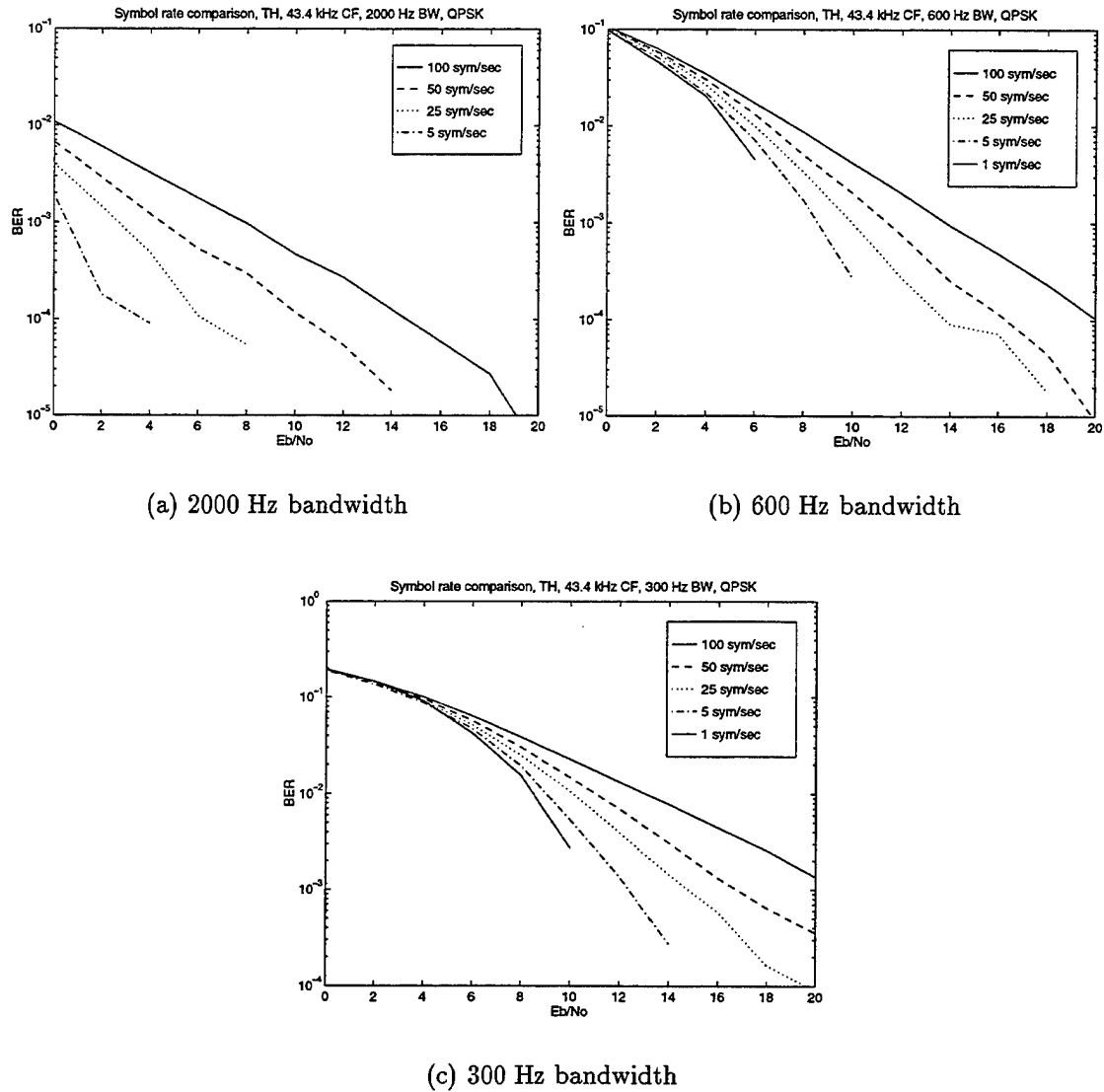
Figure 5.4: BER curves for five different symbol times using an α-stable receiver. The noise data are from June 1986 at Thule, Greenland, with a 43.4 kHz center frequency.
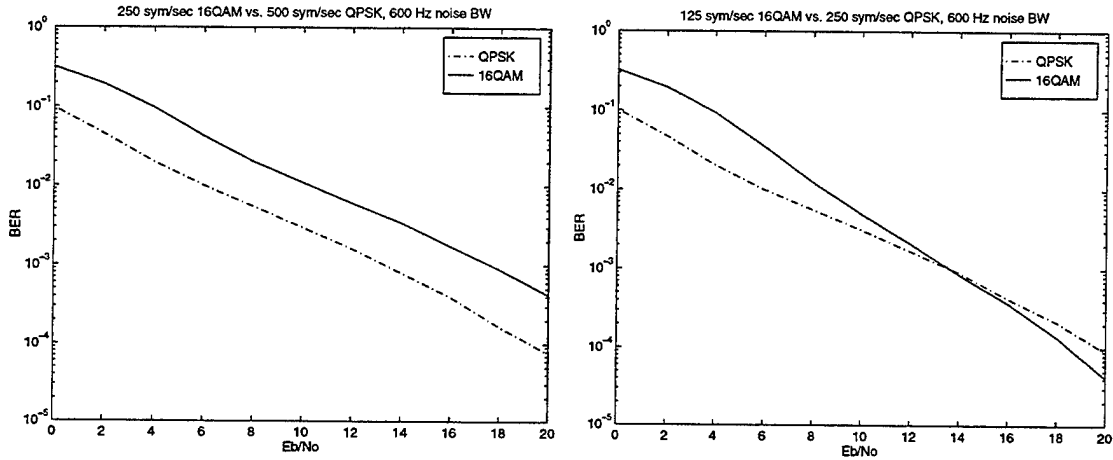
(a) 250 sym/s 16 QAM vs. 500 sym/s QPSK

(b) 125 sym/s 16 QAM vs. 250 sym/s QPSK
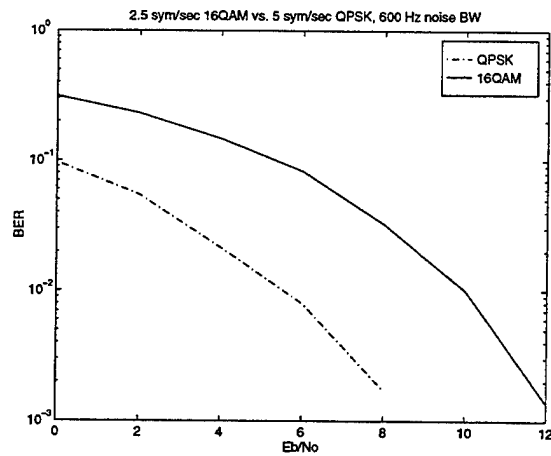
(c) 2.5 sym/s 16 QAM vs. 5 sym/s QPSK

Figure 5.5: QPSK vs. 16 QAM, with 16 QAM at half the symbol rate of QPSK. The noise data are from Thule, Greenland, with a 43.4 kHz center frequency and a 600 Hz bandwidth.

these simulations are as follows: (i) For VLF/LF digital communication systems using a QPSK signal format, an α-stable receiver provides essentially no performance improvement over a conventional clipping receiver. (This result can likely be generalized for all other constant amplitude constellations as well). (ii) For a 16 QAM signal format, a receiver optimized for α-stable noise provides several dB of performance improvement at low BER. (iii) High SNR communication systems operating in high V_d impulsive noise realize 1-2 dB better BER performance for the same bit rate and average transmitted power when using 16 QAM instead of QPSK.

Chapter 6

Conclusions

This chapter summarizes the main results of the dissertation and discusses possible areas of future research.

6.1　Summary of Results

Chapter 2 introduces some of the statistical properties of low-frequency radio noise. It is found and/or verified that (i) seasonal and diurnal variations correlate well with global lightning patterns and can be used to track global climate change, (ii) the narrowband noise envelope pdf of low-frequency noise has the functional form of a Rayleigh pdf at low values of dynamic range but decays with an inverse power law at high values, (iii) interarrival time distributions indicate clustering of sferics with bursts on the order of one second in length, (iv) no appreciable correlations are found between the maximum amplitudes of adjacent sferics or between these maximum amplitudes and interarrival times, and (v) low-frequency noise can be viewed as the superposition of white Gaussian noise and discrete noise impulses from sferics.

Chapter 3 describes three models used for low-frequency noise envelope pdf's and determines the parameters and accuracy of each model as a function of location, time and frequency. The parameters and errors of each model are found to vary with thunderstorm activity and the noise frequency and bandwidth. The chapter concludes that the Hall model is the optimal choice in terms of accuracy and

simplicity for locations exposed to heavy sferic activity, and the α-stable model is best for those relatively distant from heavy sferic activity.

Chapter 4 proposes a statistical-physical clustering Poisson model for atmospheric noise. According to the model, the sources of the noise are clusters of impulses with independent and identically distributed waveforms. Cluster occurrence is a spatial and temporal Poisson process with source distribution independent of direction and time. The impulses within clusters are defined as variable length Poisson processes. It is verified that the clustering Poisson model accurately predicts the statistical features of the actual data, and thus proves to be a good candidate as a model for atmospheric noise.

Chapter 5 shows the results of BER receiver simulations performed in order to compare α-stable receivers to common analog receivers. The conclusions drawn from these simulations are as follows: (i) For VLF/LF digital communication systems using a QPSK signal format, an α-stable receiver provides essentially no performance improvement over a conventional clipping receiver. (ii) For a 16 QAM signal format, a receiver optimized for α-stable noise provides several dB of performance improvement at low BER. (iii) High SNR communication systems operating in high V_d impulsive noise realize 1-2 dB better BER performance for the same bit rate and average transmitted power when using 16 QAM instead of QPSK.

6.2 Topics for Future Research

Possible topics for future research are as follows:

- Building a hardware prototype of an α-stable receiver and using it in an actual communication system would provide useful results on the improvement realized by such a receiver. The receiver would likely require digital signal processing (DSP) type integrated circuit hardware.

- Obtaining more detailed results on the specification of the α-stable joint pdf of impulsive noise may provide opportunity to improve α-stable receiver structures and algorithms.

- Acquiring and analyzing a continuous, worldwide collection of three axis ELF/VLF/LF time-series data with extremely accurate system timing would allow direction finding and ranging to be included in the analysis and modeling. Such a database will be collected eventually, and will allow more accurate models of low-frequency atmospheric noise to be developed, especially regarding the specification of cluster waveforms in the clustering Poisson model.

Bibliography

[1] T.F. Bell and R.A. Helliwell. Pulsation phenomena observed in long-duration VLF whistler-mode signals. *Journal of Geophysical Research*, 76(34):8414 – 8419, 1971.

[2] S. Cambanis and G. Miller. Linear problems in pth order and stable processes. *SIAM Journal on Applied Mathematics*, 41(1):43–69, August 1981.

[3] D. Chrissan and A.C. Fraser-Smith. Seasonal variations of globally measured ELF/VLF radio noise. Report D177-1, Space, Telecommunications and Radioscience Laboratory, Stanford University, Stanford, California, December 1996.

[4] D. Chrissan and A.C. Fraser-Smith. Seasonal variations of globally measured ELF/VLF radio noise. *Radio Science*, 31(5):1141–1152, 1996.

[5] D. Chrissan and A.C. Fraser-Smith. Diurnal variations of globally measured ELF/VLF radio noise. Report D177-2, Space, Telecommunications and Radioscience Laboratory, Stanford University, Stanford, California, June 1997.

[6] Thomas M. Cover and Joy A. Thomas. *Elements of Information Theory*. Wiley, New York, 1991.

[7] W. Q. Crichlow, C. J. Roubique, A. D. Spaulding, and W. M. Beery. Determination of the amplitude-probability distribution of atmospheric radio noise from statistical moments. *Journal of Research of the National Bureau of Standards-D. Radio Propagation*, 64D(1):49–56, Jan.–Feb. 1960.

[8] John R. Davis and William D. Meyers. ELF atmospheric noise excision by wideband clipping. *Radio Science*, 11(12):991–999, 1976.

[9] Herbert Bristol Dwight. *Tables of Integrals and Other Mathematical Data.* Macmillan, Toronto, fourth edition, 1969.

[10] Per K. Enge and Dilip V. Sarwate. Spread-spectrum multiple-access performance of orthogonal codes: Impulsive noise. *IEEE Transactions on Communications*, 36(1):98–106, January 1988.

[11] J. E. Evans and A. S. Griffiths. Design of a sanguine noise processor based upon worldwide extremely low frequency (ELF) recordings. *IEEE Transactions on Communications*, 22(1):528–539, 1974.

[12] Edward C. Field, Jr. and Marcus Lewinstein. Amplitude-probability distribution model for VLF/ELF atmospheric noise. *IEEE Transactions on Communications*, 26(1):83–87, 1978.

[13] A.C. Fraser-Smith and R.A. Helliwell. The stanford university ELF/VLF radiometer project: measurement of the global distribution of ELF/VLF electromagnetic noise. In *Proceedings of the 1985 International Symposium on Electromagnetic Compatibility*, pages 305–311, Wakefield, Mass., August 1985.

[14] A.C. Fraser-Smith, R.A. Helliwell, B.R. Fortnam, P.R. McGill, and C.C. Teague. A new global survey of ELF/VLF radio noise, conf. on effects of electromagnetic noise and interference on performance of military radio communication systems, Lisbon, Portugal, 26-30 october, 1987. In *AGARD Conference Proceedings*, number 420, pages 4A-1–4A-9, 1988.

[15] Martin Füllekrug and A.C. Fraser-Smith. Global lightning and climate variability inferred from ELF magnetic field variations. *Geophysical Research Letters*, 24(19):2411–2414, 1997.

[16] K Furutsu and T. Ishida. On the theory of amplitude distribution of impulsive radio noise. *Journal of Applied Physics*, 32(7):1206–1221, 1961.

[17] A.A. Giordano, J.R. Herman, X.A. DeAngelis, K.F. Marzotto, and F.M. Hsu. Measurement and statistical analysis of wideband MF atmospheric noise: 2. Impact of data on bandwidth and system performance. *Radio Science*, 21(2):203–222, 1986.

[18] Arthur A. Giordano and Fred Haber. Modeling of atmospheric noise. *Radio Science*, 7(11):1011–1023, 1972.

[19] S.J. Goodman and H.J. Christian. Global observations of lightning. In R.J. Gurney, editor, *Atlas of Satellite Observations Related to Global Change*, pages 191–219, New York, N.Y., 1993. Cambridge University Press.

[20] I. S. Gradshteyn and I. M. Ryzhik. *Table of Integrals, Series and Products*. Academic, New York, 1965.

[21] F. Grüneis, M. Nakao, M. Yamamoto, T. Musha, and H. Nakahama. An interpretation of 1/f fluctuations in neuronal spike trains during dream sleep. *Biological Cybernetics*, 60:161–169, 1989.

[22] Ferdinand Grüneis and Hans J. Baiter. More detailed explanation of a number fluctuation model generating 1/f pattern. *Physica A*, 136:432–452, 1986.

[23] H. M. Hall. *A new model for "impulsive" noise phenomena: Applications to atmospheric noise channels*. PhD thesis, Stanford University, 1966.

[24] Robert A. Helliwell. *Whistlers and Related Ionospheric Phenomena*. Stanford University Press, Stanford, California, 1965.

[25] International Radio Consultative Committee. CCIR world distribution and characteristics of atmospheric radio noise. Report CCIR-322, International Telecommunications Union, Geneva, Switzerland, 1964.

[26] International Radio Consultative Committee. Characteristics and applications of atmospheric radio noise data. Report CCIR-322-3, International Telecommunications Union, Geneva, Switzerland, 1988.

[27] R.A. Kirby. Evaluation of omega navigation system. *Geophysics*, 35(2):344–356, 1970.

[28] L.J. Lanzerotti, C.G. Maclennan, and A.C. Fraser-Smith. Background magnetic spectra: 10^{-5} to 10^5 Hz. *Geophysical Research Letters*, 17(10):1593–1596, September 1990.

[29] P.A.W. Lewis. A branching poisson process model for the analysis of computer failure patterns. *Journal of the Royal Statistical Society*, 29(B):343–354, 1964.

[30] Ning Hsing Lu and Bruce A. Eisenstein. Detection of weak signals in non-Gaussian noise. *IEEE Transactions on Information Theory*, 27(6):755–771, November 1981.

[31] Andrew B. Martinez and John B. Thomas. Detector design using a density fit to non-Gaussian noise. *IEEE Transactions on Information Theory*, 34(3):544–550, May–June 1988.

[32] David Middleton. *Introduction to Statistical Communication Theory*. McGraw-Hill, New York, 1960.

[33] David Middleton. Statistical-physical models of electromagnetic interference. *IEEE Transactions on Electromagnetic Compatibility*, 19(3):106–127, August 1977.

[34] J. H. Miller and J. B. Thomas. Robust detectors for signals in non-Gaussian noise. *IEEE Transactions on Communications*, COM-25(7):686–690, July 1977.

[35] James H. Miller and John B. Thomas. Detectors for discrete-time signals in non-Gaussian noise. *IEEE Transactions on Information Theory*, 18(2):241–249, March 1972.

[36] Taketoshi Nakai. Modeling of atmospheric radio noise near thunderstorms. *Radio Science*, 18(2):187–198, 1983.

[37] Chrysostomos L. Nikias and Min Shao. *Signal Processing with Alpha Stable Distributions and Applications*. Wiley, New York, 1995.

[38] John G. Proakis and Masoud Salehi. *Communication Systems Engineering*. Prentice Hall, Englewood Cliffs, N.J., 1994.

[39] S.S. Rappaport and L. Kurz. An optimal nonlinear detector for digital data transmission through non-Gaussian channels. *IEEE Transactions on Communications*, 14(3):266–274, June 1966.

[40] G. Samorodnitsky and M. S. Taqqu. *Stable Non-Gaussian Random Processes: Stochastic Models with Infinite Variance*. Chapman and Hall, New York, N.Y., 1994.

[41] A.D. Spaulding. Locally optimum and suboptimum detector performance in a non-Gaussian interference environment. *IEEE Transactions on Communications*, 33(6):509–517, June 1985.

[42] A.D. Spaulding, C.J. Roubique, and W.Q. Crichlow. Conversion of the amplitude-probability distribution function for atmospheric radio noise from one bandwidth to another. *Journal of Research of the National Bureau of Standards-D. Radio Propagation*, 66D(6):713–720, November–December 1962.

[43] Herbert Taub and Donald L. Schilling. *Principles of Communications Systems*. McGraw-Hill, New York, second edition, 1986.

[44] Martin A. Uman. *Lightning*. McGraw-Hill, New York, 1969.

[45] D. Vere-Jones. Stochastic models for earthquake occurrence. *Journal of the Royal Statistical Society*, 32(B):1–45, 1970.

[46] C.R. Warber and E.C. Field, Jr. A long wave transverse electric-transverse magnetic noise prediction model. *Radio Science*, 30(3):783–797, 1995.

[47] A.D. Watt and E.L. Maxwell. Measured statistical characteristics of VLF atmospheric radio noise. *Proceedings of the IRE*, 45:55–62, 1957.

[48] V. M. Zolotarev. *One-dimensional Stable Distributions*. American Mathematical Society, Providence, R.I., 1986.

REPORT DOCUMENTATION PAGE

Public reporting burden for this collection of information is estimated to average 1 hour per response, including the time for reviewing instructions, searching existing data sources, gathering and maintaining the data needed, and completing and reviewing the collection of information. Send comments regarding this burden estimate or any other aspect of this collection of information, including suggestions for reducing this burden to Washington Headquarters Services, Directorate for Information Operations and Reports, 1215 Jefferson Davis Highway, Suite 1204, Arlington, VA 22202-4302, and to the Office of Management and Budget, Paperwork Reduction Project (0704-0188), Washington, DC 20503.

1. AGENCY USE ONLY *(Leave blank)*	2. REPORT DATE August 1998	3. REPORT TYPE AND DATES COVERED 09/01/93– Final Technical Report 06/30/97

4. TITLE AND SUBTITLE

Statistical Analysis and Modeling of Low-Frequency Radio Noise and Improvement of Low-Frequency Communication

5. FUNDING NUMBERS

N00014-93-1-1073 (G)

6. AUTHOR(S)

Douglas A. Chrissan

7. PERFORMING ORGANIZATION NAMES(S) AND ADDRESS(ES)

STAR Laboratory
Stanford University
Stanford, CA 94305

8. PERFORMING ORGANIZATION REPORT NUMBER

D179-1

9. SPONSORING / MONITORING AGENCY NAMES(S) AND ADDRESS(ES)

Office of Naval Research   Code 321SR
800 N. Quincy Street
Arlington, VA 22217

10. SPONSORING / MONITORING AGENCY REPORT NUMBER

11. SUPPLEMENTARY NOTES

This report was prepared as a Ph.D. dissertation

a. DISTRIBUTION / AVAILABILITY STATEMENT

Approved for public release; distribution unlimited

12. DISTRIBUTION CODE

13. ABSTRACT *(Maximum 200 words)*

The objective of this work is the statistical characterization and modeling of atmospheric radio noise in the range 10 Hz – 60 kHz (denoted *low-frequency* noise), with the specific goal of improving communication systems operating in this range. The analyses are based on many thousands of hours of measurements made by the Stanford Radio Noise Survey System. The statistics analyzed include seasonal and diurnal variations, amplitude probability distributions (APDs), impulse interarrival time distributions, background noise statistics, and power spectral densities. Noise characteristics derived from these analyses are presented, and several noise models that accurately represent low-frequency noise APDs are compared. Two of the simplest models (*i.e.*, each with only two parameters) are found to give extremely good performance in general. These are the Hall and alpha-stable models, both of which approximate the Rayleigh distribution for low amplitude values but decay with an inverse power law for high amplitude values. Based on the statistical characterstics of the noise data, a new clustering Poisson atmospheric noise model is developed. This model is based on several previously known statistical-physical models, but in addition takes into account the clustering of sferic impulses. It is shown that the clustering model accurately predicts the statistical features found in low-frequency radio noise data.

14. SUBJECT TERMS

ELF Noise, VLF Noise SFERICS, Radio Noise Statistics, Alpha-Stable Noise Model, APD's

15. NUMBER OF PAGES
116

16. PRICE CODE
N/A

17. SECURITY CLASSIFICATION OF REPORT	18. SECURITY CLASSIFICATION OF THIS PAGE	19. SECURITY CLASSIFICATION OF ABSTRACT	20. LIMITATION OF ABSTRACT
Unclassified	Unclassified	Unclassified	UL

Standard Form 298 (Rev. 2-89)